**Title**
High Repetition Rate Mapping of the Different Regimes of Laminar Collisionless Coupling



**Author**
Dorst, Robert S

**Publication Date**
2023

Peer reviewed|Thesis/dissertation

UNIVERSITY OF CALIFORNIA
Los Angeles

# High Repetition Rate Mapping of the Different Regimes of Laminar Collisionless Coupling

A dissertation submitted in partial satisfaction
of the requirements for the degree
Doctor of Philosophy in Physics

by

Robert Spencer Dorst

2023

ABSTRACT OF THE DISSERTATION

High Repetition Rate Mapping of the Different Regimes of Laminar Collisionless Coupling

by

Robert Spencer Dorst
Doctor of Philosophy in Physics
University of California, Los Angeles, 2023
Professor Christoph Niemann, Chair

Throughout this work, the collective electromagnetic effects that mediate the transfer of energy from an energetic, dense plasma species to a relatively tenuous, magnetized plasma species are studied. These are observed to play an important role in a wide variety of space and astrophysical environments such as supernova remnants, coronal mass ejections, planetary bow-shocks, and man made ionospheric explosions. Laboratory experiments can create scaled versions of these systems using smaller denser plasmas characterized by similar dimensionless parameters. These can complement *in-situ* measurements and validate theoretical and computational models. One of the greatest advantages of laboratory experiments lies in the direct control of parameters and in the repeatability, which allows for many-point measurements of the interaction over successive data runs.

Experiments performed at UCLA combined a high-energy laser and the Large Plasma Device (LADP) to investigate collisionless coupling between an exploding laser-produced plasma (LPP) and a magnetized helium plasma. A laser induced fluorescence (LIF) diagnostic has been developed and optimized using collisional-radiative modeling to investigate the spatially and temporally evolving ion velocity distribution function of the LPP as it interacts with the magnetized plasma.

LIF measurements provide new insight into the two primary drivers that transfer energy: the magnetic structure feature which moves ions down magnetic field gradients and the Larmor feature which induces an $\mathbf{E}\times\mathbf{B}$ drift in the ambient plasma. Two experiments were conducted to investigate the different coupling regimes.

The first experiment observes the coupling when the expansion of the LPP is sub-Alfvénic ($\mathrm{M}_A = v/v_A < 1$). The LIF diagnostic maps the deceleration of LPP ions in the region where large magnetic gradients are observed. Three dimensional particle-in-cell (PIC) simulations reproduce the measured quantities well and offer new insight into the electric fields responsible for coupling. Measurements in combination with PIC simulations show that energy is transferred from the energetic species to the magnetized species consistent with the magnetic structure term. Directly measuring particle distribution functions with LIF significantly improves the initialization of the simulations.

The second experiment investigates coupling when the expansion is super-Alfvenic ($\mathrm{M}_A = v/v_A > 1$). We observe the formation and propagation of an additional magnetic structure, or "blob", in the ambient plasma that separates a relatively large distance ($\sim 0.4\delta_i$) from the bulk diamagnetic cavity ($\sim \delta_i$). This blob is observed to coincide with the focusing of the LPP ions into a jet-like structure which results from magnetic pressure gradients that act perpendicularly to both the magnetic field and bulk LPP direction of motion. Magnetized ambient ions are observed to accelerate along a trajectory consistent with Larmor coupling in the regions where LPP ions are observed to stream across magnetic field lines. The formation of the blob is consistent with an electron population confined between the Larmor electric fields created by the jet-like ion flow and the charge separation electric fields created from the accelerated helium ions.

The dissertation of Robert Spencer Dorst is approved.

Walter N. Gekelman

Troy A. Carter

George J. Morales

Christoph Niemann, Committee Chair

University of California, Los Angeles

2023

To Sophie

TABLE OF CONTENTS

LIST OF FIGURES

LIST OF TABLES

# ACKNOWLEDGMENTS

I would like to thank:

My advisor, Prof. Chris Niemann for always being and encouraging and trusting mentor, even during stressful times, for his vast and helpful insights into plasma physics and optics, and for giving me the opportunity to participate in such exciting experiments.

Dr. Carmen Constantin for building and maintaining the lasers systems that we would not be able to perform our experiments without, for staying late into the night during LAPD campaigns, and for the many espresso breaks to keep us going even in the hardest of times.

Prof. Walter Gekelman for always being present during experiments to provide valuable insight into laser-produced plasma experiments, for allowing the use of the Spectra Physics laser for my first experiment, and for being on my committee.

Prof. Troy Carter for taking me on one of the most memorable bike rides I have ever gone on, for teaching my EM class, and for being on my committee.

Prof. George Morales for teaching a series of classes I was lucky to take, and for being on my committee.

Prof. Derek Schaeffer for his LabVIEW wizardry, additional mentoring, and for trusting me to build a pulsed power supply.

My fellow graduate students, Dr. Peter Heuer and Jessica Pilgram for their help and companionship throughout graduate school.

Dr. Stephen Vincena and Dr. Shreekrishna Tripathi for their assistance and advice during the LAPD campaigns, for staying late hours and coming in on weekends, and always remaining patient with me when I am at my most stressed.

Zolton Lucky, Marvin Drandell, Tai Ly, and Dr. Patrick Pribyl for help in making the experiments run smoothly, and for being available to assist at the most crucial moments and Avdit Kohli for making countless bdot probes.

Dr. Anton Bondarenko for the initial design work of the diagnostic that I used so heavily throughout my Ph.D.

My high school physics teacher, Charlie Bissell, who initially inspired me to pursue physics.

My family and for their constant support, love, and for only occasionally asking when I would graduate.

My friends who kept me (relatively) sane throughout graduate school.

VITA

2014–2016 **Undergraduate Student Researcher**, Department of Physics, University of California, Santa Barbara, Santa Barbara

2016 **B.S., Physics**, University of California, Santa Barbara, Santa Barbara

2016–2016 **Teaching Assistant**, Department of Physics and Astronomy, University of California, Los Angeles

2017 **M.S., Physics**, University of California, Los Angeles

2016–present **Graduate Student Researcher**, Department of Physics and Astronomy, University of California, Los Angeles

PUBLICATIONS

**Measurements of ion velocity distributions in a large scale laser-produced plasma**

R.S. Dorst, P.V. Heuer, D.B. Schaeffer, C.G. Constantin, and C. Niemann, 2020, RSI, 91, 103103

**Planar laser induced fluorescence mapping of a carbon laser produced plasma**

R. S. Dorst, C. G. Constantin, D. B. Schaeffer, J. J. Pilgram, and C. Niemann, 2022, RSI, 93, 103518

**High repetition rate mapping of the interaction between a laser plasma and magnetized background plasma via laser induced fluorescence**

R. S. Dorst, D. B. Schaeffer, A. Le, J. J. Pilgram, C. G. Constantin, S. Vincena, S. P. Tripathi, D. Winske, D. Larson, M. Cowee, and C. Niemann, 2022, PoP, 29, 082113

# CHAPTER 1

# Introduction

## 1.1 Overview

Plasma is pervasive throughout the universe, making up around 99% of the observable mass. What makes a plasma unique from the other states of matter is the existence of unbound charged particles that interact with electromagnetic radiation. This results in complex motion of the particles governed by collective behavior. If a sufficiently strong magnetic field is present, it can alter the trajectory of the particles enough to confine the particle orbits within the system size and it is considered magnetized. These magnetic fields can break symmetries otherwise seen in particle dynamics, as well as mediate the transfer of energy and momentum from one plasma species to another.

This transfer of energy from one particle distribution to another has been well understood for quite a long time when particle-particle collisions dominate the interaction. Understanding the transfer of energy between particles over length scales much smaller than the collisional mean free path, as is the case in many space and astrophysical environments, has proven more difficult. Generally speaking, plasmas are quite rarefied - enough so that classic Coulomb collisions are negligible on the length scales over which the dynamics evolve. As these particles are charged, their movements affect the electric and magnetic fields in a self-consistent way.

One type of plasma interaction involved in a wide variety of space and astrophysical environments is that of an energetic, dense plasma expanding into a relatively diffuse, magnetized plasma. Examples

of such interactions are observed at the edge of supernova remnants [83], man made ionospheric explosions [32], and planetary bow shock formation [47]. These environments are known to be efficient particle accelerators, seed large-scale instabilities, and produce high energy gamma-ray bursts.

Laboratory scaled experiments have been devised to complement *in-situ* observations and help accelerate our understanding of the underlying physics. For example, collisionless shocks are phenomena that naturally occur in space and astrophysical environments where directed kinetic energy is converted to thermal energy over length scales much smaller than the collisional mean free path. The Rankine Hugoniot jump conditions [17] describe the global characteristics of the solar wind and ionospheric plasmas far from the shock structure, but the microphysics responsible for dissipation on the shock scale are not well understood. A handful of laser plasma experiments [64, 75] have successfully created a collisionless shock in the laboratory. These can provide spatially resolved measurements to validate numerical models and *in-situ* measurements [20, 46, 90, 31, 93].

Explosive plasma interactions are not limited to natural phenomena. Active Magnetospheric Particle Tracer Explorers (AMPTE) was a series of missions aimed at studying Earth's magnetosphere and its interactions with the solar wind [6]. A cloud of photo-ionized barium ions was released in the magnetosphere and observed to interact with the magnetized hydrogen plasma of the solar wind. The unanticipated motion of the barium ions transverse to both the solar wind flow and interplanetary magnetic field was observed. This provided the earliest direct evidence of collisionless transfer of energy through the laminar electric fields [53]. The energetic ion species in such experiments is often referred to as "debris" plasma, denoted by a "d" in equations.

One common way of recreating the interaction of an energetic plasma and a tenuous magnetized plasma in the laboratory is by utilizing a high-power laser to ablate the surface of a solid target. Among the first was Ripin [73] who observed the creation of a plasma from a high intensity laser ($10^{12}$ – $19^{15}$ W/cm$^2$) focused onto a foil where the laser produced plasma (LPP) expanded into a vacuum. In more modern experiments, the LPP expands into a preformed, magnetized plasma.

Here, the Large Plasma Device (LAPD) at UCLA provides the magnetized plasma [36]. The absolute scales of a laboratory experiment and astrophysical interactions are orders of magnitude different. With proper scaling, laboratory experiments help to reveal the same underlying physics. Theoretical works [31] and prior experiments [77] have identified the most critical parameters to match in order for the dynamics to most closely resemble those observed *in-situ*. A comparison between the absolute and dimensionless parameters are shown in table 1.1: for this comparison we focus on the conditions of the AMPTE mission which most closely resemble the experiments performed here.

| Absolute | Laboratory | AMPTE |
|---|---|---|
| v (km/s) | $50 - 300$ | 1400 |
| $n_i$ ambient ($cm^{-3}$) | $2 \times 10^{13}$ | $10^7$ |
| L (m) | $0.1 - 1$ | $10^5$ |
| B (G) | $300 - 2000$ | 0.3 |
| $T_e$ (eV) | $1 - 10$ | $\sim 400$ |
| t (ns) | $10 - 1000$ | $> 10^9$ |
| **Scaled** | **Laboratory** | **AMPTE** |
| $M_A = v/v_A$ | $0.5 - 2.5$ | 8 |
| $\beta_e < 1$ | $<< 1$ | 0.1 |
| $t\ \Omega_{c,a} > 1$ | $1 - 5$ | $10 - 100$ |
| $L/\rho_i > 1$ | $1 - 2$ | $\sim 1 - 5$ |
| $L/\lambda_{mfp} << 1$ | $10^{-3}$ | $10^{-6}$ |

Table 1.1: Comparison between the absolute scales and scaled parameters in the laboratory and space environments, specifically for AMPTE reported in Bernhardt et al. [6]. Through proper scaling of characteristic plasma parameters, many of the AMPTE features are explored in the laboratory. The scaled quantities that do not match well ($L/\lambda_{mfp}$ and $t\ \Omega_{c,a}$) are both above the cutoff value ($> 1$), which is the necessary condition for relating the two quantities. Unfortunately, many of the scaled properties depend on multiple parameters and so we are not able to optimize all simultaneously in the laboratory.

These characteristic scaling parameters generally depend on more than one physical parameter, and therefore it is not possible to match every one. The Alfvénic mach number ($M_A = v/v_A$) represents the ratio between the bulk velocity (v) to the Alfvén velocity ($v_A = B/\sqrt{4\pi m_a n_a}$). The time scale is expressed relative to the ion cyclotron frequency ($\Omega_i = q_i B/m_i c$), and length scales are relative to either the ion inertial length ($\delta_i = c/\omega_{p,i}$ where $\omega_{p,i} = \sqrt{4\pi n_i q_i^2/m_i}$ is the plasma frequency), or the directed ion gyroradius ($\rho_i = v/\Omega_i$). For these equations B is the magnetic field

value, $m_i$ is the ion mass ('a' for ambient and 'l' or 'd' for the laser produced debris plasma), $n_i$ is the ion number density, $q_i$ is the ion charge, and c is the speed of light. The comparison to the Coulomb mean free path ($\lambda_{mfp}$) indicates that the interaction between the explosive ion species and ambient ions species is not influenced by collisions. The same cannot be said about electron-ion or electron-electron collisions in the laboratory setting.

The number of laboratory experiments has been growing rapidly in recent years to match the comprehensive theoretical and computational efforts in understanding this interaction. Prior experiments have utilized a geometry where the LPP expands quasi-perpendicularly to the magnetic field, but at sub-Alfvénic velocity. These experiments investigated the formation of a diamagnetic cavity and jetting of the LPP from curved polarization fields [87, 22], and observed surface striation growth on the diamagnetic cavity edge, allowing for additional cross field transport of LPP ions relevant to the AMPTE experiments [22]. Additional experiments involving a $M_A = 1$ LPP examined the electrostatic fields which mediate LPP-ambient coupling in the limit of $\frac{L}{\delta_i} M_A << 1$, where L is a characteristic scale length associated with coupling.

Experiments utilizing a higher energy laser to drive faster plasmas have explored the change in coupling when the energetic expansion is super-Alfvénic. These revealed the effects of ambient ion mass to the diamagnetic cavity formation and radiated shear Alfvén wave [65], directly observed the LPP-ambient coupling in the limit of $\frac{L}{\delta_i} M_A > 1$ where Larmor term dominates [9], and have for the first time produced sufficient coupling in the super-Alfvénic limit to launch a quasi-perpendicular collisionless shock relevant to the bow-shock surrounding Earth [64].

Despite the improved understanding of these interactions in both the sub- and super-Alfvénic regimes, one aspect that has proven to be challenging to investigate in the laboratory experiments mentioned above is to measure the LPP ion velocities with high degree of spatial and temporal resolution. Here, I detail the development of a laser induced fluorescence (LIF) diagnostic specifically designed to measure the transient, hot plasma with high spatial and temporal resolution. This measurement is unique from many other LIF schemes in that it requires a large bandwidth (6.5 $cm^{-1}$)

probe laser, is only susceptible to a two-level scheme, and requires extensive collisional-radiative modeling to examine time-dependent energy level populations that dictate when the method is feasible. This LIF diagnostic was utilized to map the LPP ion velocities as it couples to the ambient, magnetized plasma in both a sub-Alfvénic and super-Alfvénic expansion.

In the sub-Alfvénic expansion, LPP ions were observed to decelerate in the region where large magnetic gradients couple energy from the LPP to the magnetic fields. The velocity maps allowed for a well initialized particle-in-cell (PIC) simulation to help complete the picture of energy transferring to the magnetized ions through the magnetic pressure.

In the super-Alfvénic expansion, the LPP was observed to focus into a jet-like structure along the primary direction of travel and across the magnetic fields. The cross-field ion currents induce electric fields that accelerate ambient plasma consistent with an E × B drift. The drifting ambient ions and streaming LPP ions developed a secondary magnetic structure, or blob, that extends well past the main diamagnetic cavity.

## 1.2 Basic Equations for Quasi-Perpendicular Collisionless Coupling

This section reviews some of the basic equations describing plasma behavior relevant to this work. Plasma is an ionized gas where the electrons have sufficient energy so as to be separated from the nucleus of the ions in a state of quasi-neutrality. Given the charged nature of plasma particles, the dominant interactions that determine the dynamics are long range Coulomb interactions. The necessary condition for a plasma is that the number of particles in a Debye sphere has to be very large ($N_D = 4\pi n_D^3/3 >> 1$ where $\lambda_D^2 \equiv T_e/4\pi n_e e^2$). This allows for a continuum approximation to be made which leads to a fluid like description of a plasma. Here $n_e$ is the electron number density and $T_e$ is the electron temperature. The behavior is dominated by collective effects over the entire plasma distribution as opposed to treating each particle independently. Two important equations are that of continuity and conservation of momentum

$$\frac{\partial n_s}{\partial t} + \nabla \cdot (n_s \mathbf{v}_s) = 0 \tag{1.1}$$

$$m_s n_s \left( \frac{\partial v}{\partial t} + (v \cdot \nabla)\, \mathbf{v} \right) = Z_s e n_s \left( \mathbf{E} + \mathbf{v} \times \mathbf{B} \right) - \nabla \cdot \mathbf{P} \tag{1.2}$$

where $\mathbf{P}$ is the pressure tensor. As each of the moments of the Vlasov equation [79] are dependent on the subsequent moment, a closure condition must be established that often comes in the form of a source term.

Each quantity is denoted as the sum of the averaged quantity $\langle Q \rangle$ plus a fluctuating component $\delta$Q. This allows the linearization of each moment when solving. A simplifying assumption that is often made is an Ansatz that solutions are in the form of an exponential $\exp i(\mathbf{k} \cdot \mathbf{x} - \omega t)$, which allows the use of Fourier transforms to substitute any time derivatives as $\partial / \partial t = -i\omega$ and spatial derivatives as $\nabla = i\mathbf{k}$.

In addition, Maxwell's equations

$$\nabla \cdot \mathbf{E} = 4\pi\rho \tag{1.3}$$

$$\nabla \cdot \mathbf{B} = 0 \tag{1.4}$$

$$\nabla \times \mathbf{E} = -\frac{1}{c} \frac{\partial \mathbf{B}}{\partial t} \tag{1.5}$$

$$\nabla \times \mathbf{B} = \frac{4\pi}{c} \mathbf{J} + \frac{1}{c} \frac{\partial \mathbf{E}}{\partial t} \tag{1.6}$$

will be used, of which Faraday's (eqn. 1.5) and Ampere's (eqn. 1.6) laws are used to a greater extent.

Combining these equations results in the necessary description of plasma behavior including

dispersion relations and the evolution of the fields that mediate coupling in these systems. Analysis in this framework utilizes a "hybrid" plasma model, in which the electrons are treated as single charge-neutralizing massless fluid, while the ions are treated kinetically [41, 3]. The validity of which is discussed at length by Leroy et al. [55].

The electron fluid evolution follows from the conservation of momentum equation

$$m_e n_e \frac{d\mathbf{v}_e}{dt} = -\nabla p_e - e n_e \left( \mathbf{E} + \frac{1}{c} \mathbf{v}_e \times \mathbf{B} \right) \tag{1.7}$$

where $m_e$, $n_e$, $\mathbf{v}_e$, $p_e$, and e are the electron mass, density, velocity, pressure and charge. In the hybrid limit we assume that over the time scales relevant for ion momentum and energy exchange, the electrons responds nearly instantaneously due to the negligible inertia compared to ions. This allows the limit of $m_e \rightarrow 0$ approximation, which leads to the laminar electric field equation

$$\mathbf{E} = -\frac{1}{e n_e} \nabla p_e - \frac{1}{c} \mathbf{v}_e \times \mathbf{B}. \tag{1.8}$$

It is useful to replace the electron velocity in this equation via Ampere's law, in which we assume that the high frequency, transient displacement current is ignored. From this one finds

$$\nabla \times \mathbf{B} = \frac{4\pi}{c} \left( \sum_i Z_i e n_i \mathbf{v}_i - e n_e \mathbf{v}_e \right). \tag{1.9}$$

Assuming quasi-neutrality( i.e. $n_e = \sum_i Z_i n_i$), we can solve the above equation for $v_e$ and substitute it into equation 1.7. This results in

$$\mathbf{E} = - \underbrace{\frac{\nabla p_e}{e \sum_i Z_i n_i}}_{\text{electron pressure}} - \underbrace{\frac{\mathbf{B} \times (\nabla \times \mathbf{B})}{4\pi e \sum_i Z_i n_i}}_{\text{magnetic structure}} - \underbrace{\frac{\sum_i Z_i n_i \mathbf{v}_i \times \mathbf{B}}{c \sum_i Z_i n_i}}_{\text{Larmor}}. \tag{1.10}$$

The electric field is described by three components: the electron pressure gradient, magnetic structure, and Larmor terms as they will be referred to. The magnetic structure term is the electrostatic component due to space charges, and the Larmor term is an induced electric field from ion motion. In chapter 2 each term will be discussed more thoroughly.

It is important to note that we have assumed only one electron density $n_e$, and do not differentiate between the LPP electrons and ambient electrons. For the time scales that are relevant for ion-ion coupling this is a valid assumption since the LPP electrons are highly collisional and become indistinguishable from the ambient electrons a short time after inception. This equation for the laminar electric field can also be derived from the generalized Ohm's law, which is described in the theory section.

## 1.3 Collisionless Coupling and Collisionless Shock Formation

While the experiments performed here are focused on the LPP-ambient coupling in terms of identifying and understanding the coupling mechanisms fundamentally, the ultimate goal is to create sufficient coupling so as to create a quasi-perpendicular collisionless shock in the laboratory [63].

Shocks are theoretically well understood (see [17, 85, 84]) and are characterized by having an abrupt transition from supersonic to subsonic flows, or in the case of a magnetized collisionless shock, super-magnetosonic to sub-magnetosonic flows. This abrupt change in flow is known as a "jump condition" and works to transfer directed kinetic energy into thermal energy. In classic collisional shocks, the transition takes place on scale lengths of around $\lambda_{mfp}$. The type of collisionless shocks that are relevant to this work dissipate energy on length scales of less than an ion inertial length.

An additional difficulty presents itself in extrapolating our understanding of gas dynamics to collisionless shocks when including complex behaviors such as multiple wave modes, non-Maxwellian distributions leading to instabilities, and energetic particle distributions [17]. The basic processes

of energy arriving at a shock faster than it can be dissipated is valid across the various types of shocks. As this wave steepening cannot continue indefinitely, a method for energy dissipation is required. Methods for energy dissipation in collisionless shocks have been well studied and intrinsic differences exist when the velocity scale changes from below to above the critical value ($M_{A,crit} \sim 3$).

In order to create a collisionless shock in the laboratory several conditions must be met in order for a super-magnetosonic, or in our case a super-Alfvénic ($c_s << v_A$) driver plasma to "shock" an ambient magnetized plasma. It is shown in the following chapter that the driver plasma stops at a given distance over which the ambient particles must be accelerated and gyrate by a quarter orbit, as will be shown below. In other words, the LPP ions must sufficiently couple to the ambient plasma which leads to the decoupling condition [46]

$$\Omega_a \delta t_d < \alpha < 1, \alpha \equiv \frac{\pi}{2} \frac{Z_d n_d}{(Z_d n_d + Z_a n_a)} \tag{1.11}$$

where $\delta t_d$ is the temporal duration of the LPP (or debris plasma) ion current density, $Z_i$ is the charge state of the driver or ambient plasma, and $n_i$ is the density of each plasma species. If this decoupling condition is met, the transfer of energy and momentum from the explosive plasma to the ambient magnetized plasma ceases. The right hand limit ($\alpha < 1$) can be understood as charge density limiting the coupling. In the limit of large Mach numbers ($M_A > 1$) the electric field created in the interaction of the cross field ion current is directed in the azimuthal direction. If the ambient electron density is sufficiently small, the large electric fields accelerate the ambient ions to speeds greater than or equal to the LPP in $1/4$ of a gyroradius, thus coupling the LPP ions to the ambient ions. If the electron density is too high, the electric fields are shielded by the fast moving electrons and coupling is reduced. In reality, this condition can be slightly relaxed given the radially outward pointing electric fields created by the magnetic pressure term. This equation assumes that the only mechanism coupling energy to the ambient ions is via the Larmor term, which initially drives ions

azimuthially and after $1/4$ gyroperiod redirects them radially. Since the magnetic pressure term drives ions to have an initial radial expansion, the assumed negligible initial radial velocity is not true for moderate Mach numbers.

The left hand limit represents the effects of a finite pulse width of the LPP. The ambient ions must be sufficiently magnetized within the pulse of the LPP driver plasma. If the ambient ion gyroradius exceeds the pulse length on the driver plasma it decouples.

## 1.4 Scope of Dissertation

This dissertation presents the results of recent experiments utilizing an LPP expanding into the preformed, magnetized plasma of the LAPD to understand the different regimes of laminar collisionless coupling between the two plasma species. The dominant mechanism that exchanges energy from the LPP to the ambient plasma is dictated by the Alfvénic Mach number of the LPP flow into the ambient plasma. The magnetic structure term dominates in the case of sub-Alfvénic expansion and the Larmor term in the case of super-Alfvénic expansion.

Chapter 2 (Theory) provides a theoretical overview of how the LPP is formed and expands into the ambient magnetized plasma. Important length scales dictating this interaction are derived as well as the different sources for the transfer of energy and momentum from the LPP to the ambient plasma. The intensification of a singly ionized helium spectral line by energetic electrons is briefly discussed.

Chapter 3 (Experimental Setups) discusses the different setups and devices that are used in the experiments. The Large Plasma Device (LAPD) where the bulk of the experimental work has been completed is described in detail. The Phoenix target chamber is discussed briefly as a test site for diagnostic development. The diagnostics used in the experiments are discussed, with a heavy emphasis on the new laser induced fluorescence diagnostic for explosive carbon laser produced plasma that has been developed from scratch.

Chapter 4 (sub-Alfvénic Coupling) details the experiment in which the magnetic structure component of the laminar electric fields dominates. It is shown that in the sub-Alfvénic limit the flow of energy is not directly coupled from the LPP to the ambient plasma, but uses the magnetic energy as an intermediary step to transfer energy. The experimental data is complemented by 3D particle-in-cell (PIC) simulations to contextualize the results and give a broader understanding to the mechanism.

Chapter 5 (super-Alfvénic Coupling) details the experiment in which both the magnetic structure term and the Larmor term play important roles in the dynamics and collisionless coupling. The magnetic structure term helps to confine the plasma transverse to the primary direction of travel and collimates the flow into a jet-like structure. This collimation leads to an enhanced current density later in time that develops the Larmor electric fields that directly couple the LPP to the ambient plasma. This develops a charge separation in the ambient plasma that creates a smaller diamagnetic cavity that extends past the main cavity.

Chapter 6 (conclusions) summarizes the results of this work and discusses potential experiments in the future.

# CHAPTER 2

# Theory

## 2.1 Laser-Produced Plasmas

When radiation from a laser of sufficient intensity is focused upon the surface of a solid target, a hot and dense plasma is formed. This laser-produced plasma (LPP) is highly transient and is characterized by steep and rapidly evolving density and temperature gradients, and ions of various charge states and velocities. Creating an energetic plasma by laser ablation of a solid target is a common technique used in many laboratory settings from laser driven inertial confinement fusion [42, 50] to laboratory astrophysics [72, 73, 61, 26, 43, 22]. Despite the wide use of LPP drivers across disciplines, the precise characterization and control of these drivers remain an active field of study. In the following I give a brief overview of the laser plasma generated in this experiment.

### 2.1.1 Laser-Target Interaction

The process of a nanosecond ($10^{-9}$ s) pulse laser interacting with a solid target is described by three distinct regions [92]. The laser interacts with the target and creates a plasma. Shortly after this, but still within the laser pulse duration, the laser interacts with the high density material that was just ejected from the surface. After the laser pulse has ended, the hot and dense plasma freely expands away from the target. These are summarized in figure 2.1.

At t = 0 ns, the high intensity laser is focused onto the graphite (C) or high density polyethylene (HDPE, $C_2H_4$) target surface at intensities up to $1 \times 10^{12}$ W/cm$^2$. The electric fields induce high

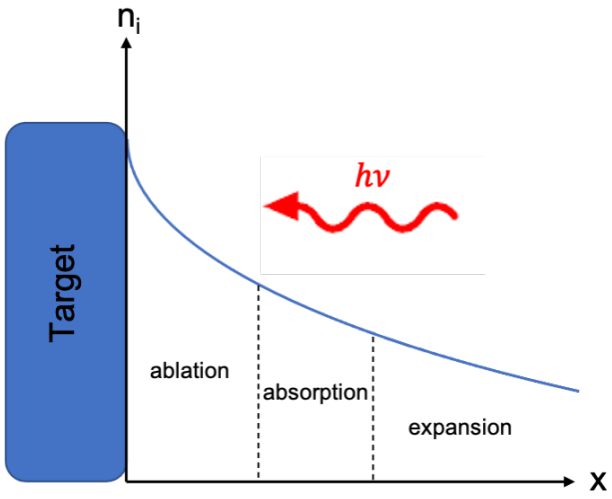


Figure 2.1: Illustration of laser ablation of a solid target by irradiation with high intensity light. Laser light irradiates the target surface from the right hand side. The solid blue block represents the unaffected target region, the ablation zone where the plasma is highly collisional, and as a result, isothermal. The initial plasma that is created exists well above the critical density which allows the plasma to absorb the incident laser light through a process referred to as inverse-bremsstrahlung. The final zone is the expansion zone where the density has dropped to the point where laser light is no longer absorbed and the plasma expands rapidly.

temperatures that rapidly eject electrons and subsequently ions at near solid densities (n $\sim 10^{23}$ $cm^{-3}$). This initial state of the LPP is well above the critical density for the laser irradiating the target ($n_{crit} = 1.1 \times 10^{21}/\lambda^2[\mu m]$ $cm^{-3} \sim 1 \times 10^{21}$ $cm^{-3}$ for 1053 nm light) [67]. This sets up a region near the target through which the laser light cannot transmit and all laser energy is either absorbed or reflected [81]. The light absorbed through a process called inverse bremsstrahlung [60] results in a isothermal plasma distribution. The light reflected is negligible for plasmas created in this intensity and frequency regime [30].

At very early times, the high density allows for collisions and satisfies the local thermodynamic equilibrium (LTE, or McWhriter) condition [59]. This sets up a nearly Gaussian velocity spread about the average speed for each ion charge state. The initially highly ionized plasma can recombine and this free bound transition results in a continuum in the emitted spectra which has been used to measure the temperature of the electrons in the LPP [7]. These recaptured electrons cascade to lower electron orbitals until they reach either the ground or a metastable state. The bound electrons

can be excited by collisions or photon absorption.

The LPP is directed perpendicularly to the surface of the target independent of the angle of incidence of the ablation laser. This results in an oblate spheroid shaped plasma. The electrons expand at higher velocities due to the lower mass, which drives a charge separation induced electric field. This ambipolar electric field accelerates the trailing ions proportional to their charge-to-mass ratio, setting up downstream velocity distributions that depend directly upon q/m. For the HDPE targets used, this would result in protons having the highest velocity with all carbon ions trailing.

As the plasma continues to expand, a threshold value is crossed where it is no longer in LTE and the velocities and charge states reach a steady-state value. This is understood as the electron-ion and ion-ion collision rate trending to zero. If the plasma is expanding into an unmagnetized vacuum, the expansion is perfectly adiabatic and remains approximately Gaussian. As long as the plasma expands unhindered, the density decreases proportional to the geometric expansion in 3D ($n_e \propto t^{-3}$).

### 2.1.2 Expansion Into Magnetized Plasma

Prior experiments with a similar setup have explored the diamagnetic cavity formation of a sub-Alfvénic [87] and super-Alfvénic [66] expanding LPP. Here I summarize the key results.

When considering the expansion of an LPP into a magnetized plasma, the impact of the magnetic fields and ambient ions must be accounted for. In the picture of the plasma expanding into vacuum, the laser produced electrons stream ahead of the ions. After a short period, the ions and electrons reach a state of quasi-neutrality and expand ballistically.

Introducing a magnetic field breaks the symmetry seen in the expansion into vacuum. This is particularly evident when the LPP expands across the magnetic field in the quasi-perpendicular geometry. It is useful to model the piston plasma as a spherically symmetric expansion into a magnetized plasma with a uniform magnetic field $B_0$ or $B_{ext}$. This simplified model allows for

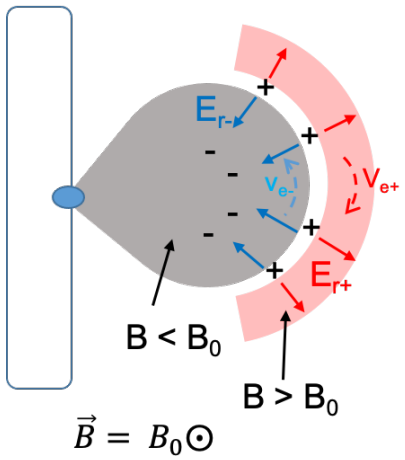


Figure 2.2: Illustration of diamagnetic cavity formation. The charge separation between the magnetically confined LPP electrons and free streaming LPP ions induces an E × B diamagnetic current in the electron population that expels the external magnetic field. A qualitatively similar process sets up an outward facing radial electric field between the LPP ions and ambient electrons that produces a magnetic compression at the leading edge of the expansion. The LPP cloud expands in a quasi-perpendicular geometry to the ambient magnetic field. The LPP cloud is assumed, at early times, to be azimuthially symmetric.

a few characteristic length scales to be derived more easily. The radially expanding LPP shell consists of $N_0$ ions, with charge $Z_d$, mass $m_d$, at an initial bulk velocity $v_{d,0}$. The ambient plasma has a homogenous density of $n_a$, mass $m_a$, and charge $Z_a$.

Invoking quasi-neutrality, one finds

$$n_e = Z_a n_a + Z_0 n_d = Z_a n_a + \frac{3 Z_0 N_0}{4\pi R^3} = Z_a n_a (1 + (R^*/R)^3) \tag{2.1}$$

where $n_e$ is the overall electron density, and $R^* = (3N_0 Z_0 / 4\pi Z_a n_a)^{1/3}$ is defined to be the equal charge radius. This radius represents the volume the LPP expands to where an equal amount of charge of the ambient plasma has been swept over [3]. This quantity is useful when discussing the coupling criteria. This model also assumes that the magnetic field energy of the ambient plasma ($B_0^2/8\pi$) is small compared to the directed kinetic energy of the LPP ($\frac{1}{2} N_0 m_d v_d^2(t)$). In other words, the LPP ion kinetic beta $\beta_{i,k} = 4\pi N_0 m_d v_d^2(t)/B_0^2 >> 1$.

In the presence of a magnetic field, the electrons quickly become magnetically confined (~ ten's of ns) as the gyroradius of electrons is small compared to the system size. The relatively unmagnetized LPP ions ($\rho_l = v/\Omega_l >$ L) stream past the electrons resulting in an electric field directed inwards as shown by $E_{r-}$ in figure 2.2. In combination with the external magnetic field, the electron population experiences an $\mathbf{E} \times \mathbf{B}$ drift. These currents enhance the electron pressure gradient flow ($\nabla P_e \times \mathbf{B}$) in a manner that expels the externally applied magnetic field. This process results in a region of lower magnetic field called the diamagnetic cavity [87].

Ignoring the ambient plasma entirely, the expansion of the LPP is halted at the magnetic stopping radius, $R_{b,0}$, which is derived from the energy balance equation

$$\frac{1}{2} N_0 m_d v_{d,0}^2 = \frac{1}{2} N_0 m_d v_d^2(t) + \frac{B_0^2}{8\pi} \frac{4\pi}{3} R^3(t) \tag{2.2}$$

$$R \equiv R_{b,0} = \left( \frac{3 N_0 m_d v_{d,0}^2}{B_0^2} \right)^{1/3} . \tag{2.3}$$

This radius, $R_{b,0}$, is the maximum radius the LPP ions could expand to before all kinetic energy was converted into expelling the magnetic field [5].

A similarly produced, but oppositely directed current structure is formed ahead of the streaming ions that enhances, or compresses the local magnetic field [92, 9]. The time varying magnetic field of the diamagnetic cavity causes an induction electric field via Faraday's law which is primarily directed in the azimuthal direction. An additional electric field is created to oppose the v × B Lorentz force that deflects moving ions and electrons in opposite directions. The Faraday and Lorentz generated electric fields combine in the azimuthal direction and E × B drift the ambient electrons radially outward. This outward drift leads to an outward directed polarization electric field which creates an anti-diamagnetic current in the ambient electrons ahead of the streaming LPP ions. Ignoring all energy dissipation processes, this effect would continue to steepen the

magnetic field until the ions stop. The maximum magnetic field compression far downstream has been experimentally observed to be proportional to the Alfvénic Mach number ($M_A = v_d/v_A$) up to the maximum value of $B_{downstream}/B_0 \sim 4$ [17]. Recent experiments have shown the magnetic field compression within the shock structure to be directly proportional to the Mach number [75].

In the case where energy and momentum is also transferred to the ambient ions, the stopping radius is reduced at higher Mach numbers. From similar energy conservation arguments it follows that

$$\frac{1}{2}N_0 m_d v_{d,0}^2 = \frac{1}{2}N_0 m_d v_d^2(t) + \frac{B_0^2}{8\pi}\frac{4\pi}{3}R^3(t) + \frac{m_a n_a v_a^2(t)}{2}\frac{4\pi}{3}R^3(t) \tag{2.4}$$

$$R \equiv R_b = R_{b,0}\left(1 + M_A^2\right)^{-1/3}. \tag{2.5}$$

Taking the limit where coupling to the magnetic fields is negligible and all of the initial energy is transferred into the directed kinetic energy of the ambient ions reveals the quantity known as the equal mass radius $R_M$. Equating the total LPP mass to the mass of ambient ions at radius $R_M$ leads to:

$$N_0 m_d = n_a m_a \frac{4\pi}{3}R_M^3, \quad R_M^3 = \frac{3N_0 m_d}{4\pi n_a m_a}. \tag{2.6}$$

Physical insight as to the dynamics is gained by evaluating the ratios of the magnetic stopping distance, equal charge radius and equal mass radius:

$$\left(\frac{R_{b,0}}{R_M}\right)^3 = \frac{3N_0 m_d v_{d,0}^2}{B_0^2}\frac{4\pi n_a m_a}{3N_0 m_d} = M_A^2 \tag{2.7}$$

$$\left(\frac{R_{b,0}}{R^*}\right)^3 = \frac{3N_0 m_d v_{d,0}^2}{B_0^2}\frac{3N_0 Z_d}{4\pi Z_a n_a} = \frac{Z_a m_d}{Z_d m_a} M_A^2 \tag{2.8}$$

$$\left(\frac{R_M}{R^*}\right)^3 = \frac{3N_0 m_d}{4\pi n_a m_a}\frac{3N_0 Z_d}{4\pi Z_a n_a} = \frac{Z_a m_d}{Z_d m_a}. \tag{2.9}$$

In the limit of a highly super-Alfvénic driver ($M_A \gg 1$) the equal mass radius determines the cavity size in comparison to the magnetic stopping radius, indicating that the LPP ions decelerate largely due to coupling to the ambient ions. In the opposite limit of a sub-Alfvénic driver ($M_A \ll 1$), coupling is dominated by expelling the ambient field. In the case of a marginally sub- or super-Alfvénic interaction ($M_A \sim 1$) both processes play an important role.

The relatively simple arguments constructed above helps define limits and important scaling parameters. The underlying mechanisms that transfer energy from the driver plasma to the ambient fields and particles is discussed in the following section. Care must be taken when using these formulae to describe the following experiments as the LPP expansion is not spherically symmetric. The distance from the target to the edge of the diamagnetic cavity is more accurately the diameter, not the radius.

## 2.2 Coupling Mechanisms

As the explosive LPP expands into the magnetized ambient plasma, electric fields develop. It is useful to divide these into separate categories, two of which are: laminar [46, 5, 35] and turbulent [58, 68, 71, 25]. Laminar coupling is mediated by fields that exhibit a smooth and ordered structure with the bulk features being quite repeatable. Turbulent coupling is characterized by fields that exhibit chaotic or irregular patterns and lead to the generation of instabilities. These are often non-repeatable phenomena and are more challenging to study. Both types of fields can suppress or enhance the ambient magnetic field and affect particle motion.

In the following section the dominant mechanisms that create the electric fields that transfer energy from the LPP ions to the ambient ions are reviewed.

### 2.2.1 Laminar Electric Fields

Laminar electric fields are large scale, coherent fields that mediate collisionless coupling (eqn. 1.10).

These electric fields are the result of electron pressure gradients (the first term in Eqn. 1.10), spatial variations in the magnetic field structure (the second term in Eqn. 1.10), and ion currents across magnetic field lines (the third term in Eqn. 1.10 often referred to as the Larmor term). These electric fields affect the motion of the LPP and ambient plasma particles alike.

The electron pressure gradient points radially outwards from the target surface, where the high density laser produced electrons repel one another.

The Larmor term is understood through the lens of quasi-neutrality. The opposing directions of the gyration of the ions and electrons sets up a spatial charge separation anywhere there is a sufficiently large magnetic field. This sets up an electric field which attempts to reduce the charge separation. The field attempts to reduce the charge separation of the LPP ions and electrons, but acts on the ambient ions as well. A cartoon is shown in figure 2.3 that shows the direction of the Larmor fields and the dependence on magnetic field.

The second term is a results of substituting Ampere's law into the Hall current term ($\mathbf{E} = \mathbf{J}\times\mathbf{B}/en_e$). Re-framing the "magnetic structure" term in this way allows for it to be measured by available diagnostics. We can further understand this term by using vector identities to brake it up into two components: a magnetic pressure and magnetic tension term

$$-\frac{1}{4\pi e n_e}\mathbf{B}\times(\nabla\times\mathbf{B}) = -\frac{1}{4\pi e n_e}\left(\nabla\frac{B^2}{2} - (\mathbf{B}\cdot\nabla)\mathbf{B}\right). \tag{2.10}$$

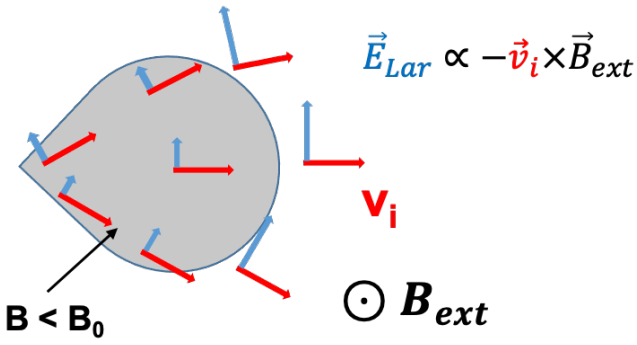


Figure 2.3: Illustration of the Larmor term in the laminar electric field equation. The ion velocity is directed radially away from the laser spot on target. LPP ions interact with the ambient magnetic field and create an electric field in the azimuthal direction. Physically, the electric field is created in direct opposition to the Lorentz force which attempts to divert the electron and ion flow. The magnitude of $E_{lar}$ is reduced in the diamagnetic cavity where the magnetic field is reduced. This was first measured by Bonde et al. [13].

The magnetic pressure term ($\nabla B^2/2$) forces ions down magnetic field gradients. This term acts along the edge of the diamagnetic cavity where large magnetic field gradients exist, and dominates the magnetic tension term. This allows the magnetic structure term to be approximately equated to the magnetic pressure term.

The ratio of the Larmor term to the magnetic structure term scales with the Alfvénic Mach number

$$\frac{|\frac{1}{en_e c}\sum_i Z_i n_i \mathbf{v}_i \times \mathbf{B}|}{|\frac{1}{4\pi e n_e}\mathbf{B} \times (\nabla \times \mathbf{B})|} \sim \frac{L}{d_i} M_A \tag{2.11}$$

where $L$ is the system size and $d_i$ is the ion inertial length. This demonstrates that even in the case of large Mach numbers, the magnetic structure term can outweigh the Larmor term if the ion inertial length is large compared to the system size.

The ratio of the electron pressure gradient term to the magnetic structure term scales as $\beta_e = 8\pi p_e/B^2$ [5]. At early times, of about the time at which electrons become magnetically confined, the electron pressure gradient dominates all other components in this electric field equation. The pressure gradients are immense and the subsequent field act to accelerate both the LPP ions and ambient ions alike. Since the density of LPP ions far outnumber the density of ambient ions at

this early time, the energy is imparted onto the LPP ions to a greater degree. Breaking down the electron pressure gradient term reveals

$$\frac{\nabla p_e}{n_e e} = \frac{T_e \nabla n_e}{e n_e} + \frac{\nabla T_e}{e}. \tag{2.12}$$

As the LPP rapidly expands, the temperature and density gradients decrease. Evaluating equation 2.12 with approximate, but realistic values for times greater than 100 ns ($\nabla n_e/\mathrm{n}_e \sim 1-5$ cm, $\mathrm{T}_e \sim 5$ eV, $\nabla T_e \sim 10$ eV/cm) we see that this field only accounts for $2-10$ V/cm compared to the hundred's of V/cm that are created by the magnetic structure term and cross-filed ion current term. This is consistent with the findings of prior, similar experiments [12].

It is interesting to note that the laminar electric field equations can also be derived from the generalized Ohm's law, as has been done in prior studies [13]. This provides more physical insight and so I briefly review the process. Starting with Ohm's law with terms of order $\mathrm{m}_e/\mathrm{m}_i$ being ignored we find

$$\mathbf{E} = \frac{\partial_t \mathbf{J}}{\omega_{pe}^2 \epsilon_0} + \frac{\nabla \cdot (\mathbf{VJ} + \mathbf{JV})}{\omega_{pe}^2 \epsilon_0} - \mathbf{V} \times \mathbf{B} + \frac{\mathbf{J} \times \mathbf{B}}{e n_e} - \frac{\nabla p_e}{e n_e} + \eta \mathbf{J}. \tag{2.13}$$

The first two terms are negligible for the spatial and temporal scales considered here. The final term, the resistive term, is negligibly small for the expansion phase of a hot plasma. It contributes a small amount later in time, but is still weak compared to the other sources ($\sim$ 0.1 V/cm for $\eta_{sp} = 0.014\ \Omega$ cm) where $\eta_{sp} = \frac{4\sqrt{2\pi}}{3} \frac{Ze^2 m_e^{1/2} ln\Lambda}{(T_e)^{3/2}}$ is the Spitzer resistivity and $\ln\Lambda$ is the Coulomb logarithm.

The velocity $\mathbf{V}$ in the third term is mass weighted, so we can, to a good approximation, replace it with a sum over the ion velocities. Making use of Ampere's law while ignoring the displacement current component $\mathbf{J} = \frac{c}{4\pi} \nabla \times \mathrm{B}$ leads to the similar form:

$$\mathbf{E} = -\frac{\sum_i Z_i n_i \mathbf{v}_i \times \mathbf{B}}{c \sum_i Z_i n_i} + \frac{1}{4\pi e \sum_i Z_i n_i} (\nabla \times \mathbf{B}) \times \mathbf{B} - \frac{\nabla p_e}{e \sum_i Z_i n_i} \tag{2.14}$$

where quasi-neutrality has been invoked to replace $n_e$ with $\sum_i Z_i n_i$. This results in the same laminar electric field derived with the inertia-less electron "hybrid" model.

The V × B and J × B components are often times referred to as the Lorentz and Hall terms respectively, where the Lorentz term is the previously discussed cross-field ion current term and the Hall term has previously been referred to as the magnetic structure term. The Hall term is a result of ions and electron motion decoupling and moving separately.

When discussing electric field components, it is useful to split the term into the electrostatic ($\nabla \times \mathbf{E}_{st} = 0$ or $\mathbf{E}_{st} = -\nabla\phi$) and induced ($\nabla \cdot \mathbf{E}_{ind} = 0$ or $\mathbf{E}_{ind} = -\partial_t \mathbf{A}$) components, where $\phi$ is the electrostatic potential and $\mathbf{A}$ is the vector potential.

### 2.2.2 Decoupling

The mechanisms that collisionlessly transfer energy from an explosive LPP to a magnetic ambient plasma have been shown above. This coupling cannot happen instantaneously. The longer the criteria for coupling are met, the greater the energy transfer. In this section the dynamics that dictate the duration until the two species decouple from one another are explored, as initially discussed in Hewett et al. [46].

The first limit defining the decoupling represents having sufficient charge density. In the super-Alfvénic limit, the dominant component of the electric field is directed in the azimuthal direction, perpendicular to both the magnetic field (z) and LPP direction of travel (x). The field is estimated by:

$$E_\theta = \frac{Z_d n_d}{Z_d n_d + Z_a n_a} v_{d,r} B_z \tag{2.15}$$

where $Z_i$ and $n_i$ are the charge and densities of the ambient and debris plasmas, $v_{d,r}$ is the radially directed component of the LPP ion velocity, and $B_z$ is the magnetic field. This field induces an E × B drift of the ambient ions and electrons. The motion of the ion population begins parallel to the electric field. The response of the ambient ions can then be expressed by

$$\frac{\Delta v_a}{\Delta t} = \frac{Z_a e}{m_a} E_\theta. \tag{2.16}$$

The ions initially accelerated in the $\hat{\theta}$ ($\hat{y}$ in Cartesian coordinates) direction gyrate into the $\hat{r}$ ($\hat{x}$ in Cartesian coordinates) direction by one quarter of a gyro period, or $\Delta T = \pi/2\omega_{c,a}$. If the ambient ions fail to accelerate to a velocity at or greater than the LPP ions by this time, they decouple. This is expressed as:

$$\frac{\pi}{2} \frac{Z_d n_d}{Z_d n_d + Z_a n_a} < 1 \tag{2.17}$$

which hides the importance of the magnetic field in this interaction.

The second criteria is known as the finite-pulse-length threshold and is representative of the degree of magnetization of the ambient ions. The end result is similar, in that the ions decouple by trailing behind the piston plasma, but the mechanism through which this decoupling happens is different. In this limit, the finite length ($\delta t_{lpp}$) of the piston plasma must be larger than the ambient ion gyroradius. If the gyroradius is too large, then the accelerated ambient ions gyrate back to the blow-off axis behind the piston plasma and stop the coupling. The coupling increases with q/m of the ambient ions [49]. This limit is expressed as

$$\frac{\pi}{2} \frac{Z_d n_d}{Z_d n_d + Z_a n_a} > \omega_{c,a} \delta t_{lpp}. \tag{2.18}$$

The interaction dynamics are quite sensitive to small changes in the parameters of either species.

### 2.2.3 Helium Intensification by Energetic Electrons

As the LPP couples to the ambient magnetized plasma, observing the motion of the ambient helium ions allows for an understanding of the transfer of energy from the driver plasma to the magnetized plasma. However, in the steady-state conditions of the LAPD, the self emission of the helium ion plasma is virtually undetectable on the timescales (~ tens'-hundred's of ns) over which the coupling occurs.

Wavelength filtered imaging reveals that when the energetic LPP ions stream through the ambient helium plasma there is a significant intensification of the $He^+$ 486.6 nm spectral line in response. The spatial location of the intensification corresponds to the leading edge of the LPP ions, but separates after a short period of time. The lens is focused on the plane where maximum coupling is expected, but light along the entire line of sight is collected by the imaging system.

The emission of the $He^+$ 486.6 nm spectral line requires the transition of a bound electron from the n = 4 to the n = 3 quantum state. A detailed collisional-radiative analysis performed by Bondarenko et al. [9] has revealed that the primary mechanism for repopulating n = 4 in the ambient plasma is collisional excitation from the ground state (n = 1) with electrons of kinetic energy greater than or equal to 51 eV. The spatial correspondence of the $He^+$ 486.6 nm spectral line with the magnetic compression suggests that the electrons involved in the anti-diamagnetic current ahead of the LPP flow are also responsible for the repopulation of the n = 4 quantum state in the $He^+$ ions.

The spontaneous decay rate of this line is ~ ten ns. As emission from this transition is observed for many microseconds, the electrons must be interacting with the helium and repopulating the n= 4 state for an extended period of time, up to many microseconds after the expansion of the diamagnetic cavity.

This intensification allows for the observation of this $He^+$ line on the nanosecond scale, which is

necessary to see the response of the ambient ions to the LPP driver plasma. It is limiting in that the effects can only be observed in regions where there are energetic electrons and therefore a more robust method of observation would be preferable for future measurements. This technique is still valid as a qualitative method for observing the reaction of helium ions to the laser plasma.

# CHAPTER 3

# Experimental Setups

## 3.1 Large Plasma Device

These experiments take advantage of the unique combination of a high power laser system and the LAPD [36] in order to investigate the interaction between an explosive laser produce plasma and a magnetized background plasma. The experiment replicates conditions similar to astrophysical plasmas at a high repetition rate ($\sim$ 1 Hz) compared to many other similar experiments. The LAPD provides a large scale (18 m long, by ⌀1 m) well characterized, current free, steady state ($\sim$ 10 ms), highly-repeatable magnetized ambient plasma. Large magnetic coils along the length of the machine generate configurable magnetic fields (300 – 2000 Gauss) that radially confine the plasma. A ⌀38 cm lanthanum hexaboride ($LaB_6$) cathode on the south side (far left in figure 3.1) of the machine generates a plasma ($n_a \sim 1 \times 10^{12} - 3 \times 10^{13}$ cm$^{-3}$) centered on the axis. The LAPD can generate a plasma from a variety of gasses (typically $H_2$, He, Ne or Ar). A background fill of helium was chosen for the experiments in order to balance the repetition rate with the degree of magnetization of the background. At this time is was uncertain if hydrogen gas would be able to be

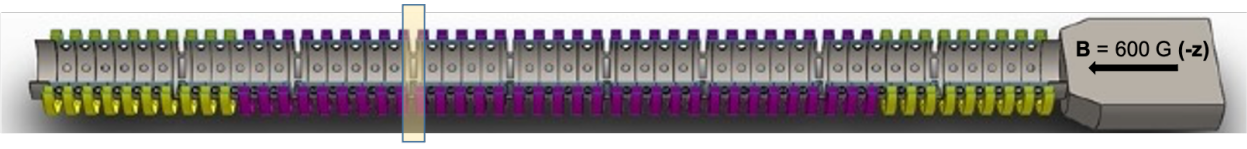


Figure 3.1: Schematic of the LAPD. In order to visualize the interior, a cut along the axis has been made in the render. The purple and yellow bands represent the magnetic coils that produce a steady-state magnetic field. The magnetic field is directed along the axis in the $-\hat{z}$ direction. For these experiments, a magnetic field of 600 Gauss was chosen. A cross section of the port highlighted in the yellow box is displayed in figure 3.2.

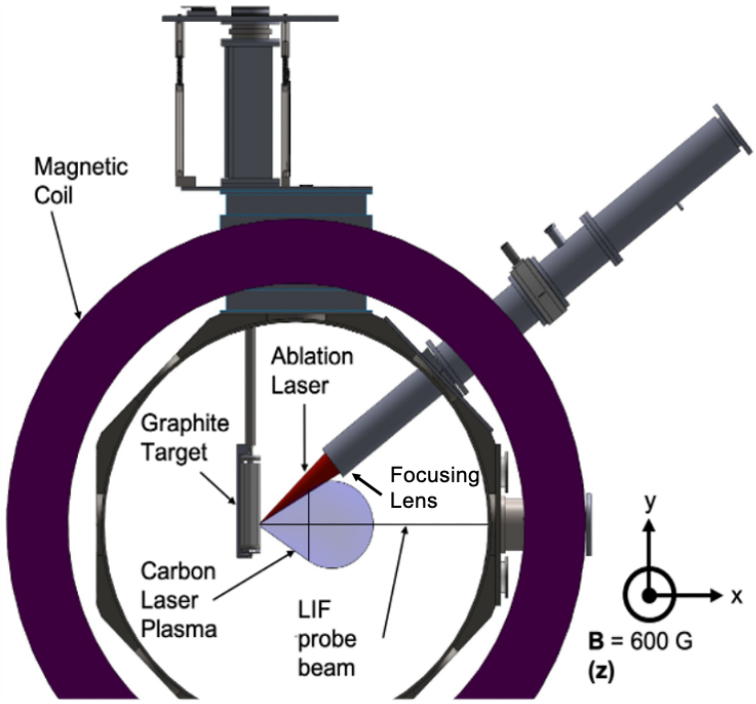


Figure 3.2: Cross section of the LAPD experiment. The ablation laser is focused onto a graphite target which creates a carbon LPP which expands quasi-perpendicularly to the magnetic field created by the purple magnet. The target is rastered in a helical pattern between shots to ensure a fresh surface for each ablation laser shot.

consistently ionized at a one quarter Hz repetition rate and any ion with a mass larger than helium would have a larger gyroradius (i.e. less magnetized). Typical ambient plasma temperatures range from $T_e = 1 - 10$ eV and $T_i \sim 1$ eV. Experimental parameters used are summarized in table 3.1.

| | | |
|---|---|---|
| $B_0$ (Gauss) | 600 | 600 |
| Plasma | $He^+$ | $He^+$ |
| L (m) | $\sim 1$ | $\sim 1$ |
| $n_i$ ($cm^{-3}$) | $1.6 \times 10^{13}$ | $2.1 \times 10^{13}$ |
| $T_e$ (eV) | 1 | $5 - 10$ |
| $T_i$ (eV) | 1 | 1 |
| $d_i$ (cm) | $\sim 10$ | $\sim 10$ |
| $v_A$ (km/s) | 170 | 140 |

Table 3.1: Important experimental parameters for the two experiments. The only substantial change to the ambient plasma was an increase in density from $1.6 \times 10^{13}$ to $2.1 \times 10^{13}$ $cm^{-3}$ which affects the Alfvén speed and therefore the Mach number

The mode of operation resulting in the highest densities in the LAPD utilize a piezoelectric gas puff near the cathode to increase the number of primary ionizing electrons. The $LaB_6$ cathode is an excellent electron emitter when heated to near electron emission temperatures ($\sim$ 1850° C) by graphite heating elements [24]. The electrons are accelerated by a relatively transparent molybdenum anode which causes $\sim$ 175 eV ionizing electrons to stream through the length of the machine. The electrons that are emitted by the cathode ionize the gas between the cathode-anode pair, which contribute to the overall number of ionizing electrons. Since the electrons are collisional with the background gas, the resulting plasma that is created has an axial gradient if the gas fill is too high. If no gas puff is used, then the number of ionizing electrons is determined by the gas fill, increasing the gas fill increases the ionizing electrons, but with the downside of decreasing the mean-free-path of electron ion collisions - too high of a density and the plasma column shortens. If gas is puffed in the region between the cathode and anode, the number of ionizing electrons is increased, while maintaining the length of the plasma column.

The experiments discussed here were performed in a quasi-perpendicular geometry, which refers to the bulk laser produced plasma flow direction ($\hat{x}$) being perpendicular to the background magnetic field ($\hat{B} = B\hat{z}$). The surface of the target where the ablation laser is focused is positioned $\sim 9 - 12$

cm from the axial center of the machine in the $-\hat{x}$ direction (as indicated in figure 3.2). The ablation laser is incident on the cylindrical graphite target at an angle of 38° with respect to the x-axis. The target was translated and rotated in a helical pattern between laser shots for one shot per position. This helps avoid cratering of the target for the subsequent shots and improves the shot-to-shot repeatability. The functionality of multiple shots on the same position was tested briefly, but found to compromise the data.

Two different ablation lasers were used in the LAPD experiments. In the first experiment, which is discussed in chapter 4, a SpectraPhysics (1064 nm, 1.5 J, 8 ns full width at half maximum - FWHM) laser system was focused to an intensity of $1 \times 10^{11}$ W/cm$^2$ resulting in a sub-Alfvénic ($M_A \sim 0.6$) bulk expansion speed. In the second experiment discussed in chapter 5, the Peening laser system (1053 nm, 14 J, 15 ns FWHM) was focused to an intensity of $1 \times 10^{12}$ W/cm$^2$. A comparison of the lasers and the ablated plasmas is shown in table 3.2. The primary ion species refers to the carbon ion with the most kinetic energy density in the LPP. This ion species will determine the coupling regime.

In both experiments the ablation beam was focused through a ⌀75 mm, f = 30 cm focal length lens that was positioned within the LAPD at the inner most edge of the lens tube holder, as depicted by the large tube inserted in the LAPD from the upper-right in the schematic of figure 3.2. While the lens holding tube has negative effects such as blocking the primary electrons which causes a shadowing of the ambient plasma to the north of the experiment, the upsides of an increased on target intensity, and blow-off velocity outweigh this.

## 3.2 Phoenix Target Chamber

In addition to experiments performed on the LAPD, a variety of smaller scale experiments were performed on a ⌀1 m, 30 cm tall cylindrical, stainless steel vacuum chamber [29]. The setup allow the creation of a very similar LPP without the ambient plasma or magnetic field and was used as a test bed for the new LIF diagnostic.

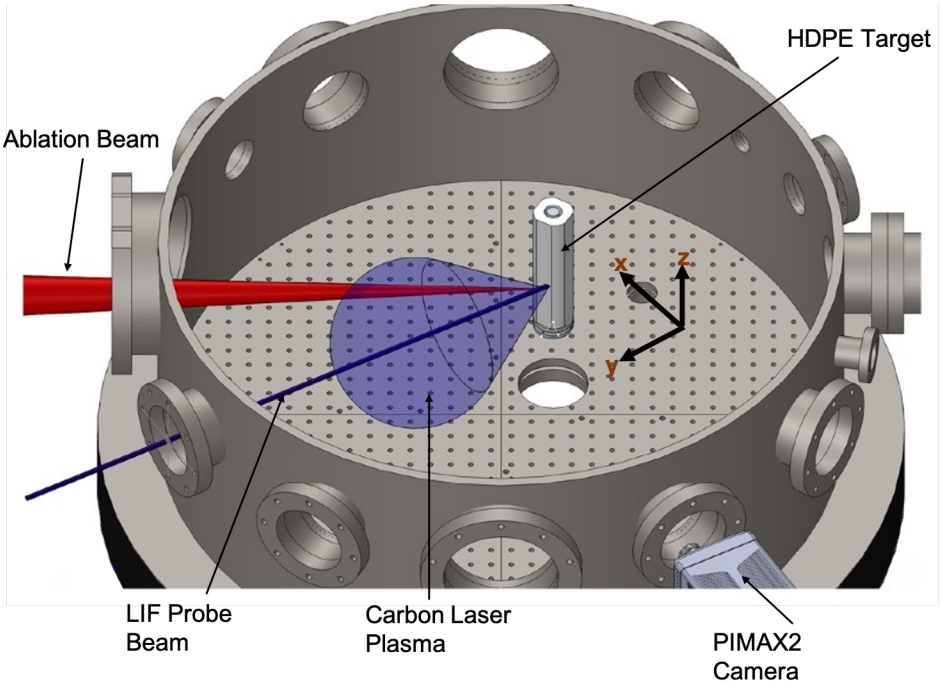


Figure 3.3: Schematic of the Phoenix laser lab target chamber where the LIF diagnostic was first tested. The ablation beam is focused onto the plastic target which creates a composite LPP of protons, carbon ion species, and a variety of molecules. The LIF probe beam is directed anti-parallel to the blow-off axis. The PIMAX2 ICCD camera images transverse to the blow-off axis.

| | Ablation Beam Parameters | |
|---|---|---|
| Laser Energy (J) | 1 | 14 |
| Intensity (W/cm$^2$) | $1 \times 10^{11}$ | $1 \times 10^{12}$ |
| Rep Rate (Hz) | 20 | 6 |
| $\tau_L$ (ns) | 8 | 14 |
| | Laser Produced Plasma | |
| $N_{particles}$ | $\sim 10^{15}$ | $\sim 10^{16}$ |
| $v_{mean}/v_A$ | 0.6 | $2-3$ |
| Primary Ion Species | $C^{4+}$ | $C^{4+}$ |
| Cavity size/$d_i$ | 0.4 | 1.1 |

Table 3.2: Comparison between the ablation beam parameters and subsequent LPP characteristics used in the two experiments. The laser energy increased by over an order of magnitude between the two experiments which created a significantly faster LPP.

The peening laser was focused by a 1 m focal length lens (with a beam $f/26$) onto the target to a $\oslash 250$ $\mu$m focal spot, at an incidence angle of 34° with respect to the $\hat{y}$ axis, as shown in figure 3.3. The different final focusing lens in this setup resulted in a slower LPP bulk speed. The target was a 2.54 cm diameter cylindrical rod made of high density polyethylene (HDPE), which was rotated in a helical pattern between laser shots to ensure a new surface. The turbo pump maintained a pressure of $2 \times 10^{-5}$ Torr by actively pumping. Actively pumping with the turbo is critical when ablating plasma on the Hz time scale as debris can build up otherwise.

Although there is a difference in target material between the two experiments, both the ablated plasma from HDPE and graphite contain large amounts of carbon ions. The HDPE targets also produce very fast protons as the LPP ions have a velocity approximately equal to the respective charge to mass ratios. The high temperatures inside the LAPD due to the radiant load of the cathode forbid the use of a HDPE target in these experiments, and graphite targets were used instead.

## 3.3 Diagnostics

Diagnostics are tools used to measure properties of the plasma of interest, whether that be in space or in the laboratory. In the LAPD these are separated into two categories of diagnostics: probes that are inserted into the plasma to physically measure a characteristic, or optical diagnostics that

characterize the plasma non-perturbatively.

The physical probes (magnetic flux probe and Langmuir probe) used in the LAPD campaigns are digitized using the LAPD's 10-bit data acquisition system (DAQ) at either 100 MHz or 1.25 GHz. Motorized drives position the probes between shots in order to analyze large regions of space. At each position $3-5$ repetitions are recorded for statistics. During a high-repetition rate run thousands of time traces are recorded relatively quickly which allows for highly resolved data to characterize the interaction.

### 3.3.1 Laser Induced Fluorescence

A novel use case of a laser induced fluorescence (LIF) diagnostic was developed for these experiments [29, 10]. LIF is a non-perturbative optical technique that is capable of selectively measuring the ion velocity distribution function (VDF) of a plasma species with high spatial and temporal resolution. It is distinct from other active optical plasma diagnostics, such as Thomson scattering and Raman scattering, in that it can measure ion properties and without *a-priori* knowledge of the distribution. LIF is a common optical technique for measuring ion VDF in basic plasmas [13, 57]. The novelty here is the use on a dense and super-Alfvénic laser produced plasma which presents unique challenges.

The ion VDF is constructed incrementally by tuning the LIF probe beam to Doppler shifted absorption wavelengths. This will resonate with electrons bound to ions of a specific velocity bin and the re-emission of light from those ions can be measured. This is performed over successive shots until the entire width of the velocity distribution has been scanned over and measured. This requires that the bandwidth of the LIF beam be much smaller than the width of the ion VDF in question, while large enough to excite a sufficient number of ions to cause a detectable signal. An illustration of this is shown in figure 3.4 where the black trace is the distribution function of a particular ion species, with the corresponding Doppler shifted spectral lines labeled on the top. The width of the LIF beam is represented by the pink block, which is the FWHM of the Gaussian

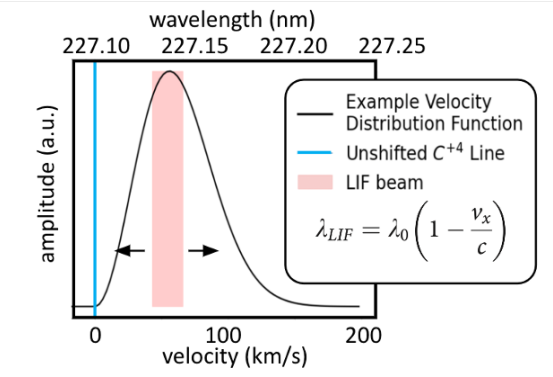


Figure 3.4: Illustration of the LIF measurement. The blue line is the spectral line chosen for LIF in a non-moving reference frame. The black line is the distribution function for the ion species to be probed by the LIF beam, with the corresponding Doppler shifted absorption wavelengths listed on the top. The pink block represents the LIF beam FWHM that is tuned, or shifted, to lower or higher wavelengths in 0.01 nm steps. The LIF beam is wide enough that a sufficient population of ions fluoresce above the noise threshold.

bandwidth of the beam. The LPP measured here is quite hot. The typical dye lasers that are used in LIF measurements have too narrow a bandwidth to measure such a wide distribution.

#### 3.3.1.1 Feasibility Study

Ideally, the plasma being diagnosed by LIF would be in a full or quasi steady-state. LIF relies upon a highly populated ground or a metastable "lower" state in the bound electrons. The laser can then excite the electrons to an "upper" state and observe the emission from the transition back to the lower state. The transient nature of LPPs present challenges to this process as the ground or metastable state are only populated some time after the creation of the LPP. Understanding these populations requires extensive modeling by collisional-radiative modeling.

Excitation out of the ground state is preferable since it is often the most populated state and fluorescence tends to be limited by the upper state enhancement. For the carbon ions ($C^{4+}$) studied in this experiment, the necessary wavelength to excite an electron out of the ground state is outside the range of commercial lasers ($\lambda_0 \approx 4 - 8$ nm). Similar to many other He-like ions, there exists a metastable state ($1s2s(^3S_1)$) for the bound electrons to populate in the $C^{4+}$ ion. Excitation out of a metastable state is feasible for LIF, although with a reduced signal gain due to the limited initial

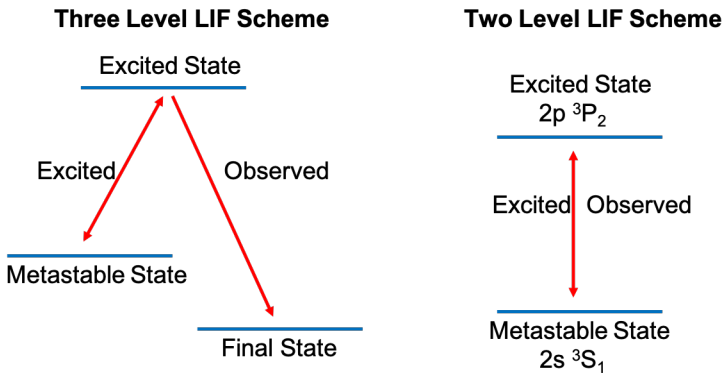


Figure 3.5: Comparison between a two- and three-level LIF scheme. The three-level LIF scheme utilizes different wavelengths for excitation and observation, whereas the two-level scheme utilizes the same wavelength for both. The $C^{4+}$ ion used in this experiment is only susceptible to a two-level scheme.

population.

When considering a LIF scheme, the ion species lends itself to either a two- or three-level scheme as depicted in figure 3.5. In the two level scheme the electron transition that is excited is the same one that is observed. The advantage is that all of the fluorescing ions decay via the same transition, but it can often present difficulties in terms of scattered light from optics and surrounding metals. In the three level scheme the excited electron can then decay via two separate transitions, with the transition to a new state being observed. This offers the advantage of not having to subtract out the scattered light from the LIF probe beam, but without the knowledge of the exact number of electrons in the transition. The $C^{4+}$ ions involved in these experiments are only susceptible to a two-level scheme.

The transition $1s2s(^3S_1) \rightarrow 1s2p(^3P_2)$ is used for both the absorption and observation of the $C^{4+}$ ions. Excitation to the $1s2p(^3P_{0,1})$ states has also been proposed; however, only the transition to and fluorescence from the $1s2p(^3P_2)$ state is considered due to its highest statistical weight.

LIF on an LPP is challenging due to the fact that a large portion of the bound electrons are from recombination, and cascade down to the lower bound states. Based on the criterion that the lower state in a LIF scheme must be highly populated compared to the upper state, a lower bound in time

is set by how quickly the electrons recombine and decay to the metastable state. Directly after the ablation laser irradiates the surface, the plasma formed is nearly fully ionized ($\bar{Z} \sim 6$). As the LPP is highly collisional at early times, this allows for electron recombination with the ions up until the density drops past the LTE condition where the temperature at that time determines the steady-state average charge of the plasma. Since bound electrons are predominantly the result of electron recapture, the electrons cascade into the metastable state. To understand the complex nature of the LPP, the radiation-hydrodynamics code HELIOS [56] is utilized to model the spatially and temporally dependent temperature and densities of the carbon plasma ablated from the target. This simulation only calculates the temperatures and densities of the plasma.

In order to obtain atomic state distributions, the simulated temperature and density profiles of the LPP are fed into a collisional-radiative modeling software (PrismSPECT). PrismSPECT then calculates the atomic state distribution, including the time-dependent bound electrons states of the various ion charge states, by solving detailed rate equations including all population and de-population mechanisms [10]. From these simulations we can evaluate when the upper state population far exceeds the lower state population as is the condition for LIF. This is depicted in figure 3.6, where a comparison of the electrons in the upper state (blue) to the metastable state (red) is shown. This suggests that a threshold for a detectable LIF signal should be crossed by $\sim$ 100 ns after the ablation laser fires. Up until saturation, the LIF signal is the brightest where the density is highest. Therefore, an upper bound in time is set by the geometric expansion leading to the dispersion of the LPP density, which for this plasma is before $\sim$ 1000 ns.

The presence of the ambient plasma leads to additional complications that must be considered. Collisional excitation from the metastable state to the upper state has a mean free path of $\lambda_{mfp} \sim 30$ cm, which is calculated from experimental findings of collisional cross sections evaluated by Phaneuf et al. [69]. As the experiment size is roughly 10 cm, this means that collisional excitation cannot be ignored.

PrismSPECT accounts for both collisional excitation from the metastable state to the upper state, as

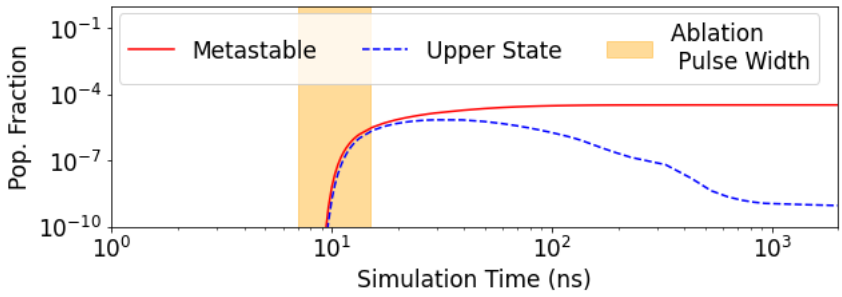


Figure 3.6: Population fraction data extracted from PrismSPECT simulation. Density and temperatures of the LPP are input into the collisional-radiative model which then exports the relative fraction of carbon ion states in the plasma. This determines the time at which we use LIF on the LPP as a high ratio between the metastable and upper state is required for LIF to be successful. This condition is met by ~ 100 ns after the ablation laser pulse.

well as well as collisional depopulation of the forbidden transition from the metastable state to the ground state. Neither of these mechanisms have a great effect on the measurement. The collisional excitation from metastable to upper state exists in both the "signal" and "background" shots and is equally subtracted out from the measurement. The depopulation mechanism does not have a great effect on the metastable state, as shown by the plateau of the red line in figure 3.6.

#### 3.3.1.2 Image Processing

In standard LIF imaging, the laser probes a region of plasma causing fluorescence from the irradiated region. The fluorescence is collected perpendicularly to the probe beam, either by an imaging system or other detector. The collection optics setup here utilize an intensified charge-coupled device (ICCD) camera optimized for low level light detection in the UV (figure 3.3). ICCD cameras couple an intensifier with an electron multiplying component in front of the CCD sensor. A narrow (~ 10 nm) bandpass filter optimized for this spectral emission line is placed in front of the camera to reject unwanted light.

Despite the bandpass filter, light from other sources (e.g. continuum light, $C^{2+}$ emission) can pass through the filter and obstruct the measurement. These light sources in addition to light from $C^{4+}$ ions not in resonance with the LIF beam must be subtracted so that the intensification of the fluorescing ions, or signal is isolated. The light sources that are not from the fluorescing $C^{4+}$ ions

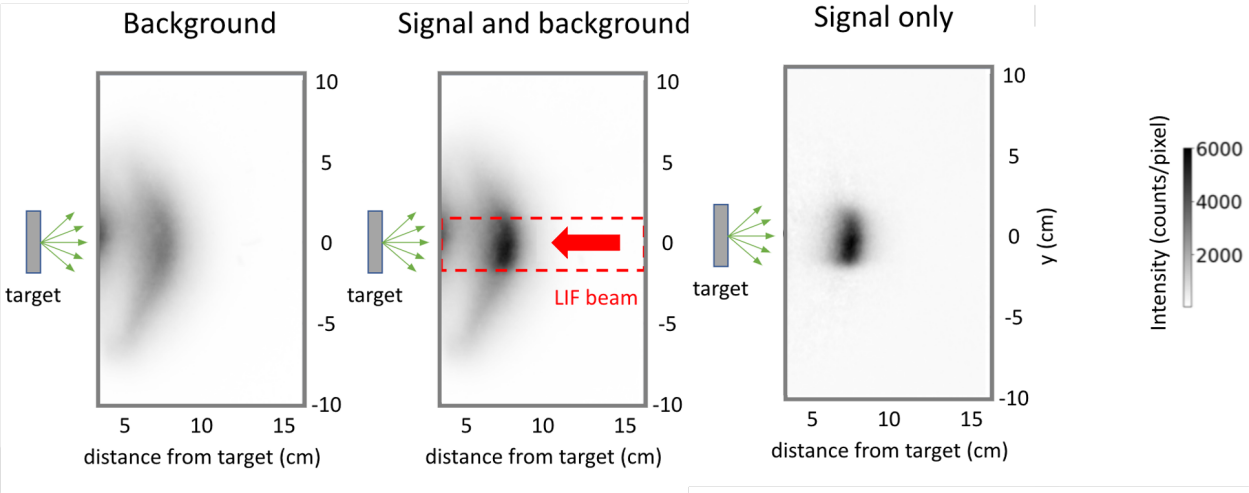


Figure 3.7: An example of the image processing necessary to extract the LIF data. The left most image shows the "background" of the measurement, which is LPP ion emission from all sources within the bandwidth of the bandpass filter. This two dominant sources are light from the $C^{4+}$ and $C^{2+}$ ions. Note that this is line integrated along the line-of-sight when imaging the region. The middle image is the detected signal when probing the LPP with the LIF beam tuned into a specific Doppler-shifted absorption wavelength. Only the region where the LIF beam passes through the LPP is fluorescing. The LIF beam is approximately a 2D sheet (negligibly thin along the line-of-sight) so this measurement offers quite good spatial resolution compared to the standard imaging. The third panel shows the subtraction of the first panel from the second panel which is done to isolate the ions that are traveling at a specific velocity.

are referred to as "background" light. In order to account for any long-term experimental changes, background and signal shots were taken in succession in sets of $40 - 100$ shots, as dictated by the signal-to-noise ratio (SNR). A fast mechanical shutter was used to block the LIF beam every other shot. These were then separated into two groups: 1) signal with background and 2) background. Each are averaged and then the background is subtracted from the signal and background in order to give the average signal. The effects of the background subtraction is shown in Fig. 3.7.

It is important to note that the LIF signal (which only consists of fluorescing $C^{4+}$ ions) has comparatively higher spatial resolution than the background emission, which consists of self-emission from other laser plasma species. The background consists of light from the plane at the lens best focus, as well as defocused light collected along the entire $\approx 10 - 20$ cm long column of the laser plasma plume (depending on how far the LPP has expanded).

Images produced by the ICCD cover a spatial area of $23 \times 23$ cm$^2$ in the plane of best focus. The

observed region of interest is a limited sample in the center of the image so as to avoid any vignetting effects of the collection optics. The exposure time varied from 2 ns for the lifetime measurements to 20 ns for all other shots. Different ICCD cameras were used in the two experiments so more details about each imaging system is given at the beginning of each experimental chapter.

#### 3.3.1.3 Image Sequences

The first image processing stage yields 2D images of fluorescing $C^{4+}$ ions at one set of time and velocity. Example images from the time scans are shown in Fig. 3.8. Panels 3.8 (a) and (b) display fluorescing ions moving at 223 km/s at 150 and 250 ns, respectively. These show that the LIF diagnostic is consistent with a ballistic model [29] for LPP expansion and offers the advantage of not requiring any *a priori* knowledge of the distribution to measure the velocity.

Each sequence of shots (i.e. wavelength scan at a constant time or time scan at a constant wavelength) is combined into a streak plot in order to represent the evolving ion dynamics in the system. For this purpose, the signal is averaged across the z-axis to reduce each image to a 1D array and stack the arrays along the scanned parameter. For the velocity scans the data is reduced down to the phase space velocity plot and for the time scans streak plots of the spatio-temporal evolution of a single velocity bin are obtained. Example of these are shown in chapter 4 detailing the sub-Alfvénic experiment.

Scattered light (the bright circle seen in Fig. 3.8 (a) and (b)) of the LIF probe beam from the target surface affects the measurement only in regions within $\approx$ 2 cm of the target surface. This prevents certain velocity bins at early time from being accurately measured.

#### 3.3.1.4 Saturation and Non-Saturation Regimes

At low probe laser powers, the fluorescence signal is linearly related to the laser power, and therefore the concentration of the absorbing species is obtained [1]. As laser power is increased, upper level entrancement is eventually limited. This regime is referred to as the saturation limit. Due to

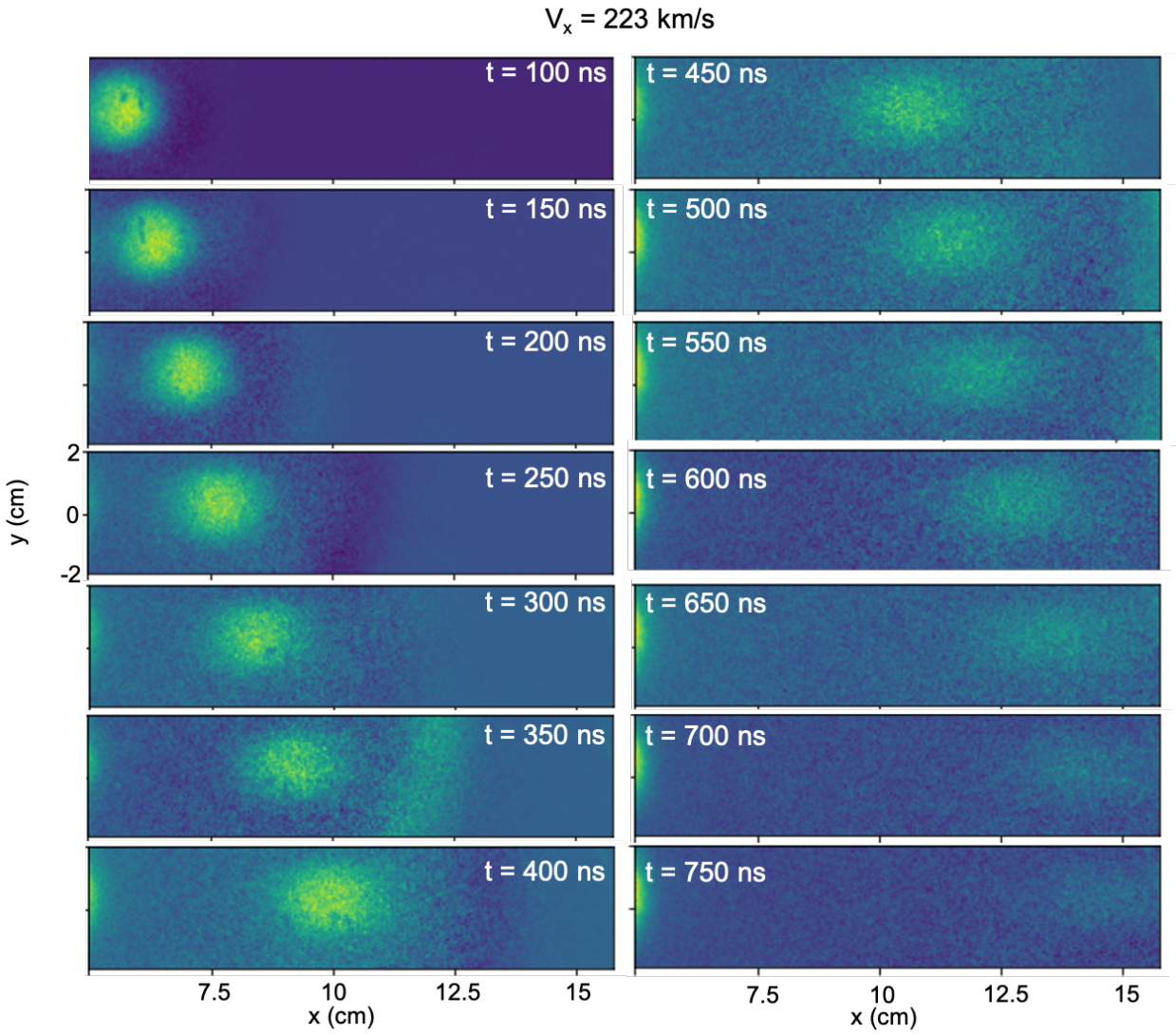


Figure 3.8: Images of $C^{4+}$ ions traveling at 223 km/s at fourteen times from t = $[100, 750]$ in 50 ns steps relative to the firing of the ablation beam. These images represent 50 total ablation laser shots, 25 in which have the LIF beam present ("signal" shots) and 25 in which the beam is not present ("background" shots). We subtract the average of the 25 background shots from the signal shots to distill the fluorescing $C^{4+}$ ions. As would be expected, the ions are further from the target at a later time.

experimental conditions, it is often necessary to work at or near the saturation limit to maximize the signal to noise ratio. Further insight is gained through the rate equations that govern this two-level system

$$\frac{dN_1}{dt} = -N_1(t)B_{12}I_\nu + N_2(t)(A_{21} + Q_{21} + B_{21}I_\nu) \tag{3.1}$$

$$\frac{dN_2}{dt} = N_1(t)B_{12}I_\nu - N_2(t)(A_{21} + Q_{21} + B_{21}I_\nu) \tag{3.2}$$

where $N_1$ and $N_2$ represent the population of the two electron levels, $B_{12}$ and $B_{21}$ are the rates of absorption and stimulated emission, $A_{21}$ is the rate of spontaneous emission, $Q_{21}$ is the metastable state quenching rate, and $I_\nu$ is the spectral energy density of the LIF probe beam.

Assuming that $I_\nu$ varies slowly in time so that the steady-state condition applies ($dN_{tot}/dt = 0$, where $N_{tot} = N_1 + N_2$) it is shown that

$$N_2 = \frac{B_{12}I_\nu}{A_{21} + Q_{21} + B_{21}I_\nu}N_1. \tag{3.3}$$

In the saturation limit ($B_{12}I_\nu >> c(A_{21} + Q_{21})$) the fluorescence is no longer proportional to the laser irradiance and the dominant de-population method is stimulated emission. It has been suggested that in the saturation regime the concentration is extracted by plotting fluorescence power against inverse laser power, but requires a high intensity probe laser [8].

In order to establish where on the saturation curve the LIF measurement lies, we compare the LIF measurement with a series of subsequent measurements where we attenuate the LIF probe beam by sending it through a UV neutral density (ND) filter of a certain optical density (OD). If we are operating in the saturation regime, then we would expect to see no decrease in fluorescence when we attenuate the LIF beam. If we do see a decrease then we know that we are operating in the

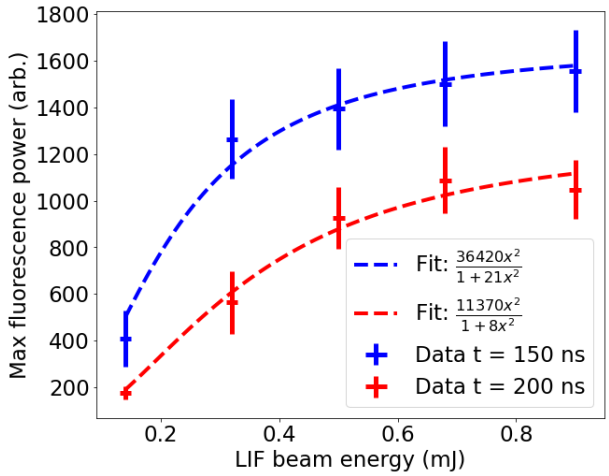


Figure 3.9: Maximum value of the attenuation scan. This measurement at 150 ns is quite near the saturation region as the max fluorescence power is beginning to level off, as is indicative of the saturation region. The LPP state at 200 ns is further away from saturation given the probe beam energy.

non-saturation regime.

As the LPP density and population fractions are highly time-dependent, we must establish the saturation curve for each given time. For two times the results of a LIF beam energy sweep is shown in figure 3.9. This LIF beam energy is swept by attenuating the beam with the UV ND filters. The data set taken at t = 150 ns (blue) displays more of the saturation regime than the data set at 200 ns (red). This is evident in the flattening of the blue curve compared to the red curve. With proper calibration we would be able to obtain the density of the LPP with a more comprehensive scan.

The data acquired here utilized the probe beam in its natural circular cross section. In the experiments on the LAPD the LIF beam is fanned out and therefore the fluence is lowered, pushing the measurement outside of the saturation regime. This has the cost of reducing the overall signal-to-noise ratio, but has the benefit of not having to take into account saturation broadening of the spectra [40, 19].

### 3.3.2 Magnetic Flux Probes ("bdots")

Time evolving magnetic fields are measured with a magnetic flux probe, also known as a "bdot" (dB/dt = $\dot{B}$) [33]. These probes are comprised of wires wrapped around a ceramic cube, with each set of coils oriented along a different Cartesian coordinate. When the magnetic field changes, a voltage is induced in the coil perpendicular to the change in B and is proportional to the effective area of the coil ($V_{induced} \propto A_{eff}\dot{B}$). The signal is attenuated and amplified in the coil which is then recorded on the LAPD DAQ system.

The attenuation and amplification processes seem redundant, but serve separate and important roles. Differential amplifiers subtract off any DC signal induced in the coils. There are multiple factors that can cause an offset to the signal, but the primary component is due to electrostatic potentials in the plasma. The attenuation must be applied before the differential amplifiers since the maximum allowable voltage is ±1 V. These measurements are numerically integrated to give $\Delta\mathbf{B}$. The frequency response is reasonably estimated by an RL circuit formed by the internal inductance (L) and resistance (R) of the coil (negligible capacitance is assumed)

$$\frac{1}{f} = \tau_{LR} = \frac{L + M}{R} \tag{3.4}$$

where L is the self inductance of the coil, M is the mutual inductance of the wound pair, and R is the resistance of the coil itself.

With the recent upgrades to the LAPD, the radiant heat load of the $LaB_6$ cathode has increased drastically. The bdot design had to be adjusted to withstand this increased heat load, which increased the difficulty of assembly. In the original design, the wires were wound around a Vespel core and run a relatively short distance to the circuit board. The Vespel core had to be replaced by a ceramic core, all epoxy was replaced by high-temperature epoxy, and the circuit board that previously existed near the core had to be placed further along the shaft. This increased the length of wire that could potentially pick up undesirable signals and affect the measurement. The top end

frequency range (> 10 MHz) was affected more than lower frequency ranges and so this is ignored for the measurement presented here.

In these experiments a $3 \times 3 \times 3$ mm$^3$, 10 turn bdot was provided by the LAPD facility for use. The spatial resolution is limited to the size of the bdot (3 mm), and the temporal resolution is essentially limited by the number of turns (~ 10 MHz), which changes the self-inductance (see equation 3.4). As discussed previously, the environment created by the LPP is quite extreme in both spatial and temporal scales - even compared to the LAPD background. Ideally, a bdot that was smaller and with fewer turns would be fielded in these experiments in order to increase the spatial and temporal resolution of the measurements.

### 3.3.3 Density Measurement

Accurately measuring the ambient density defines which regime the experiment is in (sub- or super-Alfvénic) by determining the Alfvén speed. Prior to the upgrade of the LAPD that resulted in an increased ambient density, density scans were performed by a Langmuir probe and calibrated by a microwave interferometer. However, the upgrade pushed the density near the bounds of the critical density for 60 GHz microwave interferometers which brings into question the validity of the standard calibration method. Additionally, the lens tube that holds the final focusing lens inside of the LAPD (as seen in fig. 3.2) shadows the plasma along the path of the interferometer which makes the measurement invalid.

In order to validate the interferometer, another method of density calibration was devised in which an Alfvén wave was launched by an antenna at a known location and measured by a bdot down field. Through a time-of-flight measurement of $v_A$, an average density could be deduced and used for calibration.

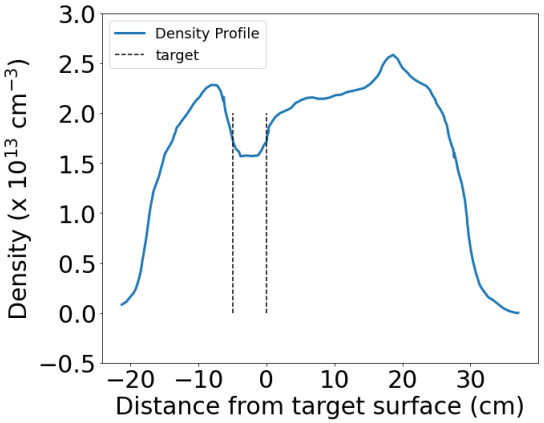


Figure 3.10: Lineout of the LAPD density profile from a Langmuir probe scan along the x-axis at y = 0. The x-axis has been shifted according to the offset of the graphite target relative to the LAPD coordinates. The absolute values of the density are calibrated with an Alfvén wave measurement. The black doted lines represent where in the plasma the graphite target is located. This lineout was taken one port (32.5 cm) to the south (closer to the cathode) of the target, however the effects of the large obstruction can still be seen in the density profile.

#### 3.3.3.1 Langmuir Probe

A Langmuir probe consists of small electrically biased wire with a surface (A) exposed to a plasma that forms a Debye sheath [62, 18]. It was used in each of the LAPD experiments to measure the electron temperature and density of the ambient plasma with spatial resolution. Two modes of operation are common use for the Langmuir probes: one in which the voltage is swept while the plasma conditions remain unchanged, and one in which the bias is fixed while the plasma conditions evolve. For these experiments only the fixed bias type was used, which is referred to as $I_{sat}$, short for ion saturation. The time scale for measuring this is limited by the Debye sheath formation time, which is easily satisfied with the given conditions.

$$I_{sat} = \begin{cases} \frac{1}{4} e n_i A \sqrt{\frac{8T_i}{\pi m_i}}, & \text{if } T_i \sim T_e \\ 0.6 e n_i A \sqrt{\frac{T_e}{m_i}}, & T_e \gg T_i \end{cases} \tag{3.5}$$

From equation 3.5, correctly measuring the area of the probe tip determines the accuracy of the density measurement. When exposed to the harsh environments of the LAPD, the surface area can deform over time from debris being deposited onto the surface. Not only does this increase

the area of the probe, but it also affects the conductivity of the surface which changes the Debye sphere. As a result, the Langmuir probe is not the best tool for measuring an absolute value of the density. It has the advantage of providing spatially resolved measurements. When used in conjunction with an integrated value of density, Langmuir probes can reveal 1D or 2D profiles of density or temperature.

#### 3.3.3.2 Microwave Interferometer

Several 60 GHz microwave interferometers are installed throughout the LAPD to measure the line-integrated density [48]. As the microwave passes trough the plasma, the phase is shifted proportionally to the average electron density. The coherence of the transmitted wave with the unaltered microwave signal is used to determine the absolute phase shift. Once the line integrated density has been measured, the absolute density profile can be distilled by comparing this to the shape of the plasma measured by the Langmuir probes. The line integrated density is found from

$$\int n_e dl = \frac{-2cn_c\Delta\phi}{\omega_{probe}} \tag{3.6}$$

where $\Delta\phi$ is the total phase shift, $\omega_{probe}$ is the microwave frequency, and $n_c$ is the critical density where the plasma becomes opaque to the interferometer

$$n_c = \frac{\epsilon_0 m_e}{e^2}\omega^2 \approx 1.24\times10^{-8} f cm^{-3} \tag{3.7}$$

where f is the frequency given in Hz. The critical density for refraction of the 60 GHz interferometer is $n_c \sim 4\times10^{13}$ cm$^{-3}$ which is close to the operating density. Despite the theoretical limit for use of 60 GHz interferometers of $4\times10^{13}$ cm$^{-3}$ which is much higher than the $\sim 2\times10^{13}$ cm$^{-3}$ densities in the experiments, the actual limit for accurate detection fails before this limit.

One complication of using the interferometer in the LAPD setup is the direction of travel. The

microwaves are launched from the top 45° east flange and measured on the bottom 45° west flange. This path is directly shadowed by the lens tube, which gives an underestimate of the line integrated density for the plasma that is not in the shadow. Therefore, an additional method was developed by Vincena and Gekelman to check the validity of the density estimated in this way.

#### 3.3.3.3 Alfvén Wave

The Alfvén speed depends on the density of the medium it travels through ($v_A = B_0/\sqrt{4\pi n_i m_i}$) [36]. With the reasonable assumption that the plasma is evenly magnetized and contains only a single ion species ($He^+$), the average density is calculated by launching an Alfvén wave with a rotating magnetic field antenna along the axis of LAPD and measure the dispersion of the wave.

An antenna on the far north end of the device creates an Alfvén wave that is measured a known distance (generally 4 m) from the launch point. Measuring the Alfvén wave at adjacent ports allows the change in time and phase of the waves to be recorded. The time-of-flight reveals what the Alfvén speed is, which can in turn validate the average density along the axis of the LAPD. The phase change allows us to calculate the dispersion relation to determine the density.

This method was devised by Dr. Gekelman and implement by Dr. Vincena and worked well for calibrating the Langmuir probe in the second set of experiments where the density of the plasma was too high for the interferometer. This method is more reliable than the interferometers currently installed on the LAPD and should be used for future Langmuir probe calibrations. The density plot shown in figure 3.10 used the calibration method described here.

# CHAPTER 4

# Sub-Alfvénic Coupling

This chapter reports the spatially and temporally resolved velocity distribution function (VDF)[1] measurements of a carbon LPP to better understand the collective electromagnetic behavior that couples and transfers energy to an ambient magnetized helium plasma through a novel application of laser induced fluorescence (LIF) [29]. The LAPD at UCLA provides a unique platform for studying the sub-Alfvénic ($M_A \approx 0.6$), quasi-perpendicular expansion of a carbon (C) LPP cloud into a magnetized ambient plasma. As the laser plasma expands primarily perpendicularly to the background magnetic field, a charge-separation induced electron diamagnetic current expels the magnetic field in the wake of the high-density LPP ions [77]. The spatial structure in the magnetic fields, as well as the interaction of the trailing, higher density ions with the magnetic fields sets up a laminar electric field that accelerates the ambient ions [9, 13, 75]. Regions in phase-space where LPP ions with a wide distribution in velocity are piled up where the diamagnetic currents are highest. This signifies the coupling of the leading edge, high density LPP ions to the background is dominated via laminar interactions.

To better understand the dynamics of both the background and LPP, the measured LPP ion VDF and magnetic field traces are compared with particle-in-cell (PIC) simulations. PIC codes are computational tools used to simulate plasma behavior by representing particles on a grid and solving for electromagnetic fields using Maxwell's equations. Particles' motion is calculated based on the Lorentz force equation, and their interactions with fields are used to update the grid-based

[1] The full velocity distribution function was only measured at two times.

electromagnetic fields. These simulations capture collective plasma effects and require careful time integration and boundary conditions, often employing parallel computing for efficiency and enabling the study of diverse plasma phenomena.

PIC simulations have been used to model the very large scale (> km) interactions such as high altitude nuclear experiments [32, 54] and steady-state magnetospheric shocks [91] as well as the smaller scale (< cm) lab-astrophysics environments [89, 76] in great detail. It has become commonplace to use computer simulations to interpret experimental data as well as to bridge the gap between laboratory data and *in situ* spacecraft measurements. In matching observables from experimental data (time resolved LPP ion VDF and magnetic field traces) to PIC simulations with good agreement, the simulations allow for a more complete understanding of the dynamics of the LPP ions and the transfer of energy to the background particles.

This chapter is structured as follows. Section 4.1 describes the experimental setup and diagnostics. The experimental findings are presented and their comparison with PIC simulation models to understand the coupling of a sub-Alfvénic LPP to a background magnetized plasma in Sec. 4.2 and Sec. 4.3. Section 4.4 is a summarizes our main results.

## 4.1 Experimental Setup

The experimental setup is illustrated in Fig. 4.1 (a). The LPP cloud is created by focusing a high intensity laser beam (1064 nm, 1.5 J, 8 ns FWHM) onto a graphite (C) target. For a given target material, the intensity of the ablation laser determines the composition of the plasma it creates. Focusing the laser to a higher intensity results in faster, higher charge-state ions, with the trade-off of fewer overall ions [39, 77]. An intensity of around $1 \times 10^{11}$ W/cm$^2$ was achieved, resulting in an LPP cloud with kinetic energy density dominated largely by the $C^{4+}$ ions.

Higher charge state (i.e. $C^{5+}$ and $C^{6+}$) that are faster than $C^{4+}$ are also present, but have orders of magnitude less density. These fast ions leak out of any magnetic field deformations and do not

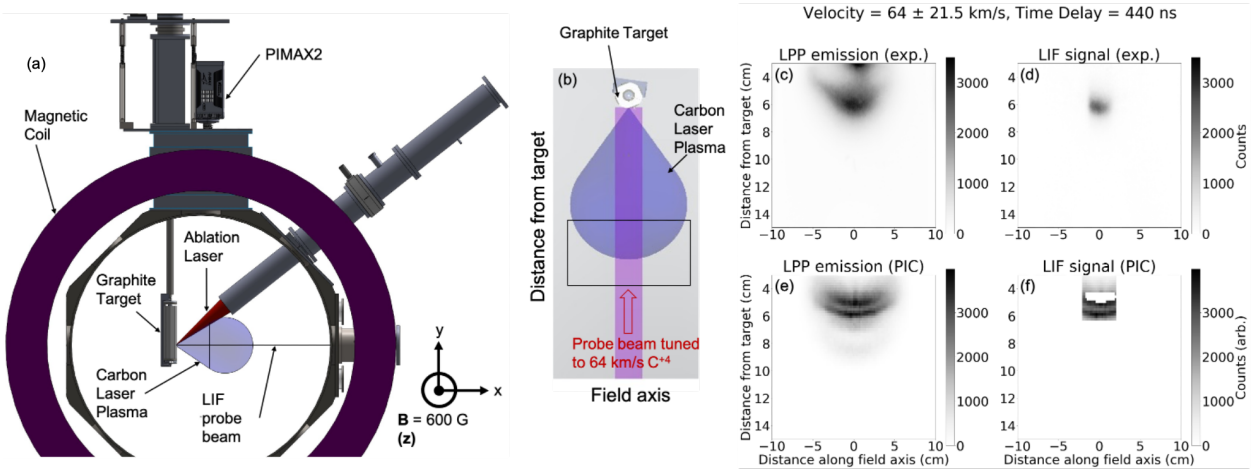


Figure 4.1: (a) Schematic of the experiment. The graphite target is located at x = −12 cm (origin is the axial center). The LIF probe beam is directed anti-parallel to the x-axis (blow-off axis). The PIMAX2 camera images along the y direction. The LIF probe beam is expanded along the z-axis (co-ordinates as indicated in the bottom-right of panel (a)). (b) Illustration of the imaged region of the laser plasma during the expansion (as indicated by the black rectangle). Panels (c) and (e) show a comparison between experimental and simulated emission from the entire LPP cloud, including all $C^{4+}$ self-emission lines as well as other species at 440 ns after laser ablation. Panels (d) and (f) show background-subtracted fluorescence maps for $C^{4+}$ ions moving at 64 km/s (speed dictated by LIF beam wavelength). The simulated data (f) has been cut abruptly at the edge of the beam width (±2.5 cm in z).

interact substantially. The lower charge states (i.e. $C^{+}$, $C^{2+}$ and $C^{3+}$) are much slower despite their relative abundance. They have been observed to travel well behind the diamagnetic cavity edge [49], where the primary coupling occurs. The second dominant ion species in terms of kinetic energy density is the $C^{2+}$ ion, which is counter intuitive since the relative abundance would be expected to be proportional to the charge. While this phenomena is not completely understood, an interpretation can be inferred from recapture rates in the interaction of $C^{4+}$ with neutral He. At lower energies (< 1 keV/amu), double electron capture ($C^{4+}$ + He → $C^{2+}$ + $He^{2+}$) has a larger cross section than single electron capture ($C^{2+}$ + He → $C^{+}$ + $He^{+}$). From this it is postulated that the recapture of free electrons might also preferentially choose to recombine to $C^{2+}$ over $C^{4+}$.

The experiment was performed in a quasi-perpendicular geometry, which refers to the bulk laser-plasma flow direction (x) being perpendicular to the background magnetic field ($\mathbf{B} = B\hat{z}$). The surface of the target where the ablation laser is focused is positioned ∼ 12 cm from the axial center of the machine in the -x direction (as indicated in figure 4.1 (a)). The ablation laser is incident on

the cylindrical graphite target at an angle of 52° with respect to the y-axis. The target was translated and rotated in a helical pattern between laser shots for one shot per position. This helps avoid cratering of the target for the subsequent shots and improves the shot-to-shot repeatability.

The LPP expands into a magnetized pre-formed helium plasma in the LAPD. For this experiment the plasma density was measured to be $n_i \approx 1.6 \times 10^{13}$ cm$^{-3}$.

After the LPP expands for a specific time, the LIF beam is directed anti-parallel to the expansion, intersecting along the 'blow-off axis' (Fig. 4.1 (b)) and interacts with the $C^{4+}$ ions. The LIF beam is generated by a tunable, diode pumped solid state laser (Ekspla NT230). In this experiment, the beam is tuned around 227.091 nm (1.5 mJ, 4 ns pulse duration, 50 Hz, 6.5 cm$^{-1}$ bandwidth). Using cylindrical lenses, the beam is expanded from 4 mm to 5 cm in the z direction, while the height of the beam remains ≈ 4 mm in the y direction. The beam is then transmitted through a quartz vacuum window and terminates on the graphite target as depicted in Fig. 4.1 (b). The intensity of the LIF beam is too low to ablate the target.

The camera-based detection system used to image the fluorescence consisted of an image-intensified charge-couple device (ICCD) camera with an intensifier sensitive in the ultraviolet (UV) range, an objective (25 mm fixed focal length, f/2.8 – f/16, UV sensitive), and a relatively broad (10 nm FWHM, 228 nm central wavelength) optical filter. The optical filter is placed directly in front of the objective to reject stray light from the ablation laser and many spontaneous emission lines. The camera images the plasma perpendicularly to the probe sheet - along the y direction from the top as shown in Fig. 4.1 (a). Note that a spontaneous emission line of $C^{+2}$ (229.687 nm) is transmitted through the filter; however, this line is not in resonance with the LIF beam and is subtracted from the signal. An example of the background and signal is displayed in Fig. 4.1 (c) and (d) and an equivalent representation from a PIC simulation (discussed later).

Given the orientation of the LIF beam relative to the LPP expansion, the component of velocity along the blow-off axis (x-axis) was measured by tuning the wavelength of the LIF beam according

to

$$\lambda_{LIF} = \lambda_0(1 - \frac{v_x}{c}) \tag{4.1}$$

where $\lambda_{LIF}$ is the wavelength of the probe beam, $\lambda_0$ is the non-Doppler shifted absorption wavelength, $v_x$ is the velocity of $C^{4+}$ ions along the blow-off axis, and $c$ is the speed of light. In the reference frame of the LPP ions, the LIF laser is blue-shifted. Therefore, in order to measure positive velocities along the blow-off axis the LIF probe beam must be red-shifted.

The LIF beam has a bandwidth of 6.5 $cm^{-1}$ (0.033 nm at 227.091 nm), which corresponds to velocity bins of $\approx$ 43 km/s. However, the wavelength of the LIF laser is tuned with 0.01 nm ($\approx$ 13 km/s at 227.091 nm) resolution. This allows us to measure a more resolved VDF profile by stepping through the velocity profile in 13 km/s steps.

The LIF beam cross section determines the spatial resolution of the measurement. The spread in the probe beam illuminated 5 cm along the z-axis and 4 mm along the y-axis. The fluorescing $C^{4+}$ ions (signal) has a high spatial resolution compared to the background, which consists of both the LAPD He plasma emission, as well as emission from other laser plasma species. The background emission consists of light from the plane at the laser beam's best focus, as well as defocused light collected along the entire $\approx$ 80 cm of LAPD plasma column, and the $10 - 20$ cm long column of the laser plasma plume (Fig. 4.1 (a)).

A bdot probe [33] was inserted into the plasma in the same xz-plane as the LIF beam, during separate shots. In addition to measuring the magnetic field flux, the probe is used to calibrate the pixel/distance ratio of the LIF detection system. All other parameters were held constant so as to have a one-to-one comparison to the LIF data. The probe directly measures the diamagnetic cavity as well as plasma waves produced by the LPP. The bdot was used to record magnetic signal traces in an xz plane. Boundaries of this plane were constrained by the target surface in the x-direction

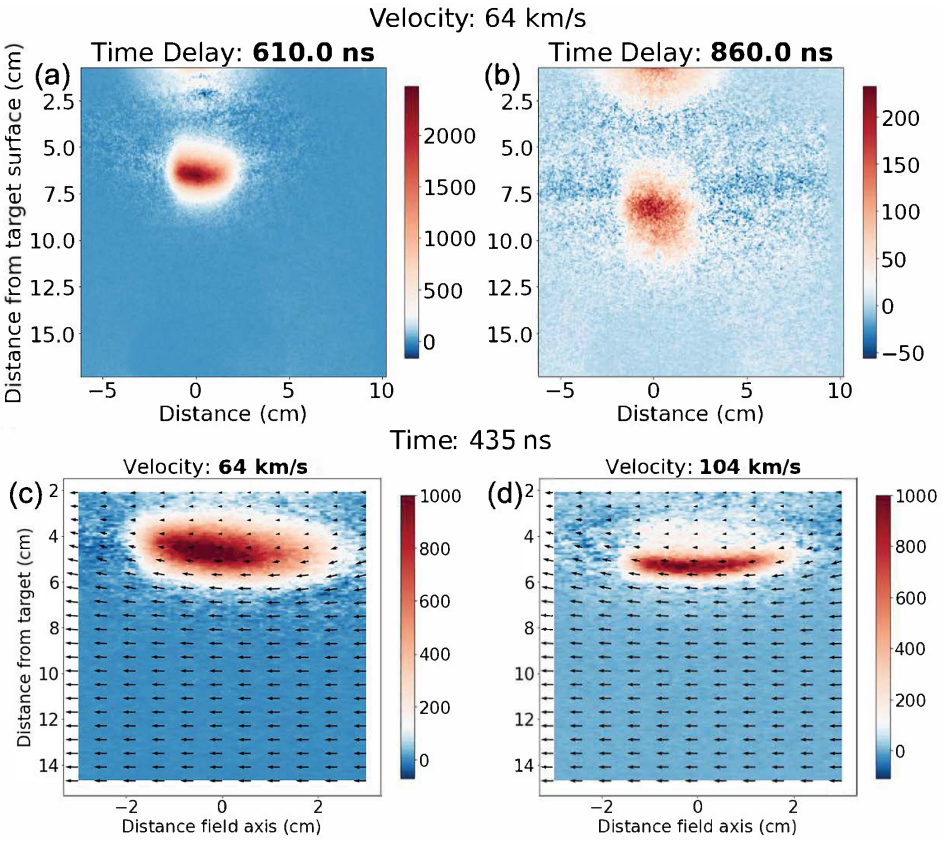


Figure 4.2: Images of fluorescing $C^{4+}$ ions at a several velocities and times. Each images represents 25 signal shots with 25 background shots subtracted to highlight the fluorescing ions. (a) and (b) show the same velocity bins at two different times which is consistent with a time-of-flight model where faster ions are further from the point of inception than slower ions. (c) and (d) show the same time at two different velocity bins. Ions in the 64 km/s bin have slight overlap with the ions in the 104 m/s bin which seems to violate the time-of-flight model. This can be explained by the coupling to the ambient magnetic fields as will be detailed in section 4.3.1. The black arrows overlayed into the bottom images represent the magnetic field measured with a bdot probe.

(-12.1 cm), and the LAPD electromagnets in the z-direction ($-3 < z < 3$ cm).

## 4.2 Particle-In-Cell Simulations

To gain insight into many of the features observed in the experimental data, a three-dimensional (3D) fully kinetic PIC simulation [54] using the VPIC code [15] was performed by Ari Le at LANL to model the experiment and explore the collisionless coupling between the sub-Alfvénic LPP and the background magnetized plasma. A 3D full PIC simulation was chosen over a hybrid model as the spatial extent of the entire experiment was not large compared to the Debye length, which must be resolved for numerical stability. There were two objectives of the simulation code: one to validate the PIC code, but also to understand the unmeasured experimental quantities such as the electric field and response of the ambient plasma.

| | Simulation | Experiment |
|---|---|---|
| $m_{He}/m_e$ | 25 | 7440 |
| $v_A/c$ | 0.1 | $5.5 \times 10^{-4}$ |
| $\beta$ | $<< 1$ | $<< 1$ |
| $v_{x,C^{+4}}/v_A$ | 0.6 | 0.6 |
| $\rho_{C^{+4}}/d_i$ | 1.9 | 1.9 |
| $v_{x,C^{+2}}/v_A$ | 0.4 | 0.4 |
| $\rho_{C^{+2}}/d_i$ | 2.5 | 2.5 |
| $L/d_i$ | 0.5 | 0.5 |
| $Z_i$ | $e$ | $e$ |
| $B_z$ (G) | 600 | 600 |
| $n_{He^+}$ ($cm^{-3}$) | $1.6 \times 10^{13}$ | $1.6 \times 10^{13}$ |
| $T_e$ (eV) | 1 | 1 |
| $T_{He^+}$ (eV) | 1 | 5 |
| $c_s$ (km/s) | 6.4 | 6.4 |
| $\lambda_{mfp,C^{+4}}(m)$ | $> 10$ | $> 10$ |

Table 4.1: Comparison between simulated and experimental background plasma conditions, where $\rho_i = v_{x,i}/\omega_{c,i}$ is the directed ion gyroradius, $d_i = c/\omega_{p,i}$ is the ion inertial length, $\beta = 8\pi nT/B^2$ is the ratio of plasma pressure to magnetic field pressure, L is the magnetic cavity size, $v_A$ is the Alfvén speed, $c_s$ is the sound speed, and $\lambda_{mfp}$ is the collisional mean free path between the two ion species.

The initial simulated background plasma conditions are compared to the experimentally known

quantities in table 4.1. The non-physical ion to electron mass ratio was varied from 25 to 100 with negligible effects and so the mass ratio was kept at 25. Simulation lengths are scaled to match $d_i$, times are scaled to match $1/\omega_{c,i}$, and velocities are scaled to match $v_A$ within the confines of the non-physical mass ratio and speed of light. The PIC simulation used a domain of $L_x \times L_y \times L_z$ = 4 $d_i$ × 2 $d_i$× 6 $d_i$ = 144 × 72 × 216 cells, with $5 \times 10^8$ macroparticles per species in the uniform background plasma, $\sim 1 \times 10^7$ $C^{4+}$ macroparticles, and $\sim 5 \times 10^7$ $C^{2+}$ macroparticles.

A cloud of ions representing the LPP ($m_{LPP}/m_{He} = 3$ corresponding to $m_{LPP}/m_e = 75$ to differentiate the LPP ions from the ambient ions) was initialized at the origin with a density profile $n_{LPP} \propto cos^4(\theta)$ and velocity profile $v_{LPP} \propto cos^2(\theta)$, where $\theta$ is the azimuthal angle with respect to the blow-off axis. Maintaining the mass ratio of LPP ions to ambient ions is important for matching their respective charge-to-mass ratios as the Larmor radii are important for the coupling. The FWHM initial spread in the LPP ion distribution is over $\sim$ 2 cm in each direction, which is done in order to make the Debye lengths a reasonable value in order to be able to resolve in the simulation. As the LPP in the experiment is considerably smaller in comparison, the starting time of the PIC simulation represents a short amount of time ($\sim 50 - 100$ ns) into the expansion of the experimental LPP into the ambient plasma. This delays the physics between the PIC simulation and experimental data by a small, amount that is challenging to quantify. Since the coupling between the two plasma ion species primarily happens after approximately 400 ns, the PIC simulation captures this physics.

The initial energy was partitioned between two populations of ions: $C^{4+}$ with a $v_{x,mean}$ = 105 km/s and $C^{2+}$ with a $v_{x,mean}$ = 65 km/s. This is chosen to be consistent with previous work where relative kinetic energy densities have been studied with respect to ablation laser intensity [77]. The $C^{4+}$ distribution was measured at many times in the experiment and thus used to match the simulation code. The $C^{2+}$ distribution was varied until good agreement in the spatial extent of the diamagnetic cavity between the experiment and PIC simulations was achieved, particularly in the region trailing the fast $C^{4+}$ ions. The electron temperature was set to $T_{e,LPP} = 10\ T_{e,background}$ within the simulation in order to match the timing of the diamagnetic cavity leading edge slope. It

was found by varying this parameter that with too small of an electron temperature in the LPP that the cavity would not extend far enough in x, but last for too long of a time. The expansion speed and size of the diamagnetic cavity is an important feature to match when simulating these experiments as the size represents the transfer of energy from the LPP to the ambient magnetic fields and ions as seen in chapter 2.

While matching simulations to experimental results it is critical to correctly initialize both the electron and ion distributions, even though the experimental diagnostics are primarily used to characterize ion properties. Many of the most important features (diamagnetic cavity formation and collapse, energy transfer, heating, etc.) arise due to the interactions between electron and ion distributions and are therefore a useful benchmark when validating that the simulations accurately portray the experiment. Many MHD codes hide the physics behind the diamagnetic cavity and field compression and therefore do not accurately match the experimental findings. It was determined that treating the electrons as two separate temperatures was critical to obtaining reasonable agreement between the experimental data and PIC simulations. A comparison between the measured and simulated evaluation of the diamagnetic cavity is displayed in Fig. 4.4 (b) and (e), respectively. The maximum cavity size (defined here as the location of highest magnetic field gradient at the time of largest cavity size) was obtained at $x = 5.7$ cm and $t = 500$ ns for the experimental data and $x = 6.1$ cm and $t = 585$ ns for the PIC simulations.

Figure 4.1 displays the similarity between the experimental ((c) and (d)) and PIC simulation ((e) and (f)) of the total LPP emission ((c) and (e)) and the LIF signal at 64 km/s ((d) and (f)). LIF data from the PIC simulation is extracted by tracking ions moving at a specific velocity bin. The similarity of the experimental and simulated LIF signal also point to the PIC simulation being representative of the experiment.

The magnetic field values are explicitly returned by the PIC simulation. There many be small differences when measuring the magnetic fields with a bdot probe due to the frequency response of the probe which could lead to smaller measured magnetic compression since the leading edge of

the compression is quite fast. The general shape and cavity size measured should be well reflected by the absolute values output by the code.

Extracting the LIF data from the PIC simulation was a bit more involved since it does not drop out so conveniently. Firstly, ions moving within a specific velocity bin had to be isolated. For instance if ions traveling at 64 km/s were going to be plotted, the ions outside of the $64 \pm 21$ km/s velocity range are dropped. Then, as the bandwidth of the LIF laser beam is Gaussian in shape, the remaining ion distribution is multiplied by a normalized Gaussian distribution weighted according to the velocity. This would result in heavier weighting of ions traveling at the center of the bandwidth ($\sim$ 64 km/s) compared to ions traveling at the FWHM ($\sim$ 43/85 km/s). This reflects the instrument function and artificially broadens the PIC outputs compared to plotting a single velocity. In order to scale the absolute values, the trimmed velocities were multiplied by the density output from the PIC simulation and by the macroparticle/experimental particle factor. Finally the relative population of the metastable state of the $C^{4+}$ which was output by the PrismSPECT [11] modeling discussed in chapter 2 was taken into account, as well as an estimated factor accounting for the efficiency of the collection optic setup (detector quantum efficiency, spectral filter transmissivity, etc.).

## 4.3 Experimental Results

### 4.3.1 Spatio-temporal Evolution Maps

To gain insight into the interaction between the LPP ions and the magnetic field, it is useful to plot spatio-temporal evolution maps of ion velocities and magnetic fields side-by-side for direct comparison. To distill the LIF images into an x vs t format, the data along the x axis from each image is stacked along the time dimension for a given velocity bin. Examples of such a streak plot are displayed in figure 4.3 (a) and (b) for velocities corresponding to $v_x$ = 64 and 104 km/s. Below the ion velocity evolution maps, the magnetic field data along the x-axis is shown in (c) and the calculated Hall or magnetic structure term ($E_x = \frac{\mathbf{J}\times\mathbf{B}}{en_e}$) from the laminar electric field equation is shown in (d). It is assumed that $E_x \sim \frac{J_y \times B_z}{en_e}$ and $J_y$ in calculated via Ampere's law in the xz plane.

For the geometry in this experiment, the current in the y direction should significantly outweigh the current in the z direction. Here we are assuming the Darwin limit in which the transient, high frequency displacement current component of the electric field can be ignored.

Fig. 4.3 (c) displays a streak plot of the magnetic field in the z-direction as measured by the bdot probe. The white regions are undisturbed from the initial 600 G background field. The red region is the leading-edge compression ahead of the fast laser produced ions, and the blue region represents the diamagnetic cavity produced by the E×B drifting electrons [63, 9, 88, 22].

Figure 4.3 (a) displays the signal from ions moving at $v_x = 64 \pm 21$ km/s vs time after ablation. At very early time (t < 300 ns) the signal is negligible, signifying that there are too few particles traveling within this velocity bin to allow their detection. At x = 5 cm and approximately 350 ns, a large signal appears, which then continues past t = 800 ns spreading out as time increases. Following a ballistic model ($\Delta x/\Delta t$), particles at 5 cm and t = 350 ns would have an average directed velocity of $v_x = 140$ km/s, substantially higher than the velocity illuminated by the LIF diagnostic. The spatial correspondence of this signal of ions traveling at a velocity slower than explained by ballistic motion with the location of large calculated electric field (d) suggests coupling mediated by this magnetic structure, or Hall term. Ions at the leading edge experience an inward facing electric field via the magnetic structure term, and therefore decelerate rapidly down to ~ 64 km/s. Since the ablation laser duration is 8 ns, and the relevant time scales are on the order of 100's of ns, there is no need to account for the difference in inception times for the different velocity bins in the experiment. The electric field to decelerated a $C^{4+}$ ion from 140 to 64 km/s over 100 ns is $E = \frac{m_C}{q_{C^{4+}}} \times \frac{\Delta v}{\Delta t} = 300$ V/cm, which is consistent with the calculated electric fields in figure 4.3 (d).

After the leading edge ions decelerate, the trailing ions have a faster speed. This is apparent in figure 4.3 (b) where the large signal of 104 km/s ions are initially located closer to the target than that of the 64 km/s ions. The faster shell of ions, which were not measured in this experiment at this early time, shielded the 104 km/s ions from the electric field induced by the Hall effect. Once the fast ions decelerate, the 104 km/s ions lead the expansion of the LPP cloud and drive

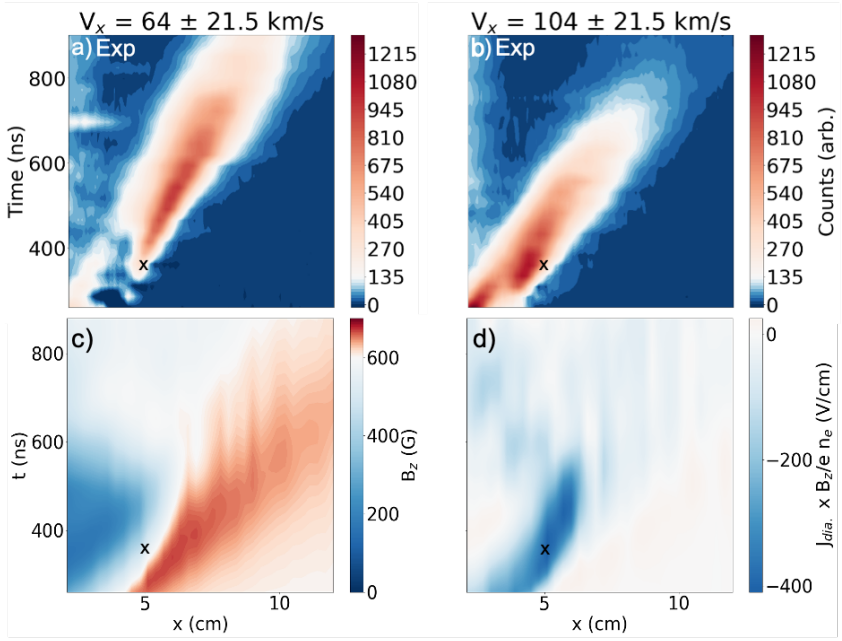


Figure 4.3: Panels (a) and (b) show spatio-temporal evolution plots of distance from target vs time of the $C^{4+}$ ions at two specified velocity bins collected in the experiment. Panel (c) displays the measured magnetic field traces along the blow-off axis of the expulsion/compression structure. Panel (d) shows the calculated electrostatic field strength in the x direction from $E_x = \frac{\mathbf{J}\times\mathbf{B}}{en_e}$. From Ampere's law the current is calculated as $J_y = \frac{c}{4\pi}\nabla \times \mathbf{B}$. This assumes a flat electron density, which while not entirely accurate, allowing for a rough calculation with spatial resolution. Combining these plots good spatial agreement is evident with the appearance of slow ions that are believed to have originated as fast ions in the spatial location where there are large electric fields. This point is marked with an "x" on the plots.

the diamagnetic currents which create the Hall electric fields. The leading edge ions decelerating and being overtaken by the trailing ions leads to the curved shape of the diamagnetic cavity edge, evident in both the magnetic field traces and the calculated electric fields. The is short lived due to the geometric dispersion of the LPP ions, and since the diamagnetic cavity dissipates and coupling ends. This is confirmed in figure 4.3 (d) where the calculated electric fields decrease rapidly after $\sim$ 500 ns.

The profiles in (a) and (b) after t $\sim$ 440 ns more closely resemble that of a ballistic model, signifying that coupling has been reduced greatly, if not completely ended. The apparent spreading of the signal from the inception location is due to the finite bandwidth of the probe beam. The lower bound of 43 km/s is the trailing edge and the upper bound of $\sim$ 85 km/s is the leading edge.

One additional note about the LIF streak plots is that one might initially assume the brightness

directly correlates to the density. However, care must be taken when comparing signal brightness across different times, since at later times there are more ions in the metastable state that are capable of fluorescing, weighed against the natural dispersion of the ions.

The equivalent simulation results for the spatio-temporal evolution velocity maps and the magnetic field are shown in figure 4.4, where the experimental data are shown in (a-c) and the simulation results are displayed in (d-f). Every plot included in Fig. 4.4 has identical axes: the distance from the target along the blow-off axis is plotted along the horizontal-axis and the time relative to the ablation beam along the vertical-axis. The distance and time of the PIC simulation is chosen to most closely resemble that of the experimental data even though the exact starting position and time are a bit ambiguous. There are notable similarities between the experimental and simulated data. The diamagnetic cavity shows approximately the same expansion speed and cavity expulsion and size, and the ion velocities follow a similar deceleration with good spatial agreement to the diamagnetic cavity.

### 4.3.2 Phase Space and Velocity Distribution Function

Here we show the full velocity distribution function at two times during the experiment. The top two images in figure 4.5 scan over the entire distribution of velocities in 14 m/s bins. There are a total of 20 velocities measured in the recreation of these. Constructing the phase space plot as outlines is section 4.3.1, allows for a comparison between measured and the simulated phase space plots. The simulated LIF results must be artificially broadened with the instrument function of the LIF beam in order to recover a true comparison to the experimental data. The experimental data (fig. 4.5 (a) and (b)) as well as the PIC results (fig. 4.5 (c) and (d)) show that the mean velocity of the $C^{4+}$ ions, directed along the blow-off axis, has slowed between 610 – 860 ns.

The deceleration observed at this later time is primarily due to the gyration of the ions in the magnetic field, which agrees well with the streak plots in Fig. 4.4. The coupling takes place primarily around 400 ns when a sharp deceleration of $\sim$ 40 km/s occurs over a duration of ten's of

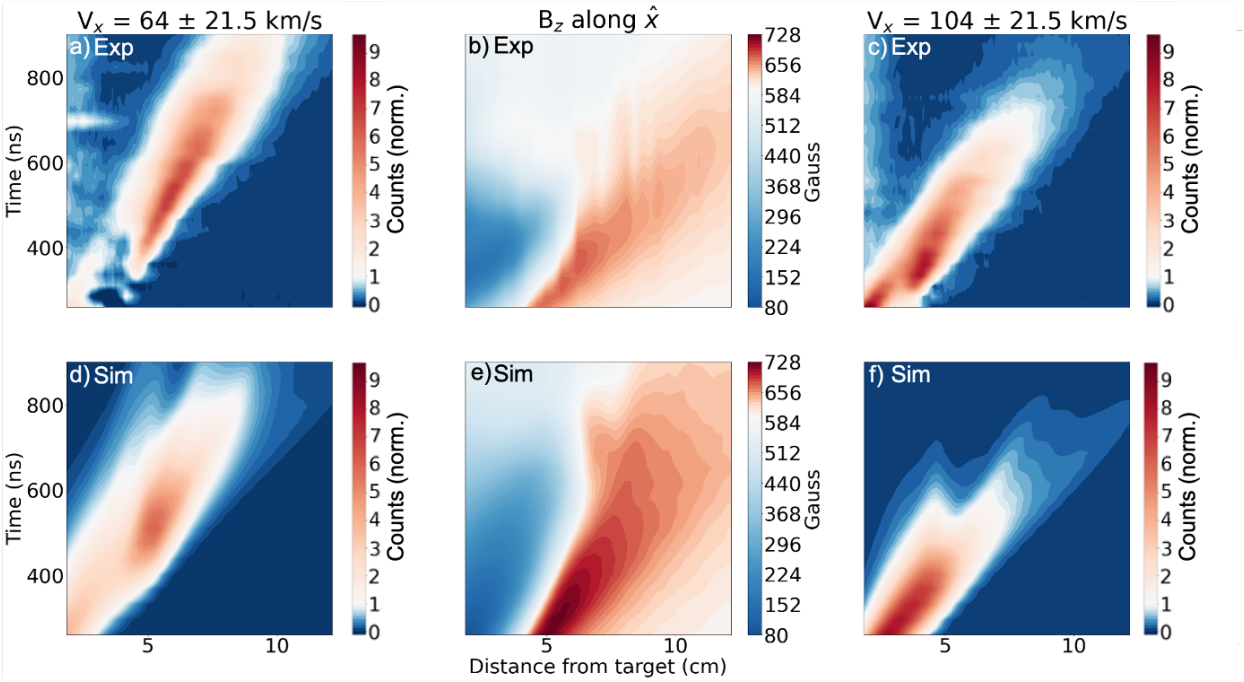


Figure 4.4: Panels (a) and (c) show spatio-temporal evolution plots of distance from target vs time of the $C^{4+}$ ions at two specified velocity bins collected in the experiment. Panel (b) displays the measured magnetic traces along the blow-off axis acquired from magnetic flux probes. Panels (d) and (f) show spatio-temporal evolution plots of distance from target vs time of the $C^{4+}$ ions at two specified velocity bins extracted from PIC simulations. Panel (e) shows corresponding magnetic field data from the simulations. There is an offset in time between the simulations and experimental data which stems from inception of the simulated LPP cloud over a larger spread than the experimental data. For simplicity all LIF data was normalized.

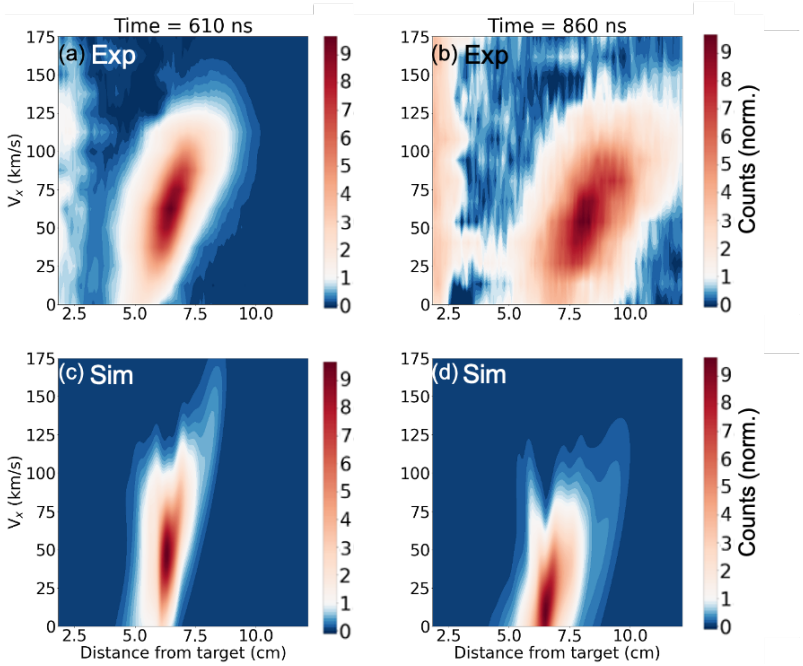


Figure 4.5: a) and b) Phase space plots at 440 and 690 ns, respectively, after ablation. Each velocity bin represents a different data run. c) and d) PIC simulation phase space plots at equivalent times which have been artificially broadened with the instrument function in order for a more direct comparison.

ns. The later time dynamics of the LPP ions is dominated by simple gyration in the magnetic field which shows a much more moderate deceleration along the x-axis of $\sim$ 15 km/s over $\sim$ 250 ns. A more detailed description of the transfer of energy is explored in the following section.

The broadening of the phase space is explained with the observed features in Sec. 4.3.1. Since the slower population of ions that are initially ahead are overrun by the faster moving ions, the times at which the phase space were measured show significant overlap between the two populations.

### 4.3.3 Energy Coupling

The reasonable agreement between the simulation and experimental data at later times (> 400 ns), giving confidence to the PIC simulation results of the coupling mechanism at early time (< 400 ns) which can reveal additional physics that was not measured in the experiment. One additional goal of this experiment was to validate the computational model.

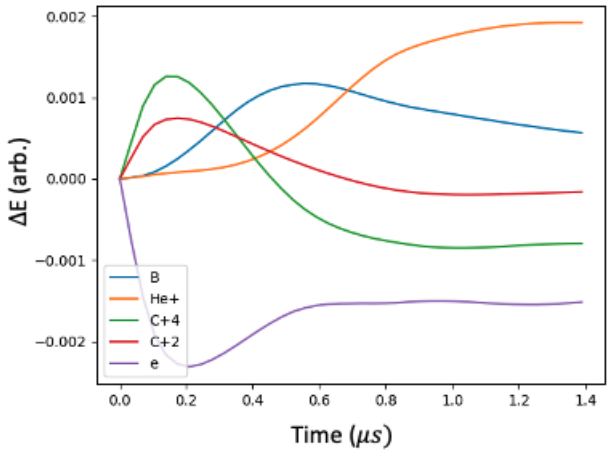


Figure 4.6: Simulation results showing the change in magnetic field energy B (blue), background ion energy $He^{+}$ (orange), laser-produced ion $C^{2+}$ (red) and $C^{4+}$ (green) energy, and the energy in the electron population *e* (purple) over time. The flow of energy is initially from the electrons to the LPP ions, then to the background field and finally to the background ions, as is expected in the sub-Alfvénic case.

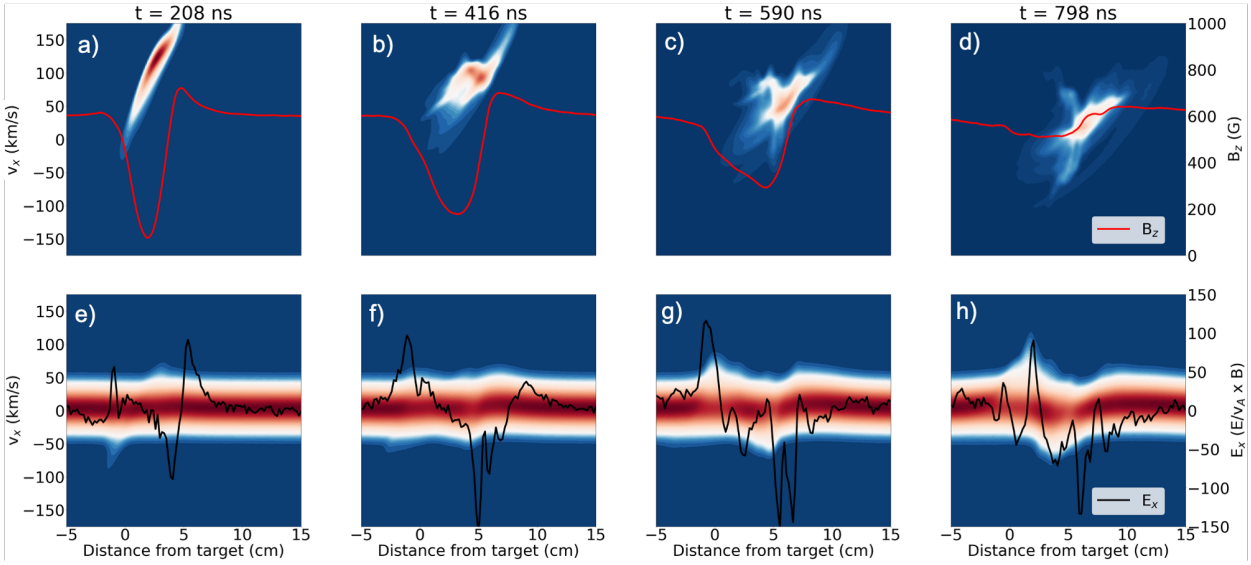


Figure 4.7: (a)-(d) Phase space plots of the $C^{4+}$ LPP ions (red/blue contour) as well as corresponding magnetic field profiles (red lines) at four characteristic times. These are the simulated values corresponding to measured quantities. (e-h) Phase space plots of the background ions (red/blue contour) as well as corresponding electric field profiles (black lines). These represent quantities not measured in the experiment, but are important for the complete story of coupling. The gyroperiod is 3.25$\mu$s.

Both the experimental data and the relative change in energy of each species in the model (Fig. 4.6) details the time of expected coupling between the LPP and magnetic fields. In Fig. 4.6, B represents the magnetic field energy, $He^{+}$ is the background ion energy, $C^{2+}$ and $C^{4+}$ represents the energy in each laser-produced ion species, and $e$ is the energy in the electron population. Due to the time step size ($t{\cdot}\omega_{c,e} \approx 0.04$), there is no distinction made between the quickly magnetized laser produced electrons and the background electrons.

The transfer of energy is separated into three phases as shown in Fig. 4.6. Initially ($0\ \mu s < t < 0.2\ \mu s$), the quickly magnetized laser plasma electrons accelerate the LPP ions. The high inertia, unmagnetized ions streams past the electrons and set up an electric field due to the charge separation. In the second phase ($0.2\ \mu s < t < 0.5\ \mu s$), the ambipolar electric field set up by the charge separation induces an E×B drift of the electrons, transferring energy from the ions to the magnetic field. In the final stage ($0.5\ \mu s < t$), the laminar electric field ($E_{lam}$) set up by magnetic pressure gradient as well as the LPP ion currents accelerate the background ions.

To further assess coupling, the time dependent VDF of both the LPP ions and the background ions alongside the electric and magnetic fields is examined through the simulated data. Four characteristic times of extracted from the PIC simulations are displayed in Fig. 4.7. The times chosen are near 200 ns, 400 ns, 600 ns, and 800 ns. These correspond to the times near maximum LPP ion energy, maximum transfer of energy from LPP ions to magnetic field, maximum energy increase of the background ions, and finally the stabilizing of the LPP ions energy.

By t = 208 ns the laser plasma is freely streaming, and, via interacting with the electrons, has set up the magnetic cavity ($B_z$(x=3cm, t=208 ns) = 80 G) which is represented by the red profile along the top row of plots. The background ions remain relatively stationary as depicted in the bottom row of plots. The LPP ions are exhibiting ballistic motion, which is evident as faster moving ions have traveled further. This motion forms the diamagnetic cavity. The electric field from spatial magnetic gradients is forming, and directed towards decreasing magnetic field.

At the next time step (416 ns) the initial signs of ions departing from ballistic motion is observed. The ions that are further out in space are observed to be traveling at a lower directed velocity, similar to the LIF data shown earlier. Within the mass of LPP, there are two distinct red points, where the leading point is at a slower speed. By comparing the spatial position with the electric fields in (f) the mechanism for this deceleration is in agreement with the space charge electric fields. This is further pronounced in Fig. 4.7 (c) where particles at the magnetic ramp ($\approx$ 5 cm) are decelerating along the blow-off axis. This spread in ion velocities coexisting at the magnetic ramp (at 6 cm) in the phase space plot is the departure from ballistic motion that indicates coupling and is the mechanism that leads to a slower population of ions (64 km/s) out in front of faster ions (140 km/s) observed in the spatio-temporal evolution maps in Sec. 4.3.1. The LPP ions that most effectively couple energy to the background are those with sufficient density. Figure 4.7 (c) shows that this leaves the diffuse (very low density), highest velocity "vanguard" layer of LPP ions relatively unaffected as well as the diffuse slower ions. After t = 590 ns the LPP ions become too diffuse and slow to maintain the diamagnetic cavity. Therefore the space charge separation electric fields diminish and coupling ends.

At these same times (Fig. 4.7 (f) and (g)), the laminar electric field due to gradients in the magnetic fields are developed. Now that the electric fields have grown and sufficient time has passed, the background ions begin to get swept up in the wake of the LPP ions. At the trailing edge of the bubble (where the magnetic field is sloped downwards) both components of $E_{lam}$ are directed in the +x direction. Comparatively, in the region where the magnetic field slopes upwards, the magnetic pressure term points in the -x direction, and since it dominates in comparison to the Larmor term, background ions are accelerated to negative velocities. This is reflected in the VDF of the background where ions are accelerated to higher positive velocities than negative velocities.

At the final time step (798 ns) these effects further develop. As shown in Fig. 4.4 (a) and (c) there are LPP ions of quite different velocities piled up at the edge of the diamagnetic cavity and the cavity has largely collapsed. More of the background ions have been picked up by the electric

fields and a population have been accelerated to speeds higher than the bulk of the LPP. Since the LPP was not sufficiently populous the coupling was not sufficient to see any separation of the LPP from the background accelerated ions.

## 4.4 Summary

The collective electromagnetic interactions that couple energy from a sub-Alfvénic laser produced plasma to a pre-formed, magnetized background plasma are explored via a novel laser induced fluorescence diagnostic. Time streaks of two ion velocities and velocity distribution functions at two given times are compared to measurements of magnetic compression and diamagnetic cavity formation. The observation of LPP ions departing from ballistic motion corresponding to collisionless coupling of LPP-background coupling is understood through modeling the experimental data.

- Three-dimensional, fully kinetic particle-in-cell simulations reproduce both the magnetic field and particle data and show that the LPP ions couple energy to the background upon crossing the large magnetic field gradient at the edge of the diamagnetic cavity. The discrepancies observed when comparing the PIC results to the measured data stem from the large spatial spread in the ions when being initialized compared to the experiment, as well as the inherent dependence of the experimental LIF data on the density of the ions.

- This experiment mapped out the 2D spatial extent of two velocity bins, and two time delays of the velocity along the blow-off axis. Future experiments on the LAPD will map the full extent of the velocity space, as well as the transverse velocities, in order to gain more insight into laser-target interactions.

- In addition to the increased extent of mapped parameter space, the plasma conditions will be improved in the context of quasi-perpendicular collisionless shock formation [9, 77, 66]. The combination of a higher energy laser system ( 20 J) [78], which is expected to create a

faster LPP expanding into a hotter, denser background plasma from an improved source, will push the experiment well into the super-Alfvénic regime.

- Although this diagnostic was developed with the intention of measuring carbon ions ablated by a moderate intensity lasers ($\approx 1 \times 10^{11} - 1 \times 10^{13}$ W/cm$^2$), the technique can be adapted to a variety of experiments that generate compatible C charge states.

- For example, it may be possible to use this technique in inertial confinement fusion (ICF) experiments. While in typical ICF experiments the high laser intensities ($I_l \approx 1 \times 10^{15}$ W/cm$^2$) will initially create a much more highly ionized plasma ($\overline{Z} \sim 6$), C ions compatible with this LIF scheme have been observed in gas-filled capsule implosions[2], possibly due to the collisionality of these plasmas. Further studies would indicate if this technique would be feasible in such environments. In order to probe the timescales of such experiments a short pulse (~ps) laser would be required.

- This technique could be further extended by using two-photon LIF [14, 57] which is capable of measuring ion properties such as temperature and density, as well as ambient properties such a magnetic or electric fields with the caveat that the high intensities required would limit the measurement to a single point, reducing the spatial information gained. This technique has not yet been explored in our configuration due to high probe beam intensity required to perform two-photon LIF, as well as the low spatial resolution of such a measurement.

# CHAPTER 5

# Super-Alfvénic Coupling

## 5.1 Overview

The expansion of a super-Alfvénic, quasi-perpendicular LPP into a relatively tenuous magnetized plasma has been investigated. The energetic carbon (C) ions couple energy and momentum to the helium (He) ambient ions through large scale laminar electric fields (eqn. 1.10) over length scales that are much shorter than the ion-ion collisional mean free path ($\lambda_{ii,mfp}$).

Magnetic pressure gradients ($\mathbf{E}_{press}$ in equation 1.10) along the edge of the diamagnetic cavity are enhanced by the ambient plasma density. These are strongest transverse to both the blow-off axis and magnetic field and act to collimate the LPP flow into a jet-like structure as depicted by the blue arrows at $t_1$ in figure 5.1. These fields are created at frequency close to the ion-cyclotron frequency which drives the collimation off axis in the azimuthal direction.

This collimation into a jet-like feature results in a high current density that extends well past the diamagnetic cavity, allowing for the Larmor electric fields ($\mathbf{E}_{Lar}$ in equation 1.10) to accelerate the ambient plasma consistent with an $\mathbf{E}\times\mathbf{B}$ drift. This is depicted in figure 5.1 at $t_2$. A similar focusing via magnetic pressure has been observed in the expansion of an LPP into a strongly magnetized vacuum [70], and due to a curvature in the polarization electric field [61, 88]. The polarization driven case involves a low $\beta_k$ LPP where the magnetic field is not significantly perturbed. Here, the self-focusing and additional cross-field transport is primarily due to the magnetic pressure. This is in agreement with Brenning et al. in their comparison of high to low $\beta_k$ plasmas [16].

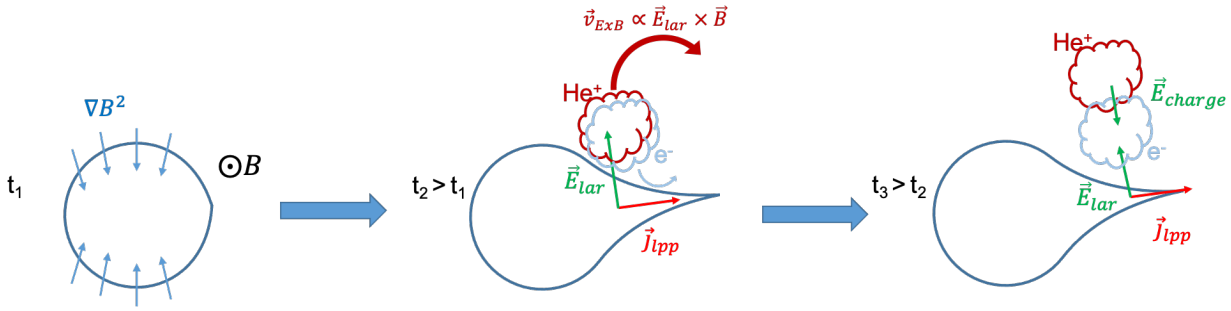


Figure 5.1: Illustration of the formation of the blob and small magnetic compression. As the LPP ions converge into the jet, the strong Larmor electric fields cause an E × B drift in the ambient plasma. At $t_2$ the Helium and electron population is coincident with the LPP jet, but for simplification in the illustration is is shown above the jet. This accelerates the helium ions upwards, due to the large gyro-radius, while moving the electrons primarily perpendicularly to $E_{Lar}$. This sets up electric fields along the outside of the electron population that expels the local magnetic field and compress the magnetic field above the blob.

The relatively large gryoradius of the ambient ions compared to the electrons will cause a charge separation electric field ($\mathbf{E}_{charge}$ in figure 5.1 at $t_3$). This electric field is directed anti parallel to the Larmor term and creates an additional structure in the magnetic field that extends past the bulk diamagnetic cavity. This "blob" (as it is generally referred to in 2D) is a slice of a filament structure.

Similar blob (2D) or filament (3D) phenomena have been observed in both flux tube transport in ionospheric events such as the Starfish* experiment [94], as well as in cometary transit [51] where blobs are observed to co-move perpendicular to both a jet-like structure and the solar magnetic field. The creation and transport of blobs are often tied to a polarization drift which results from a static electric field that arises due to the difference in gyro-directions of the electrons and ions. However, this is only the case when the magnetic fields are not significantly altered. These blobs have frequently been observed to cross field lines, and transport energy along magnetic field line. To our knowledge, this is the first time a blob has been studied in such a transient laser-produced plasma. One prior study saw an increase in visible light congruent with the location and timing of the blob, but it was not discussed in their findings and it is unclear if the same phenomena is the cause [13].

Here, the formation and separation of a blob from the bulk diamagnetic cavity is explored by measuring the time evolving magnetic fields (bdot probe) and the velocity distributions of the LPP

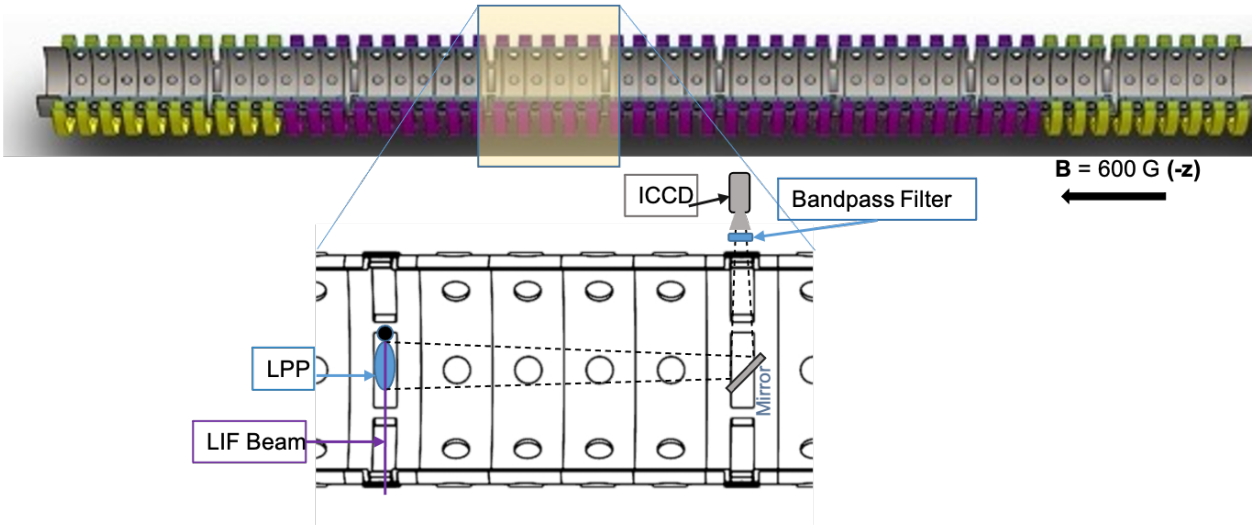


Figure 5.2: Schematic of the experiment. The LIF measurement was imaged along the axis of the LAPD through a turning mirror embedded in the LAPD.

plasma (LIF). In order to measure the reaction of the ambient plasma to the LPP, the helium plasma is imaged through a bandpass filter.

## 5.2 Experimental Setup

The experimental setup is illustrated in figure 5.2, and shares a great deal with the setup in the previous chapter [28]. The Peening laser system (1053 nm, 14 J, 14 ns FWHM) is used in place of the SpectraPhysics laser for the purpose of ablation, which increases the on target intensity to $\sim 1 \times 10^{12}$ W/cm$^2$. The focusing lens has remained unchanged, which results in a similar spot size between the experiments. Despite this, the number of ablated ions increases by nearly an order of magnitude, as well as the on-axis velocity increases by roughly a factor of three [78].

The collection optics system for the LIF diagnostic has significantly changed from the sub-Alfvénic setup. Here we image the LIF beam along the axis of the machine in order to observe the xy plane. A turning mirror is inserted from the west side of the LAPD with a mirror reflective in the UV. The LIF is imaged though the same bandpass filter. The ICCD camera has been upgraded from the prior experiment. The new PIMAX4 camera has a generation II intensifier that is optimized for the

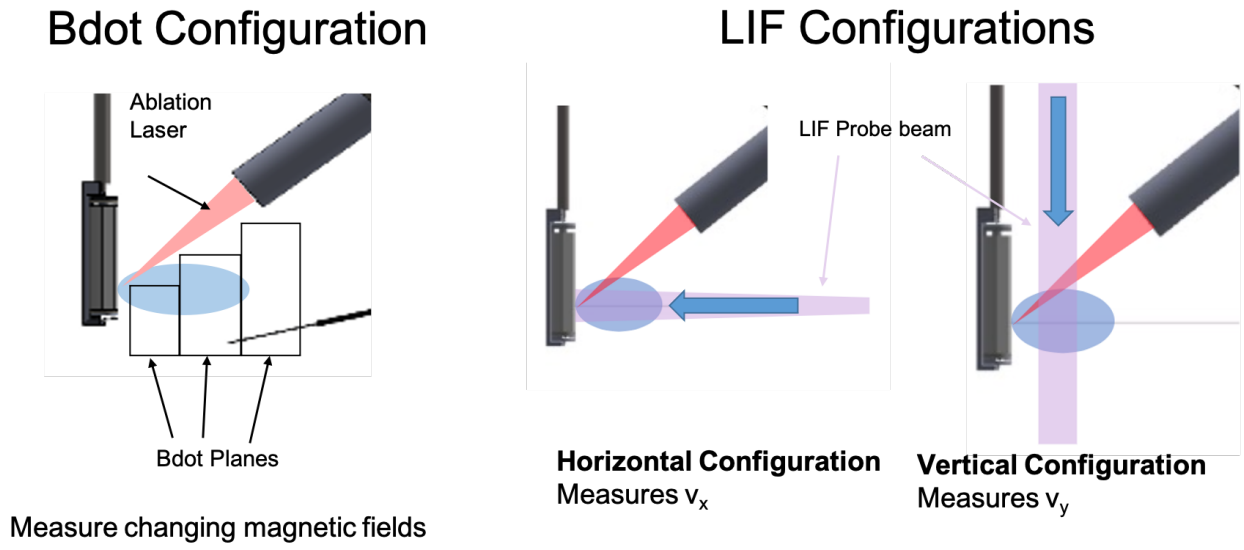


Figure 5.3: Diagram showing the different diagnostic setups used for this experiment. The bdot configuration shows the three xy planes where data was acquired. In order to avoid the ablation laser path the extent of each plane was limited in y according to x positions. The LIF parallel configuration shows the geometry chosen for measuring the x component of the LPP velocity. The LIF perpendicular configuration shows the geometry for measuring the y-component of the LPP velocity. Since a pencil beam was used for this measurement, the LIF probe beam was scanned along the x direction to measure the transverse velocities at different spatial positions.

UV, with an imaging array of $1024 \times 1024$ pixels, 16 bit digitization, and increased sensitivity in low level light detection.

A helium ion density of $2.1 \times 10^{13}$ cm$^{-3}$ was achieved in this experiment through the use of the LAPD gas-puffing device near the south end $LaB_6$ cathode. The LPP expanded into the main discharge of the LAPD and so the electron and ion temperatures for this experiment were higher as a result.

In the sub-Alfvénic experiment, the LIF probe beam was expanded into a 5 cm thick sheet in the xz plane. This worked well, in that the intensity of the beam was constant throughout the entire length of travel to a good degree which meant that there was a higher chance of the LIF beam to cause fluorescence. The drawback being that the measurement was effectively 1D and interesting results were potentially missed.

Here, the probe beam was fanned out along the xy plane and focused along the z direction (as

shown in fig. 5.3 (b)). This resulted in a larger region in which the dynamics of the LPP could be observed, but without confidence of the exact intensity of the beam at any given point. As the priority was to measure velocity and not the density, this was an acceptable trade-off. Given that the angle of the beam is relatively small (5 – 10 degrees), it is safe to assume that the x-direction of the LPP velocity was measured.

In addition to measuring the LPP parallel velocity, $v_x$, a second probe beam geometry was implemented to measure the transverse velocity of the LPP along the y-direction. In this configuration (fig. 5.3 (c)) the LIF beam enters through a quartz window on the top of LAPD and passes through the LPP in the negative y-direction. This causes fluorescence in the ions with a specific y-component of velocity according to the wavelength of the probe beam. This measurement proved to be more sensitive to the intensity of the probe beam, and therefore the beam was not fanned out along the direction of travel and remained at 1 cm wide. In order to acquire data from an area with a width larger than the beam waist, the beam was scanned along the x-axis to measure a larger area. Measuring the transverse component of the LPP velocity allows the observation of the effects of the laminar electric fields, as they primarily act in the y direction for the setup described here.

For each measurement, 50 shots (25 background and 25 signal) were acquired, averaged and subtracted in order to have sufficient signal. The number of shots necessary to produce a reasonable signal was much greater than in the sub-Alfvénic experiment. There are three possible explanations for this: the higher velocities in this experiment causes the density to drop much faster based on geometric arguments, increased ablation laser intensity produces more higher charge state ions in the LPP, and the LIF laser energy had anomalously dropped by nearly a factor of two, likely pushing the measurement well outside of the saturation region.

A few examples of the LIF measurement are shown in figure 5.4, half in the parallel configuration and half in the perpendicular configuration. The images shown here act as a benchmark in order to confirm that the LIF diagnostic is consistent with a time-of-flight model where ions are spatially located according to their speeds. Based on the good agreement, we can confidently use the LIF

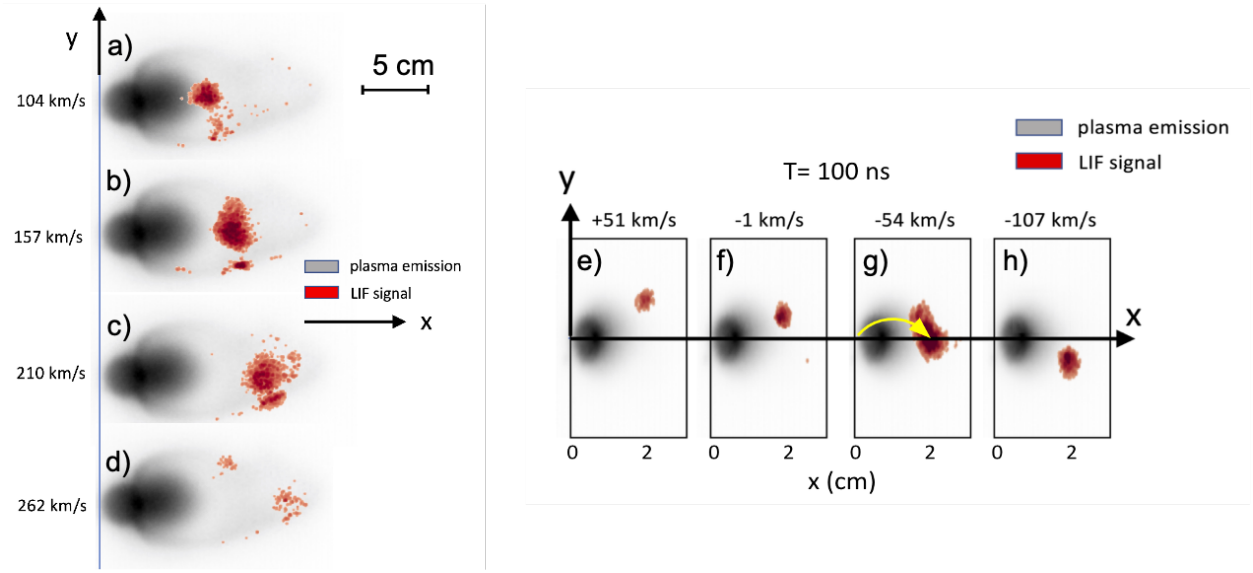


Figure 5.4: Eight images showing the LIF signal in red overlayed on top of the LPP self-emission in grey scale at the same time. The red signal representing the LIF measurement is referred to as a heat map. These images show that the LIF diagnostic works well on ions moving ballistically (ions that are measured as moving faster are further away from the inception point). (a-d) displays the LIF in the parallel configuration in which measured $v_x$. There is a very strong signal in three of the four velocity bins measured that are in good agreement with ballistic motion. (e-h) display an example of the LIF measurement in the perpendicular configuration which is consistent with ions that have gyrated a small amount (small negative values of $v_y$ on the axis). These measurements which are held to a higher scrutiny (i.e. signal closer to the noise level has been cut) for the acceptable S/N ration giving confidence that the diagnostic works well and can be used to assess more subtle features.

investigate more subtle features along the edge of the cavity and extending past the cavity where the dynamics are far more complicated.

The bdot probe was fielded in the same xy plane as the LIF beam for comparison. Multiple xy planes are stitched together in order to avoid the ablation beam path, while also measuring the largest possible interaction region. A visualization of the three planes measured is shown in figure 5.3 (c).

These experimental differences between the sub-Alfvénic and super-Alfvénic experiments are summarized in table 5.1. The key differences in the formation of the blob are the increase in number of LPP particles and bulk LPP flow.

| | sub-Alfvénic | super-Alfvénic |
|---|---|---|
| | Ambient Plasma | |
| Magnetic Field (G) | 600 | 600 |
| $n_{He^+}$ ($cm^{-3}$) | $1.6 \times 10^{13}$ | $2.1 \times 10^{13}$ |
| $T_e$ (eV) | 1 | $5 - 10$ |
| $d_i$ (cm) | 11.5 | 10 |
| $v_A$ (km/s) | 160 | 140 |
| | Ablation Laser | |
| $E_l$(J) | 1.5 | 14 |
| $I_l$ $(W/cm)^2$ | $10^{11}$ | $10^{12}$ |
| $\tau_l$ (ns) | 10 | 14 |
| | Laser-Produced Plasma | |
| N Particles | $\sim 10^{15}$ | $\sim 2 \times 10^{16}$ |
| Bulk Initial Velocity | $0.6v_A$ | $1.5 - 2v_A$ |
| Bulk Ion Species | $C^{4+}$ | $C^{4+}$ |
| Diamagnetic Cavity Size (cm) | $0.4\ d_i$ | $\sim d_i$ |

Table 5.1: Summary of differences between the sub-Alfvénic and super-Alfvénic experiments. The increase in LAPD ambient density leads to a smaller Alfvén speed and smaller ion inertial length. The more substantial experimental difference was the increase in ablation laser energy results in a much faster blow-off speed and larger cavity size. The ion species that dominates in terms of kinetic energy density remains $C^{4+}$.

## 5.3 Experimental Results

This section details the experimental results of a super-Alfvénic LPP expanding into a magnetized ambient plasma.

The first part discusses the effect of the increased density to the diamagnetic cavity formation and shape. Without these high densities, the magnetic pressure would not be sufficient to collimate the LPP flow into a jet.

The second part details how the LPP focuses into a jet.

Finally the third shows how the jetting into the high density magnetized plasma forms the blob.

### 5.3.1 Coupling Length Scales Determined by $M_A$

As discussed in chapter 2, the size and shape of the diamagnetic cavity depends on the contribution of energy transferred to the magnetic fields and ambient ions. In the limit of a sub-Alfvénic expansion ($v \ll v_A$), the contribution of the ambient ions is small and the magnetic stopping radius dictates the cavity size. Conversely, in the far super-Alfvénic limit ($v \gg v_A$), the contribution of the magnetic field is small and the equal mass radius determines the diamagnetic cavity size.

In the low, super-Alfvénic Mach number case ($v \sim 1-2\, v_A$) neither of these simplifying assumptions can be made and the LPP expansion is stopped by both the ambient ions and the magnetic field. In order to test the contribution of each, a bdot probe measured the diamagnetic cavity size and timing with and without an ambient helium plasma. These data will be referred to as the ambient plasma, or $LaB_6$ cathode, being "on" or "off". When the cathode is off, the ambient plasma density is negligible and therefore the cavity is determined by the energy transferred to the magnetic field alone, which is comparable to when the LPP expands into magnetized vacuum. During the plasma off runs, the gas puffing system was also turned off so as to reduce the pressure further in the LAPD, ensuring a collisionless interaction. As the magnetic field produced by the coils surrounding LAPD work to confine the ambient plasma, testing the expansion into an unmagnetized plasma in the LAPD is not possible. Comparing the cases of expansion into plasma and vacuum allows the validity of equation 2.3 to be tested.

Figure 5.5 shows a comparison of $B_z$ along the blow-off (x) axis versus time with (a) and without (b) the ambient plasma. In addition to the full streak plots shown in (a) and (b), lineouts along the x-axis at a specific time are displayed in the plots directly below. These show $B_z$ (blue), with the calculated $E_{press,x}$ (orange). The peak value of the diamagnetic current (spatially located at the peak of the orange trace) at t = 500 ns is taken as the stopping radius for each case.

Evaluating the stopping radii with equation 2.5 reveals that the Alfvénic Mach number is $M_A \sim 0.8$. This number is substantially lower than expected based on measuring the LPP velocity with the

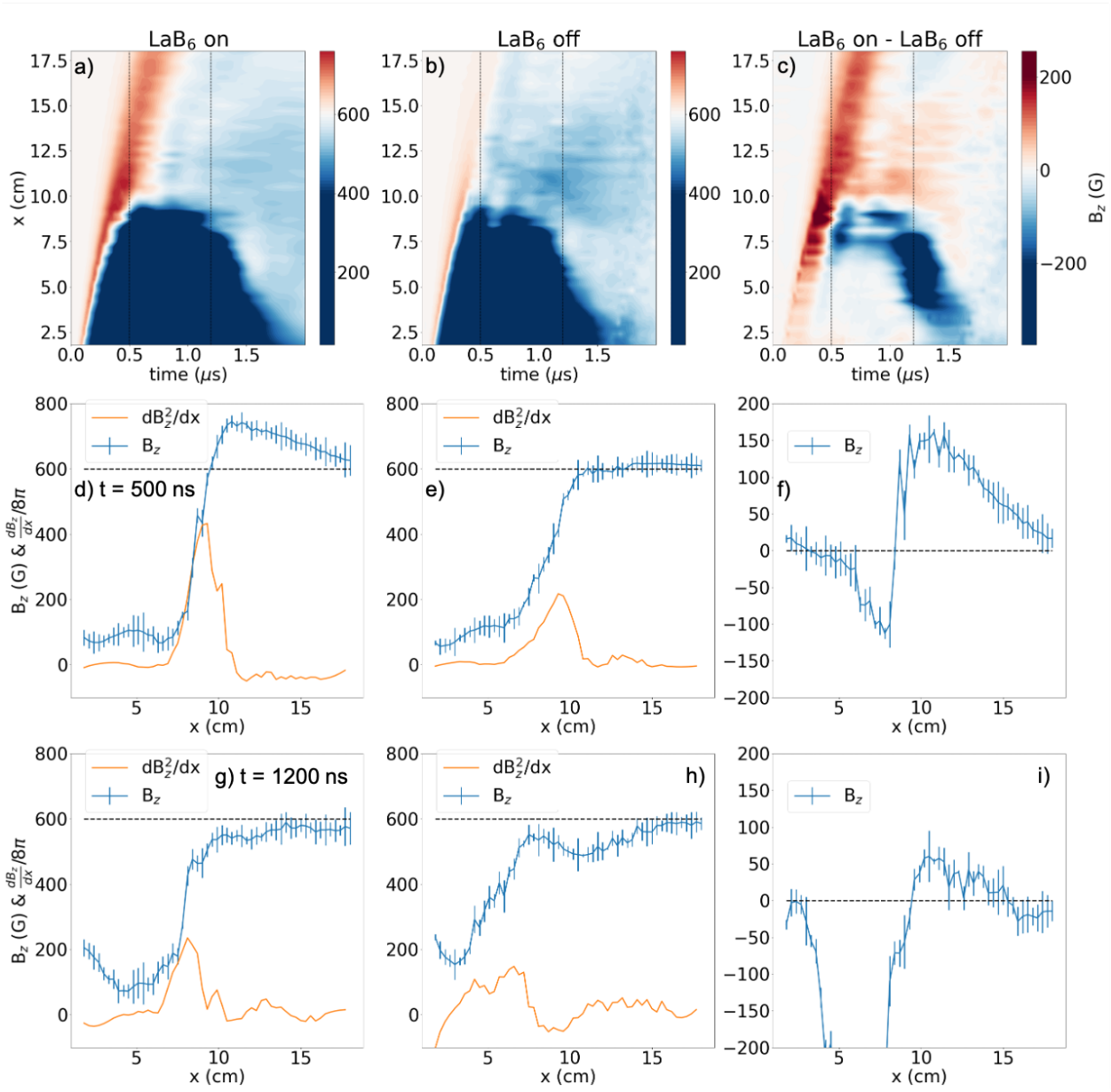


Figure 5.5: Streak plots of $B_z$ as a function of time and x are plotted for the case of expansion into a magnetized ambient plasma (a) and only a magnetic field (b) with the difference between the two in (c). The lines on the contour represent two characteristic times and are displayed along the following rows. At 500 ns, the time of peak diamagnetic current, the effects of the ambient plasma are observed in the increased calculated electric fields by over a factor of two. This increase in the collimating electric fields force the LPP flow back towards the axis of symmetry. At 1200 ns, the time at which the blob gyrates back to the x-axis, there is a region of magnetic expulsion far out past the main cavity in (g) whereas there is no such structure in (h). This is exaggerated in (i) which shows the difference between the two.

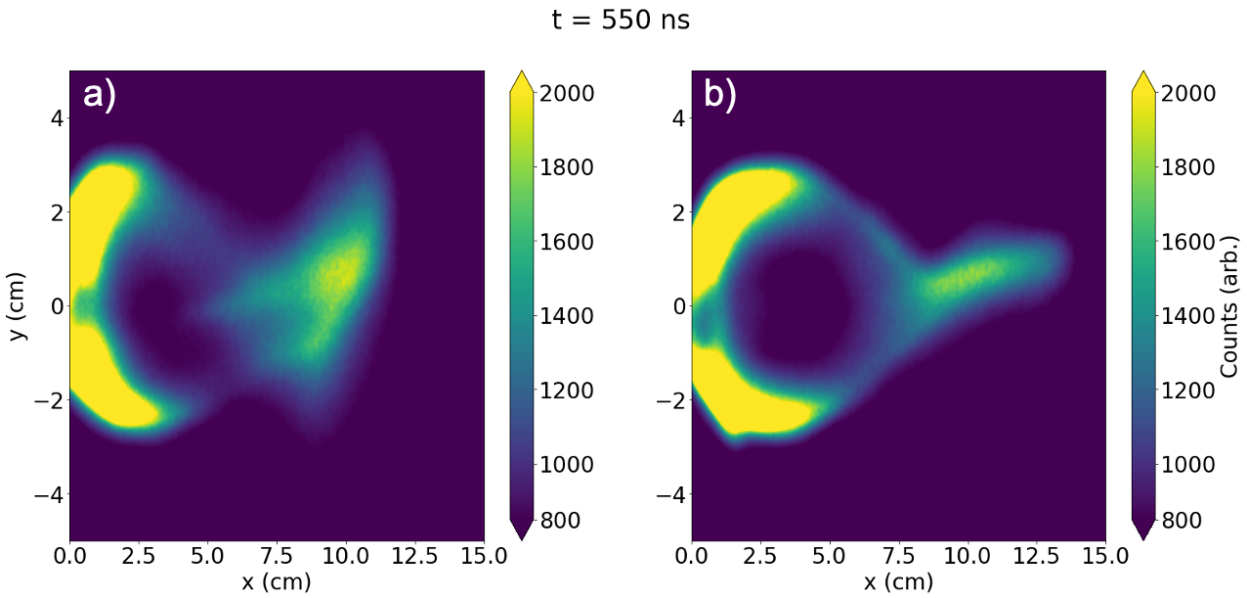


Figure 5.6: Images taken of the LPP self-emission expansion at t = 550 ns relative to ablation laser. Both images are taken through a bandpass filter centered around 227 nm light. Within the bandpass filter are prominent self-emission lines for $C^{2+}$ and $C^{4+}$ which are the dominant ions in terms on the kinetic energy density of the LPP. The proportion of $C^{2+}$ to $C^{4+}$ is identical between the two cases. Emission from other ion species has been filtered out which explains the gap between the leading edge and the light closest to the target. (a) is the expansion into magnetized vacuum (with the gas puff turned off) and (b) is the expansion into magnetized plasma. y comparing the two images, the effects of the ambient plasma on the self-focusing of the LPP is evident. The ambient plasma increases the magnetic pressure which helps to confine the LPP. This increased confinement allows for additional cross-field penetration, as shown in (b) extending further along the x-axis than (a). The polarization electric fields are present in each case and cause the off-axis tilt in the electron gyro-direction ($+\hat{y}$).

LIF diagnostic and calculating the Alfvén speed from the density measurement and magnetic field value (see table 5.1). The main contributor to the error in calculating the Alfvén speed in this way is the assumption that the LPP expands similarly in both cases, or that the volume of the LPP in each scenario is accurately described by one radius. The bdot data for the expansion into vacuum was only taken along the x-axis and limits the comparison to one-dimension.

By referencing images of the LPP expansion, as shown in figure 5.6, a qualitative difference in the stopping volume is observed. The images in fig. 5.6 show the expansion of the LPP at t = 550 ns into magnetized vacuum (a) and plasma (b). Light is filtered through a bandpass filter centered at 227 nm which only transmits light from $C^{2+}$ and $C^{4+}$ self-emission. The proportion of $C^{2+}$ to $C^{4+}$ is identical between the two cases. This explains the gap between the leading edge and the trailing edge in each image. The difference in expansion along the y-axis between the two cases is significantly larger than the difference in x-axis expansion. The Mach number would be more accurately calculated in this way if a 2D measurement of the cavity was taken with the bdot.

The collisionality condition must be revisited when considering the expansion of the LPP into a magnetized gas to ensure that energy is not being transferred from the LPP ions to neutrals via collisions. The approximate collision frequency for ion-ion collisions in a plasma is [86]

$$\nu_s^{i\beta'} = 9 \times 10^{-8} n_{i'} Z^2 Z'^2 \lambda_{i,i'} \left( \frac{1}{\mu} + \frac{1}{\mu'} \frac{\sqrt{\mu}}{\epsilon^{3/2}} \right) \tag{5.1}$$

which equates to $\lambda_{mfp} = 125$ m. The relevant mean free path for ion-neutral collisions is one for resonant charge exchange, which dominates compared to both the polarization attraction and the collisional excitation in the energy regime for the carbon ions in this experiment. Once again experimental findings from Phaneuf et al. [69] are adopted to see that that $\lambda_{mfp} \sim 60$ m. Despite the factor of two difference in mean free paths, the interaction length scales still far outweigh the experiment length of 10 cm.

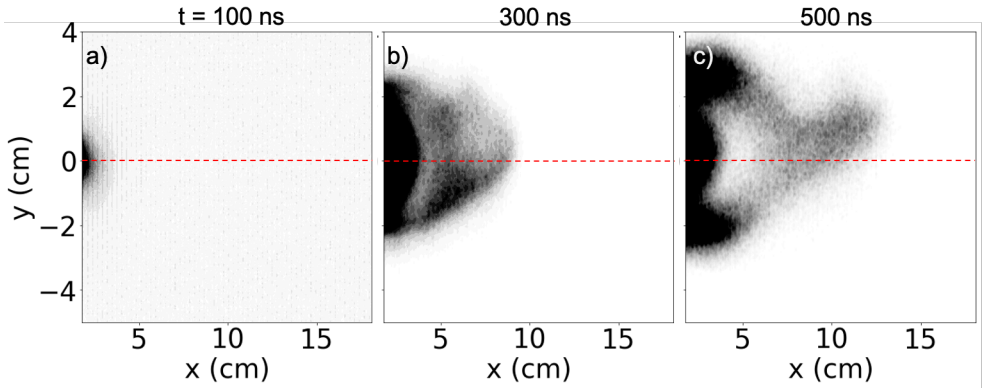


Figure 5.7: Self emission images of the LPP at 100, 300, and 500 ns. The light is predominantly from $C^{4+}$ ions, but includes light from other C ion self emission. At early times, the LPP expands primarily along the x-axis. Continuing further out in time the formation of a jet-like structure appears at the leading edge of the expansion of the plasma off from the axis of symmetry. The structure moves upwards, opposite of the gyromotion of ions in the applied ambient field of LAPD. A red dotted line is plotted along the x-axis for reference. The formation of the jet is a result of the magnetic pressure that acts along the edges of the LPP flow. The upwards tilt of the jet is a result of the polarization drift acting on the ions.

### 5.3.2 Convergence of Flow into Jet-like Structure

In the overview of this chapter, it was discussed how the magnetic pressure gradient at the diamagnetic cavity edge focuses the LPP along the dimension transverse to both the magnetic field direction and the blow-off axis (figure 5.1 at $t_1$). It was shown in the section above that the presence of the ambient plasma enhances this effect. This is accompanied by an induced drift which collimates the flow off-axis. This effect can only be observed in the xy-plane. The magnetic pressure gradients are substantially smaller in the $\hat{z}$ direction, and so the same collimation is not observe in the xz plane (see chapter 4). Here I will discuss in more details the convergence of the flow into a jet.

In the first stage of the LPP expansion, the directed ram pressure of the LPP ($0.5 m_i n_i v_i^2$) greatly exceeds that of the ambient magnetic field ($B_0^2/8\pi$). The ratio between the LPP ion kinetic ram pressure and the magnetic pressure is the kinetic beta, $\beta_k = 0.5 m_i n_i v_i^2/(B_0^2/8\pi)$. The general shape of the LPP closely resembles that of the ballistic expansion into B = 0 where the leading edge forms a $\cos^2(\theta)$ distribution, where $\theta$ is from the x-axis [44]. This is reflected in the shape of line-integrated, unfiltered images of the LPP (figure 5.7 (a)) and the still forming diamagnetic cavity (figure 5.8 (a)). In figure 5.8 $B_z$ is represented by the contour, and the magnetic pressure

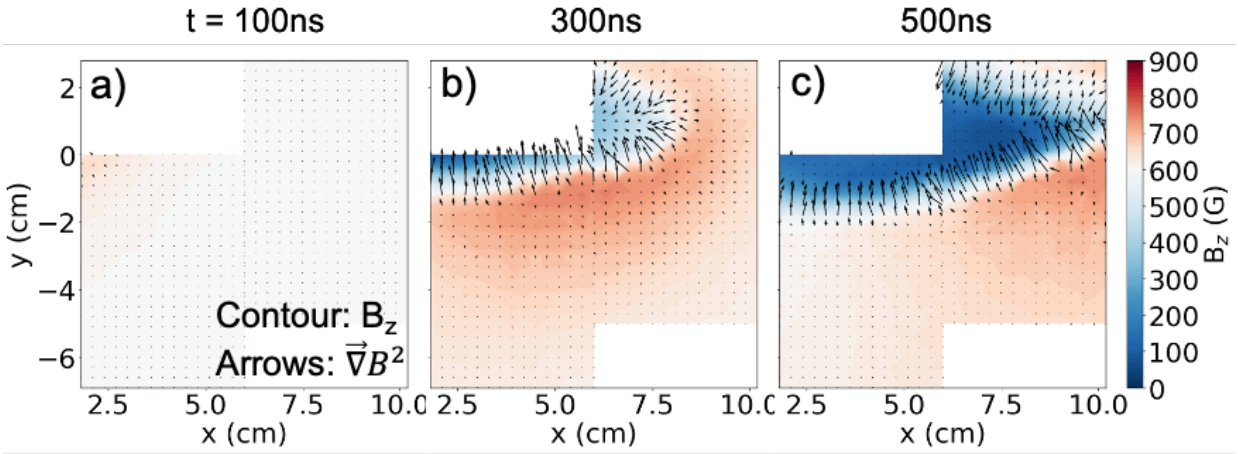


Figure 5.8: Two dimensional bdot scans are shown at three times. Two separate planes are stitched together in order to scan over a large area from $1.8 < x < 10.1$ cm and $-6.5 < y < 2.8$ cm, while also avoiding the ablation laser path. The contour represents the magnetic field along the axis and the arrows represent the calculated magnetic pressure term in the laminar electric field equation. At 100 ns the compression is first observed to enter the field of view. The magnitude of the magnetic pressure is small and is not yet visible. At 300 ns the magnetic compression is observed off axis by roughly 1 cm in the -y direction. The large magnetic pressure along the cavity edge is shown by the highly localized black arrows. At 500 ns the full extent of the diamagnetic cavity is shown and a discrepancy of the magnetic pressure strength along the top and bottom of the diamagnetic cavity. If integrated along the y-axis there is a net positive pressure in the y-direction. Here a zoomed in image of the diamagnetic cavity is shown. The development of the blob is outside of the frame of these images.

gradient driven electric fields are represented by the arrows, which are calculated from equation 1.10.

The early time LIF measurements agree well with the bdot data and unfiltered images. The LPP ions travel relatively unimpeded with shells of faster ions further out in space than slower ions. This is evident in fig. 5.9, which displays six parallel velocities at t = 100 ns. The transverse LPP velocities at the same time are shown in figure 5.10 (a-d) agree well with the expected motion of ions with larger y velocities extending further from the x-axis. There is a slight offset in y-velocities, as seen with y = −54 km/s directed velocity on axis and the bias of x = 262 km/s towards the negative y. These are consistent with ions gyrating in the magnetic field for 100 ns, corresponding to 0.2 radians. This is considerably different from the expansion into unmagnetized vacuum as seen in figure 3.8 at the same time. A comparison to the sub-Alfvénic experiment is challenging due to the difference in ablation beam and imaging orientation.

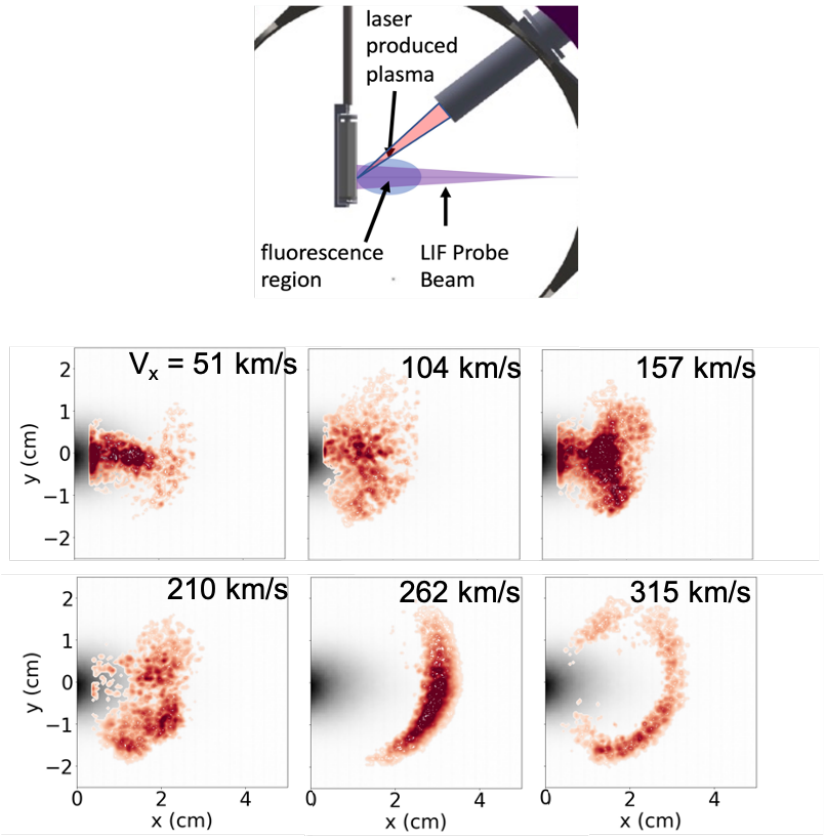


Figure 5.9: An illustration of the parallel LIF setup is displayed on the top. The six velocity bins collected at t = 100 ns are shown. Ar early times, the LPP expands freely, closely following a $\cos^2(\theta)$ model. The background grey-scale contour is the self emission of the LPP which is integrated over the line of sight and all wavelengths and the red contour represents LIF data.

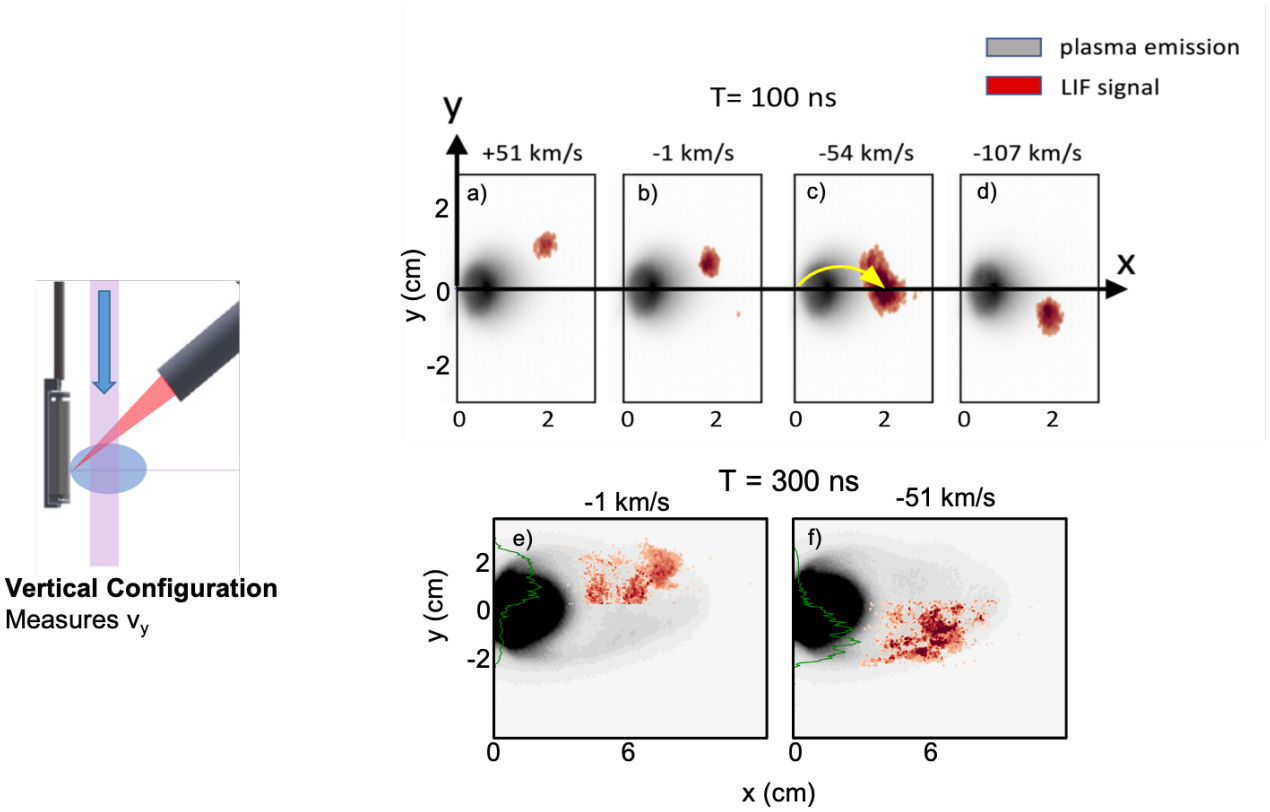


Figure 5.10: An illustration of the complementary setup for perpendicular velocity measurements is shown on the far left. Four velocity bins are measured at this time, ranging from $-107 - 51$ km/s. This data is also in good agreement with a ballistic expansion of the LPP ions. At t = 100 ns the LPP expands ballistically, which is represented by the approximately Maxwellian spread in the velocity profile. Once the magnetic pressure forces have begun to act and restrict the LPP transverse motion, the spread in velocity becomes much more leveled out in y-direction.

As the ions continue to expand, the diamagnetic currents increase and form the diamagnetic cavity and field compression structure. The diamagnetic cavity and magnetic pressure gradient vectors are now evident in figure 5.8 (b). Since the magnetic compression ($\delta B_{compression} \sim 0.3 \times B_0$) observed in this experiment is relatively small compared to the diamagnetic cavity ($\delta B_{cavity} \sim -0.9 \times B_0$), the pressure gradient driven electric fields are predominantly in the wake of the fastest LPP ions and the force directs ions inwards in the direction of the diamagnetic cavity. From this it is observed that the magnetic pressure is primarily directed in the $+\hat{y}$ direction along the bottom of the cavity and the $-\hat{y}$ direction along the top of the cavity. Since a derivative is calculated across a discontinuity when stitching the planes together, there is some non-physical behavior along the stitched line that can be ignored.

With this continued expansion of the LPP the density decreases in inverse proportion to the time cubed ($n_{lpp} \propto t^{-3}$). This decreases the transverse ram pressure to the point where the magnetic pressure term stagnates the expansion along the y direction and redirects the plasma flow back towards the x-axis. A simple cartoon displaying this effect is shown in fig. 5.11. The ballistic zone refers to the region where LPP ions are expanding into the diamagnetic cavity and their motion is unaffected by the negligibly small magnetic field. The ion velocities observed in figure 5.4 (a-d) represents the motion in the ballistic zone.

The convergence zone is where LPP ions are expanding across the magnetic field gradient along the cavity edge. The ion motion is significantly affected by the non-zero magnetic field and the pressure gradient electric fields. The electric fields will redirect the ions back towards the blow-off axis. If the flow is sufficiently redirected it will converge into a high density jet-like structure at the leading edge. The additional features observed at the edge of the diamagnetic cavity in figure 5.12 show ions in the convergence zone. The transverse velocity maps visualize how the transverse flow is restricted from 100 ns and 300 ns (fig. 5.10). The spread in velocity space is reduced from $v_y(100\ ns) = [-107, 51]$ km/s to $v_y(300\ ns) = [-54, 0]$ km/s primarily in the convergence zone. At this time (300 ns) the jet has not yet formed.

The addition of an ambient plasma steepens the magnetic ramp, which is the region where the magnetic field "ramps" up from fully expelled to peak compression. An example of the enhancement is shown in figure 5.5 (d) and (e). In (d) the magnetic ramp is approximately $\delta B$ = 650 G over x = 7.5 − 10.5 cm, or roughly $\delta B/\delta x$ = 220 G/cm. The expansion into a magnetized vacuum (e) the magnetic ramp is greatly reduced to $\delta B/\delta x$ = 100 G/cm. Since the calculated $E_{press}$ (orange lines in (d) and (e)) is proportional to $\delta B^2/\delta x$, the LPP expansion into plasma experiences over twice the focusing effect compared to vacuum. Revisiting the imaging on the late-time (500 ns) expansion confirms the impact of the ambient plasma (5.6 (b)) on the collimation compared to expansion in vacuum (5.6 (a)).

If the curvature in polarization electric fields across the cavity was the dominant focusing mechanism, there would be no difference between the expansion into plasma compared to vacuum as this large scale polarization is due to the interaction with the magnetic field [16, 82]. The key assumption that leads to a curvature in the polarization fields is from the lack of magnetic field perturbation (low $\beta_k$). This allows for a simplified version of Faraday's law in which $\nabla \times E = \frac{-1}{c}\frac{dB}{dt} = 0$. This is not a valid approximation in the diamagnetic cavity edge in this experiment. Outside of the main diamagnetic cavity these large polarization fields have been measured [13].

This focusing results in the highly anisotropic expansion of the cavity which is evident in the shape of the 500 ns data in both figures 5.7 and 5.8. The "tear-drop" like shape is a result of the magnetic pressure term directed along the y-axis along with a time varying E × B drift as is discussed below. Similar effects have been observed in experiments studying sub-Alfvénic expansion [88] as well as expansion into vacuum [70, 61], and have been discussed theoretically [4, 79].

The LPP continues to self-focus until a jet is formed at the leading edge. From the arguments given thus far the jet would be expected to be formed on axis, since the transverse magnetic pressure would be expected to be symmetric across the blow-odd axis. The self-emission images in fig 5.7 (c) and 2D magnetic field data in fig. 5.8 show that the jet converges repeatably off axis in the +y direction. This corresponds to the electron gyro-direction.

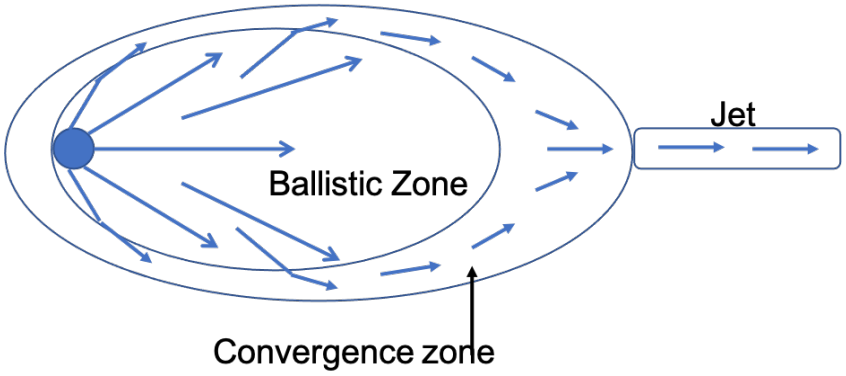


Figure 5.11: Illustration adopted from Frank et al. 1996 showing the convergence of the plasma flow transverse to the primary direction of travel. This flow "refracts" due to the interaction with the magnetic fields and ambient plasma and sets up a jet-like structure at the leading edge of the LPP. The convergence zone represents the region in which the magnetic pressure term is large and redirects the LPP flow. The ballistic zone is the region of expelled magnetic field where the ions travel ballistically. The jet is a result of the convergence region where ions pile up into a high density at the leading edge of the diamagnetic cavity.

Consistent with the findings of the sub-Alfvénic experiment, the leading edge ions experience a large deceleration due to the magnetic pressure gradients. This is evident in the deceleration of the leading edge ions from t = 100 ns (figure 5.9) where ions are moving upwards of $v_x = 315$ km/s to t = 300 ns (figure 5.12) where ions are observed to move at velocities as slow as $v_x = 50$ km/s. This deceleration would require a radially inward directed electric field of magnitude $E_r = \frac{m}{q}\frac{\Delta v}{\Delta t} = 400$ V/cm. This is consistent with the calculated fields in figure 5.5 (d).

The ions slow rapidly due to the presence of this electric field which has been measured in prior experiments [13, 28]. These slow moving ions have a small directed gyroradius ($\rho_i < 1$ cm) which allows for the ions to drift along the cavity edge in the azimuthal direction. Prior experiments have attributed a similar drift to the E × B drift of the entire LPP mass [61, 88, 26], the present case is a more localized effect as the drift can only affect particles along the diamagnetic cavity edge that have met two criteria: sufficient deceleration for $\rho_i < 1$ cm, but still in the presence of a magnetic field. As the magnitude and direction of the E × B drift and ∇B drift are similar, either of these could play a role in the motion along the cavity edge.

This will guide the ions in the azimuthal direction, or counter-clockwise in the data shown ($+\hat{y}$ on

the x-axis, $+\hat{x}$ on the bottom of the cavity edge, and $-\hat{x}$ on the top of the cavity edge). The effects of the drift can be observed in figure 5.12 which shows the x-directed velocity bins of the $C^{4+}$ ions. The ions in the convergence zone on the top side of the cavity experience a deceleration, which is evident in the ions with a low velocity existing further out in space. In the region of the 52 km/s bin at x = 8 − 10 cm and y = 0 − 2.5 cm there is a large signal. Ions traveling ballistically at 50 km/s would reach a distance around 1.5 cm by this time.

The reciprocal net positive drift along the bottom of the convergence zone is more visible at higher velocity bins. The velocity map representing the 157 km/s bin, for example, displays a large signal along the bottom edge of the cavity far behind the signal along the top edge of the plasma. If the LPP was allowed to expand freely into an unmagnetized vacuum, the expansion would be purely symmetric about the x-axis (see figure 3.8). However, since the ions along the top are decelerated and the ions along the bottom are accelerated in the convergence zone there is a large difference in the spatial position of the two signals.

This drift results in the self-collimation of the LPP off axis by y = 1.3 cm at 500 ns as displayed in figure 5.6 (b). Although the bulk features of the drift along the edge is observed here, the interface of the LPP and magnetized ambient plasma is host to a number of instabilities that is believed to lead to the spiky nature observed along the edge [23].

The x-directed velocity LIF maps at this time (550 ns) are displayed in figure 5.13. Below the velocity maps is the 2D magnetic field at the same time. The black dotted line overlayed onto all of the plots at the same point shows the very tip of the diamagnetic cavity. As will be shown in the following section, this feature detaches from the main cavity and maintain a region of expelled magnetic field that extends outward from the cavity, similar to a filaments observed in the Starfish* high-altitude nuclear test (HANEs) [94].

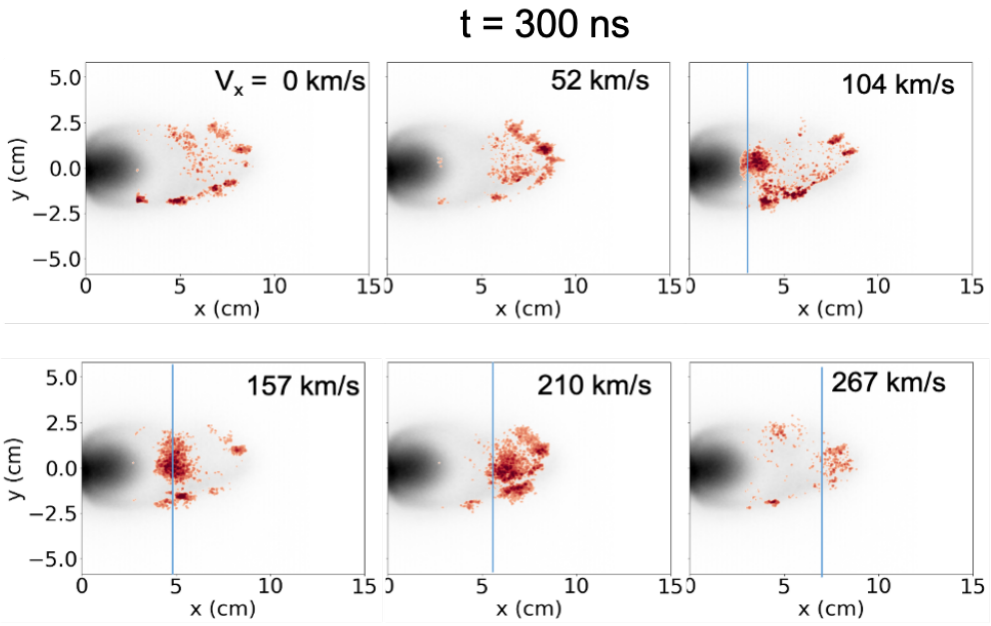


Figure 5.12: Images of fluorescing $C^{4+}$ ions at 300 ns at six different x-velocity bins. The effects of the $v_{pol}$ velocity shear along the edge of the cavity is evident in the discrepancy of the velocities measured on the top and bottom of the cavity. Velocities lower than 0 km/s and higher than 267 km/s bin were within the noise and therefore are not displayed here. Ions in the ballistic zone have an "x" over the top of them, and are identified as streaming within the diamagnetic cavity. The blue lines overlayed onto the images represent the expected time of flight distance for ions traveling at this velocity.

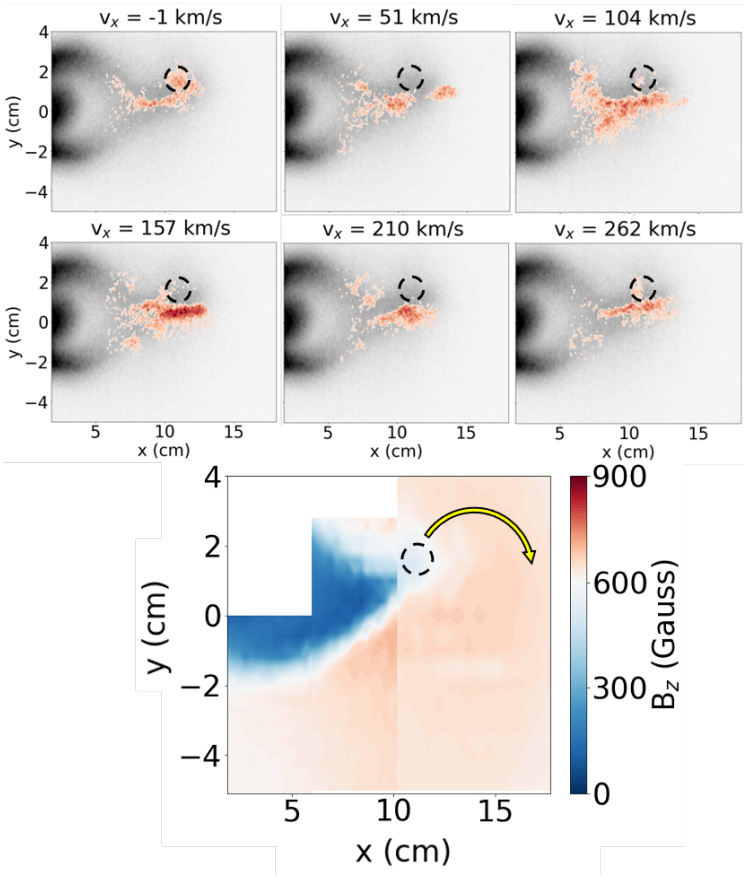


Figure 5.13: Fluorescence images of $C^{4+}$ ions at 550 ns at six velocity bins are displayed over the greyscale self-emission images of the LPP. On the bottom a contour plot of $B_z$ at the same time is shown when the blob is first separating from the diamagnetic cavity. The region where the blob is separating is represented by a black dotted line on the magnetic field plot as well as the LIF images. The bulk LPP flow is directly below the formation of the blob, which suggests the blob is formed from the cross-field ion currents.

### 5.3.3 Laser Produced Plasma Jetting Forms Plasma Blob

The focusing of the LPP maintains higher densities later in time and space than a free expansion. This high density flow is propelled into a region of magnetic field. This large, cross-field ion current density mediates the Larmor electric fields to develop ($\mathbf{E} \propto -n_i q_i \mathbf{v} \times \mathbf{B}$) in the y-direction acting on the LPP and ambient ions alike. These fields counter-balance the Lorentz force on the LPP ions and prevent gyration, whereas the ambient ions accelerate upwards and move according to the Lorentz force equation

$$\frac{d^2\mathbf{r}(t)}{dt^2} = \frac{d\mathbf{v}(t)}{dt} = \frac{e}{m_{He}}\left(\mathbf{E}(\mathbf{r},t) + \frac{\mathbf{v}(t)}{c} \times \mathbf{B}(\mathbf{r},t)\right). \tag{5.2}$$

As the ambient ion velocities are initially quite small, the equation of motion is dominated by the force due to the Larmor generated electric fields. The ambient ions are initially directed parallel to the electric fields ($+\hat{y}$) and then begin to gyrate. Since the LPP ions are primarily directed along the x-axis the difference in trajectory of the LPP ions and gyrating ambient ion separates them by upwards of the directed ambient ion gyroradius $\rho_{He^+} = \mathrm{v}_{He^+}/\Omega_{He^+}$, where $\mathrm{v}_{He^+}$ is the directed velocity and $\Omega_{He^+}$ is the ion cyclotron frequency for helium ions. This effect is displayed in the illustration in figure 5.1 at $\mathrm{t}_3$. The ambient electrons have a smaller directed gyroradius and so their motion to a good approximation can be is treated as directed radially outward according to the E $\times$ B drift with the externally applied magnetic field. The difference in motion between the two ambient species creates a region of charge separation that establishes an electric field directed downward. The combination of the Larmor and charge separation electric field sources enables a current which expels the magnetic field between the two flows as seen in figure 5.1.

To visualize this, figure 5.13 shows the 2D magnetic field map where there is first evidence of the blob compared to the velocity maps of the LPP. A black dashed circle highlights the region where this blob originates with a yellow arrow indicating its approximate future trajectory. Black dashed circles are over-plotted onto the LPP velocity maps in same location where the blob forms to allow

for an easier comparison between the two measurements. The predominant LPP flow is directly below the blob by this time, consistent with the blob being driven by Larmor electric fields.

The dynamics of the blob are shown in fig 5.14 where 2D bdot traces are displayed at ten separate times spanning form 500 – 700 on the first column and 750 – 950 ns on the third column. Each of these 2D traces are accompanied by y-lineouts of $B_z$ at five positions along the x-axis for easier visualization of the blob cross-section. The five lineouts are represented by the black dashed lines overplotted onto the 2D traces. The traces start before the blob has detached from the cavity. At times before 650 ns the characteristics of a standard diamagnetic cavity are observed, with the cavity strength decreasing with increased distance form the target. By 750 ns, the blob detaches from the cavity and the tip returns towards the blow-off axis. In the lineout at x = 12.7 cm, the blob expulsion is $\Delta B$ = 100 G which is 60 Gauss more expelled than the field at x = 10.7 cm. This pocket of expelled magnetic field that separates from the cavity must be maintained by a diamagnetic current structure flowing in a counter-clockwise sense. The blob is centered at (x,y) = (12.7 cm, 1.8 cm) and has a physical size of 3.2 cm in the direction of travel and 1.8 cm in the transverse direction, which is displayed in figure 5.15 (c). The amount of energy within the 2D slice of the blob is calculated to be 35 $\mu$J/cm from $\frac{B^2}{8\pi} \times A_{blob}$.

It is useful to check that such an ion current could expel this amount of magnetic field. Assuming that the ions are approximated by a wire, the amount of current necessary to expel 100 Gauss at a radius of 1 cm is 500 A (from B = $\frac{\mu_0 I}{2\pi r}$). An estimated density can be calculated from I = $q_i n_i v_i A_i$, where $q_i$, $n_i$, $v_i$, and $A_i$ are the ion charge, density, velocity, and cross section area. This leads to an approximated density of $5 \times 10^{13}$ cm$^{-3}$ for the LPP ions at 550 ns. Scaling laws [78] estimate the number of laser ablated ions as $2 \times 10^{16}$, which nearly half of should be $C^{4+}$ at these conditions. The shape of the LPP can be approximated as an oblate spheroid with a semi-major axis of 5 cm and semi-minor axis of 2 cm to first order. This equates to a volume of 210 cm$^3$, and thus an ion number density of $4.7 \times 10^{13}$ cm$^{-3}$. The agreement of this simplified model give confidence to the notion of the LPP ion currents creating the blob. This model would suggest an equivalent

magnetic compression along the bottom of the ion current, which is observed in the lineouts at x = 10.7 cm at 500 ns in figure 5.14. This phenomena is short lived compared to the blob, as the blob is maintained by the charge separation electric fields along the top edge, whereas the compression is not maintained once the ion currents dissipate.

The blob then begins to dissipate and moves closer to the x-axis. By t = 1200 ns the center of the blob displaced from the target by 16 cm where the maximum diamagnetic cavity extent is x = 10 cm. This is easier to observe in the lineouts present in figure 5.5 (g) highlighted with a black dashed line. The blob expulsion magnitude has dropped from 100 to 40 Gauss by this time. The 1D lineout in figure 5.5 provides better spatial resolution for observing the blob than the 2D traces in figure 5.15.

One prior experiment that observed this type of converging flow [70] did not report the formation of this additional magnetic structure in the experimental data, even though a similar feature appeared in the ideal MHD simulations. The structure is forming in the ambient particles and therefore was not observed in the prior experiments as it was performed in vacuum.

The blob is formed between the two ion flows, the LPP along the bottom and the E $\times$ B drifting helium ions [9, 13]. In order to observe the reaction of the helium ions as the LPP transfers energy, the plasma was imaged through a 10 nm bandpass filter, centered around the 468.6 nm $He^+$ self-emission line. These images are integrated along the line of sight. As discussed in chapter 2, the emission of this spectral line is only visible on the nanosecond timescale if the ambient ions are in contact with energetic electrons. The emission is from a transition the n = 4 to n = 3 quantum state and repopulation of the n = 4 state from the ground state requires collisional excitation by an electron with energy > 51 eV. Therefore, only a small subset of the ambient ion reaction is observed due to the cross field ion current.

Another difficulty in this measurement is that there exists a $C^{2+}$ self-emission line at 467.3 nm. This is within the FWHM of the bandpass filter used to image the helium and at an intensity greater than

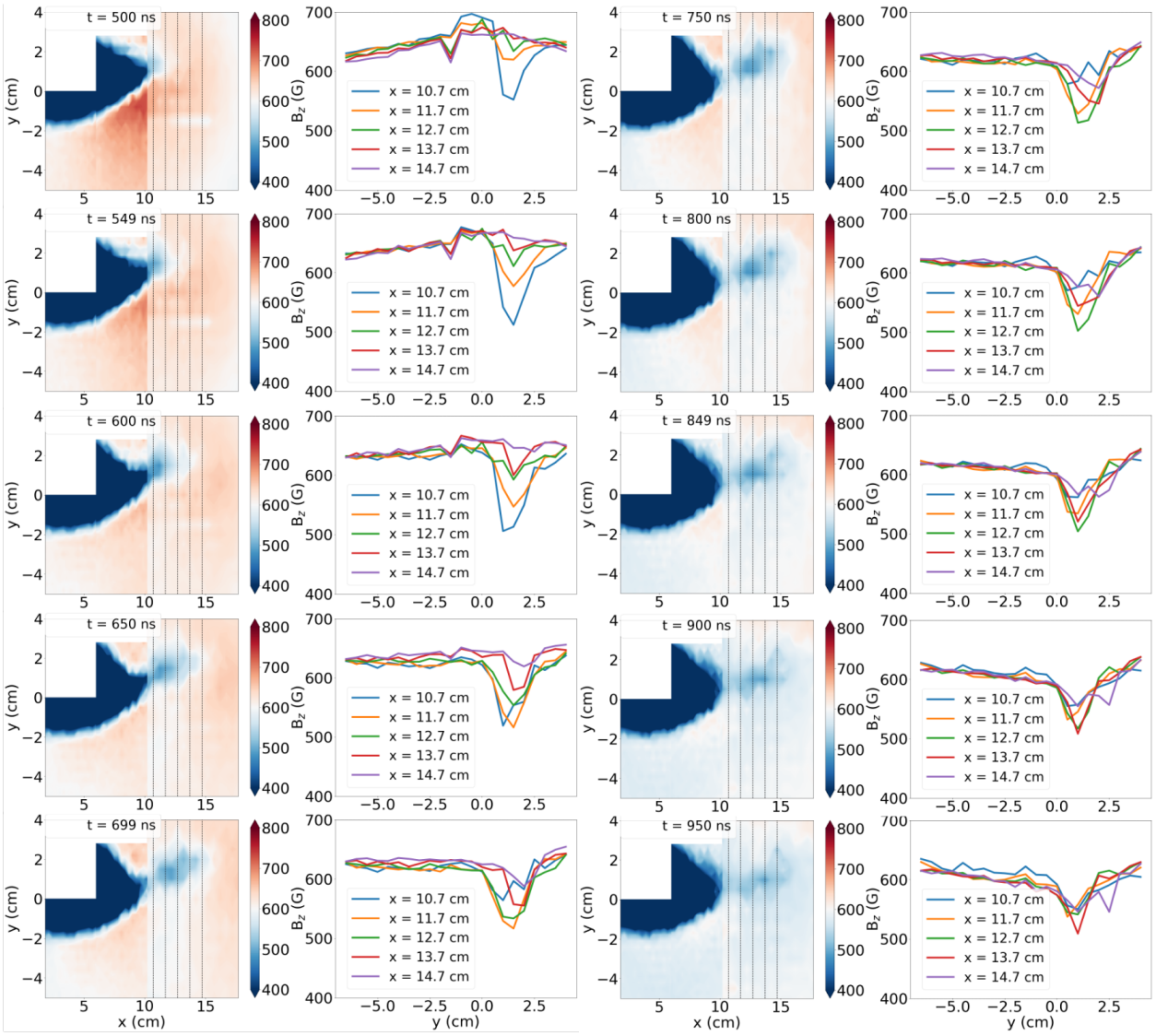


Figure 5.14: The evolution of the blob from inception to dissipation are represented. At each time from 500 – 950 ns, a 2D magnetic field trace on the left hand side and y-lineouts at 5 different x position on the right hand side are shown. These x positions are represented by the black dashed lines over the 2D traces. Before the blob detaches from the diamagnetic cavity, the y-lineouts show that the magnetic expulsion decreases with increasing distance from the target. After the blob detaches around 700 ns, there is a distinct gap between the diamagnetic cavity and the blob where the magnetic field is 60 Gauss less expelled than the blob. The peak expulsion of the blob is $\Delta B$ = 100 Gauss at 800 ns.

the helium line. While this does limit this measurement, with basic arguments about the spatial location and direction of travel of the $C^{2+}$ ions, the reaction of the helium ions can still be observed.

The ions species in the LPP should have velocities related to the respective charge-to-mass ratios, giving $C^{2+}$ roughly half the initial velocity of the $C^{4+}$ ions. Overlayed on top of the helium emission images in fig. 5.15 are red dotted lines that represent the furthest spatial location $C^{2+}$ would be expected to have expanded. Any signal beyond this point is assumed to be emitted by the intensified helium ions. A secondary identification method is the direction of travel. As the $C^{2+}$ ions should be directed primarily along the x-axis, the features that move along the y-axis in accordance with the Larmor coupling term is assumed to be helium ions.

Based on these arguments, the $He^{+}$ reaction to the LPP is observed in the filtered images. In figure 5.15 the magnetic field traces and filtered He ion images at three different times (500, 750, and 1000 ns respectively) are shown. A red arrow in figure 5.15 (b), (d), and (f) identifies the spatial location of helium ions that are accelerated by these Larmor fields.

In the first row at t = 550 ns, the Larmor electric fields have just begun and so the helium ions have not separated from the electrons and formed the detached blob.

The second row (t = 750 ns) depicts when the blob detaches from the main diamagnetic cavity and the tip of the cavity returns back down to the axis. A region of 580 Gauss that has separated from the main cavity has been highlighted in black and represents the blob. From the helium emission, it is shown that ambient ions have primarily moved upwards in the y-direction, and slightly forward in the x-direction, consistent with the $E \times B$ drift driven by the Lorentz equation 5.2 for early times.

The helium emission that is identified by the red arrow is notably above the blob. This helps to support the origin of the blob as electron population trapped between two oppositely directed electric fields. One along the bottom of the blob directed in the $+\hat{y}$ direction due to the LPP cross-field currents (induced electric fields). The other along the top of the blob directed in the $-\hat{y}$ direction from the transient charge separation from the difference in gyroradii of the ambient

ions and electrons as they E × B drift (electrostatic fields). This drives a current similar to the diamagnetic current which expels the ambient magnetic field in this blob. The reason the magnetic compression below the ion current dissipates much faster than this blob is the lack of electrostatic field maintaining the feature.

Finally, at 1000 ns, along the bottom row the blob is directed toward the x-axis and dissipates. The helium ions have decoupled from the LPP by this time. These blob structures have been observed in earths atmosphere after Starfish* events [94] and have been measured to considerably elongate along the field axis. A direct correlation can be drawn between the lifetime of these blobs and the length along the field axis as energy is transported out of the system. In this experiment, data was collected in two dimensions and therefore the full 3D structure of the filament is not clear. However, prior experiments done on the LAPD by Gekelman et al. [37] have shown large coherent current channels that exist perpendicular to the LPP flow in agreement with this blob, as well as the corresponding density increase. These experiments did not reach currents as large as predicted here. A characteristic that defines these blobs is a singly-peaked density distribution with a peak value much higher than the surrounding root mean squared fluctuations of the ambient density [27]. These are associated with changes to the magnetic field similar to those observed here. The densities were not able to be measured in these experiments and only magnetic field data can be compared.

In the duration that the motion of ambient ions is observed as a direct reaction of the LPP driver, the species moves further in the y-direction than the x-direction. This is understood through the equation of decoupling, presented by Hewett et al. [46]. It was previously shown that if $\alpha = \pi Z_d n_d / 2(Z_d n_d + Z_a n_a)$ meets the condition $\Omega_c t_d < \alpha < 1$ the ambient ions rapidly decouple from the driver plasma. The left-hand limit of the equation is known as the finite pulse duration limit, and is understood as the ambient ions not being sufficiently magnetized within the finite pulse width of the LPP driver. The ambient ions are accelerated along y, increasing the gyro-radius. However, by the time they complete one quarter of a gyro-period and direct the velocity to the

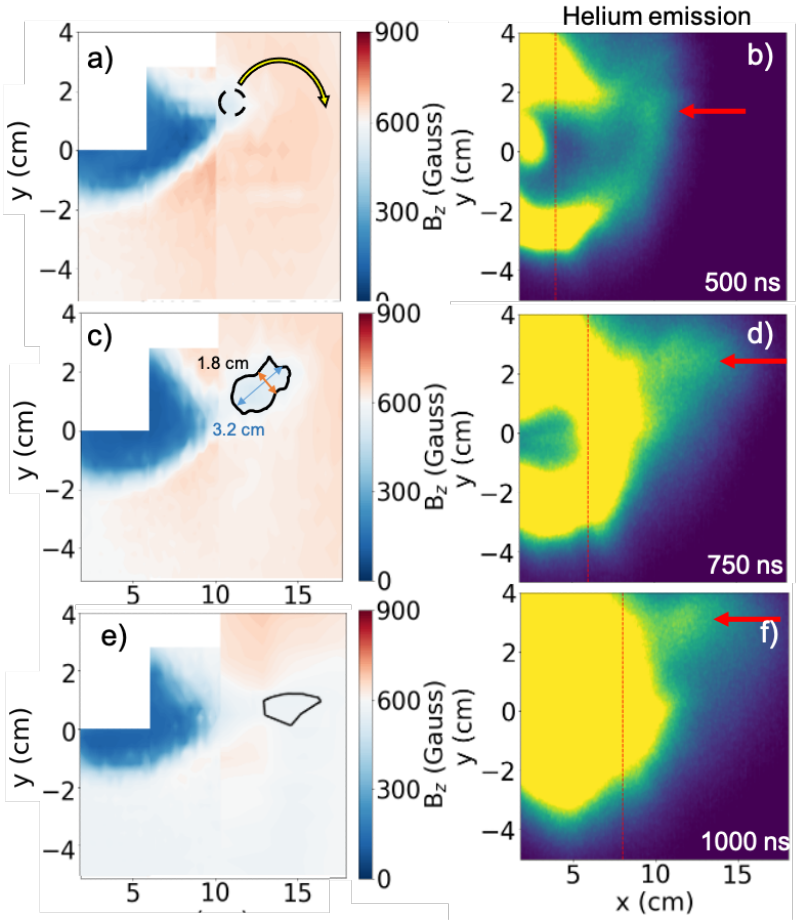


Figure 5.15: (a-c) show 2D bdot planes at 550, 750, and 1000 ns. The region of ~ 580 G that is separated from the main cavity is represented by the black dotted line in order to highlight the blob region. (d-e) show the unfiltered LPP images at the corresponding times with the region of the blob highlighted. At 1000 ns the far out regions are outside of the visible range due to the intense light near the target. (f-i) show the images with the helium filter placed in front of the camera. While there is intense light from $C^{2+}$ light, a convincing signal is generated from intensified helium near the blob.

x-direction, the driver plasma has expanded well past and no longer are able to couple to the plasma. This decoupling could be alleviated by using a hydrogen ambient plasma, or by increasing the magnetic field. Since the electric field maintaining the blob has weakened, the blob dissipates.

Thus far simulations have been able to replicate some of the major features in this experiment (blob detaching from cavity and drift). Fine adjustments are still being made to ensure sufficient agreement between experimental and simulated data.

### 5.3.4 Comparison to Expansion in Vacuum

In order to verify that this blob structure is developed due to the presence of the ambient plasma, it is useful to return to the comparison between the LPP expanding into the magnetized ambient plasma to expansion into a vacuum with magnetic field as seen in figure 5.5. Comparing the blob developed in the ambient plasma to vacuum is limited since the motion of the blob is off-axis, and the only data collected without an ambient plasma was a lineout along the x-axis. In fig. 5.5 the difference between plots (a) and (b) are plotted in (c) to detail the difference that ambient plasma has on the magnetic traces. Blow each of the streak plots, an x-lineout at times corresponding to 500 and 1200 ns specified on the left most plot for each row. A line is overplotted onto the streak plots to show where the lineouts correspond to the 2D data. The electric field due to the magnetic pressure is calculated and plotted alongside the magnetic field traces. Only the x-component of $E_{press}$ can be calculated in this lineout since the only spatial parameter varied is x.

From the 500 ns data (the second row) the calculated electric field that leads to both the self-focusing mechanism, as well as the polarization drift, is greatly reduced from the expansion into plasma (d) to the expansion into vacuum (e). While no 2D data of the vacuum shot was measured to corroborate that the dynamics are affected, it stands to reason that the reduced electric fields along the x-axis is representative of an overall reduce electric field along the exterior of the diamagnetic cavity. This would result in less collimated flow and therefore no jetting or blob.

As displayed in the 2D bdot data, the blob gyrates down to the x-axis by approximately 1200 ns,

and although the extent of the expulsion has been reduced, the effects are seen in the lineouts in (g), (h) and (i). When there is no ambient plasma to interact with (b, e and h), the blob does not develop and the field simply returns to the ambient field after the magnetic compression passes. Whereas (g) and (i) show that an additional magnetic expulsion exists further out in space than the diamagnetic cavity corresponding to the blob.

## 5.4 Summary

The main discovery in this experiments was the creation of an additional magnetic structure - or blob - created in the ambient plasma that extends well past the diamagnetic cavity. 2D mapping of a super-Alfvénic LPP expanding quasi-perpendicularly into a magnetized ambient plasma allowed for the origins of blob to be explored. This experiment built off of the previous experimental findings that have shown the effect of the magnetic structure term which dominates in sub-Alfvénic expansion. While the dominant component of coupling in super-Alfvénic flow is the cross-field ion current term, the magnetic structure term still plays an important role in the dynamics in the low Mach number ($M_A \sim 2$) case. We investigate the dynamics through the combination of magnetic field measurements, spatially and temporally resolved ion velocity maps, and wavelength filtered imaging. The investigation has yielded the following results:

The dynamics are understood through the combined utilization of magnetic flux probes, wavelength-filtered imaging, and the laser induced fluorescence diagnostic and have yielded the following results:

- The effects of the increased coupling to the ambient plasma were observed, as is expected from the energy balance equation. The diamagnetic cavity size is greatly reduced when the LPP expands into a magnetized plasma as opposed to a magnetized vacuum. This gives additional confidence that the plasma density is high enough that the LPP is in the super-Alfvénic regime.

- The measured magnetic fields allow the calculation of the electric fields along the diamagnetic cavity edge that lead to a self-focusing force which allows a jet-like structure to emerge at the leading edge of the LPP flow. LPP self-emission images are in good agreement with the self focusing and agree well with the calculated magnitude of electric field strength.

- The restrictive force along the edge of the cavity that focuses the LPP and which acts perpendicularly to the externally applied magnetic field leads to an inertial polarization drift. This polarization drift is sufficiently strong to significantly affect the trajectories of ions within a gyroperiod. This causes the gyration of the tip of the diamagnetic cavity in the electron gyro-direction and are observed in the LIF maps as slowing the ions along the top side of the cavity edge and accelerating ions along the bottom edge.

- The jetting of the LPP flow increases the density of the LPP ions in a region where ions are crossing field lines. This ion current in a non-field free region allows Larmor coupling to impart energy from the LPP to the ambient plasma directly instead of using the magnetic fields as an intermediary in the process. This electric field is directed in such a way so as to cause an $E \times B$ drift of the ambient ions and electrons. Using wavelength filtered imaging the reaction of the helium ions to the LPP are observed to move according to the Larmor term which is directed perpendicular to the LPP ion current and B field. The ions are not well magnetized and so shortly after acceleration, they decouple from the LPP plasma.

- A blob is observed in the magnetic field traces where a region of expelled magnetic field that extends well past and separates from the main diamagnetic cavity in what is referred to as a blob. This blob structure is generated in the region where the Larmor fields originate, but does not extend quite so high as the observed helium ions. This giving confidence that the blob is a region of electrons trapped between the LPP and helium ions that then diffuses along the field lines. The blob gyrates back towards the x-axis after a short (few 100's of ns) time. This blob is a result of the coupling to the ambient plasma and is not observed when the plasma expands into vacuum.

# CHAPTER 6

# Conclusions

## 6.1 Summary of Main Results

The primary results of this work can be divided into two components: the observation of a blob structure developing in the interaction of a hot, transient plasma with the ambient magnetized plasma of the LAPD and the implementation of a laser induced fluorescence (LIF) diagnostic capable of measuring the hot, transient plasma.

The results will be divided into two sections based on the experiments performed. The first discusses the creation of a blob in the ambient plasma. The second discusses the development of the LIF diagnostic on a sub-Alfvénic laser produced plasma (LPP).

### 6.1.1 Super-Alfvénic Expansion

- A blob, or region of expelled magnetic field that extends well past and separates from the main diamagnetic cavity is observed. This blob structure is generated in the region where the Larmor (induced electric) fields originate and extends between the streaming LPP ions and the accelerated ambient helium ions. This gives confidence that the blob is a region of electrons trapped between the LPP and helium ions that then diffuses along the field lines. This blob is a result of the coupling to the ambient plasma and is not observed when the plasma expands into vacuum.

- The results of increased coupling to the ambient magnetized plasma are observed. The diamagnetic cavity volume is reduced when the LPP expands into a magnetized helium plasma as opposed to a magnetized vacuum. The discrepancy in size is not equivalent in all dimensions, with the cavity length remaining more similar along the blow-off axis than transverse to the blow-off axis.

- The magnetic pressure gradient generated electric fields at the diamagnetic cavity edge mediate the focusing of the LPP flow into a jet-like structure at the leading edge. This is different from prior experiments where the LPP focused due to a curvature in the polarization electric fields. LPP self-emission images are in good agreement with the self focusing and demonstrate that the effect is not present in the expansion into magnetized vacuum. The calculated magnitude of electric field strength agrees with the focusing mechanism.

- The jetting of the LPP flow increases the density of the LPP ions in a region where ions are crossing field lines. This ion current in a non-field free region allows Larmor coupling to impart energy from the LPP to the ambient plasma directly instead of using the magnetic fields as an intermediary in the process. This electric field is directed in such a way so as to induce an E $\times$ B drift of the ambient ions and electrons. Using wavelength filtered imaging the response of the helium ions to the LPP are observed to move according to the Larmor term which is directed perpendicular to the LPP ion current and B field. The ions are not well magnetized and so shortly after acceleration, they decouple from the LPP plasma.

### 6.1.2 Sub-Alfvénic Expansion

- The first laser induced fluorescence measurements on an explosive, $C^{4+}$ laser produced plasma (LPP) as it expands into a preformed magnetized plasma were conducted. These allowed for the LPP ion velocity distributions to be measured with high spatial and temporal resolution, revealing ion deceleration in regions of high magnetic pressure gradients, consistent with coupling dominated by the magnetic structure term.

- The measured ion velocities at early times allowed for an improved initialization of three-dimensional particle-in-cell simulations that well represent the interaction. Through matching the ion velocities and diamagnetic cavity shape and expansion time, these simulations allowed for the unmeasured quantities such as the total electric field and ambient ion reaction to be understood.

- The combination of the novel measurement of ion velocity maps and simulations allows for an understanding of electric fields created from laminar collisionless coupling that accelerate the ambient helium ions. The energy from the LPP is observed to transfer to the magnetic field and then to the ambient ions as is expected in the sub-Alfvénic regime.

## 6.2 Future Work

Structures similar to this blob feature have been observed in the AMPTE and Starfish* experiments that transport energy across field lines. These features have been observed to have an increased extent along the magnetic field axis, be associated with increased densities, and are characterized by quantities that deviate significantly from Gaussian statistics. The exploration of blobs in LPP experiments is relatively new and not thoroughly explored, as the geometry of this experiment was 2D. As a future direction, we could explore the spatial extent along the field axis, and try to measure the increased density profile in the blob to understand how energy is transported along field-lines.

In the current setup, the LIF diagnostic requires averaging approximately 20 laser shots to collect one data point. This is due to the necessity of subtracting background shots from the signal shots to distill the actual signal. An improvement to the LIF diagnostic would allow for the collection of signal in one ablation laser shot by using two cameras to observe the interaction region. One camera would image the background a few ns before the LIF probe beam resonates with the LPP, then an image would be acquired by a second camera to gather the signal and background. Assuming that the dynamics of interest have not appreciably changed over a few ns, this would allow us to observe non-repeatable phenomena such as instabilities, as well as field this diagnostic on slower repetition

rate lasers.

Recent experiment have demonstrated improved control over the LAPD plasma conditions, resulting in a factor of two increase in the helium density by conservative estimates. This increased density will lower the Alfvén speed and extend this experiment further into the super-Alfvénic regime dominated by Larmor coupling. If the same scaling of density applies to the hydrogen plasma, the increase magnetization of the ambient plasma will extend the coupling between the LPP and ambient plasma, while maintaining a super-Alfvénic expansion.

# APPENDIX A

# Measurements of Ion Velocity Distributions in a Large Scale Laser-Produced Plasma

## A.1 Introduction

Creation of a hot expanding plasma by laser ablation of a solid target is ubiquitous in laboratory astrophysics. The interaction of a laser-produced plasma (LPP) expanding into an ambient magnetized plasma is important in cases as diverse as the study of diamagnetic cavity formation[9], anomalous magnetic diffusion[26], plasma instability growth[43], and collisionless shock formation[64]. These systems are often hotter ($T_e \gtrsim 10$ eV) and denser ($n_e \gtrsim 10^{13}$ cm$^{-3}$) than those probed by traditional diagnostics (e.g. magnetic flux probes, Langmuir Probes, etc.), which also inherently disrupt the plasma during measurement. LPP experiments must instead rely on non-invasive diagnostics when traditional diagnostics would overly disrupt the dynamics or when the plasma is too hot/dense to permit physical probes.

In this paper, the design and assembly of a time-resolved monochromator to diagnose ion velocity distributions is discussed. We present results of time-of-flight (ToF) ion measurements from expanding laser plasmas. One distinguishing factor from conventional techniques (i.e. Langmuir probes, Thomson scattering) is the ability to separately diagnose different charge states within a composite plasma. By looking at self-emission spectral wavelengths for each of the species in our composite plasma, the velocity distributions and relative abundances of each ion species can be identified. This information is vital in order to further understand the creation and dynamics of the

laser-produced plasma.

## A.2 Experimental Setup

This diagnostic was developed for use as part of a series of experiments studying instabilities in ion beams streaming parallel to ambient magnetic fields[43, 45]. The LPP is created by focusing a high energy laser (1053 nm, 200 J, 25 ns FWHM) onto a high-density polyethylene ($C_2H_4$) target (Fig. A.1). The composition of the LPP is determined by the intensity of the ablation laser[78], which for this experiment went up to $I_o = 10^{13}$ W/cm$^2$. This laser is operated by the University of California, Los Angeles (UCLA) High Energy Density Plasma (HEDP) Phoenix Laser Laboratory[63]. Based on this intensity, the most dominant ion species, in both population and total kinetic energy density[78], is $C^{4+}$. The resulting plasma expands though the ambient helium plasma of the Large Plasma Device (LAPD) at UCLA[36].

The LAPD consists of two cathodes (BaO and $LaB_6$) on either end of a 20 m, long 1 m diameter vacuum chamber that is capable of creating a quiescent and highly reproducible, steady-state ($\sim$ 15 ms), magnetized plasma at repetition rates up to 1 Hz. The LAPD can create a plasma up to electron density $n_e \sim 10^{13}$ cm$^{-3}$, electron temperature $T_e \sim 5 - 10$ eV, and ion temperature $T_i \sim 1$ eV.

The initially dense LPP ($n_i \sim 1.5 \times 10^{17}$ cm$^{-3}$) rapidly expands causing the leading edge of the ablated ion plume to become quite tenuous[78] ($n_i \leq 5 \times 10^{11}$ cm$^{-3}$) by the time it reaches the first optical diagnostic window (viewing port) at z = 32.5 cm. Nevertheless, the monochromator diagnostic can detect particles greater than seven meters from the target where the longitudinal dispersion has caused the density to drop further[45]. Measurements can be made through viewing windows spaced every 32.5 cm along the LAPD.

The spontaneous emission lines of interest for this study (isolated from other lines by at least the instrument function $\Delta\lambda = 0.3$ nm, and not containing significant fine structure) exist in the UV

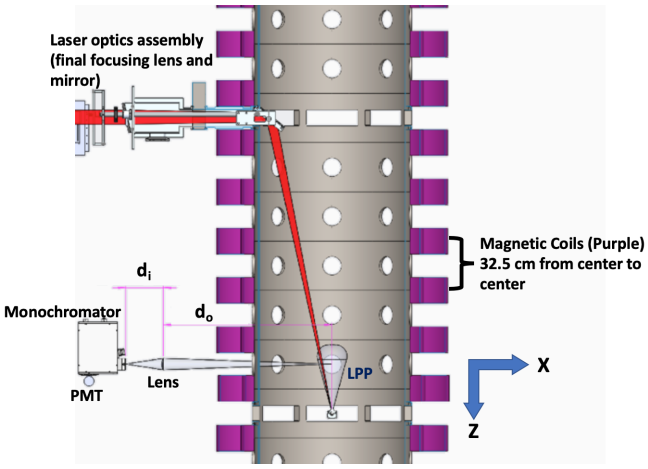


Figure A.1: Cross section of experimental setup in the LAPD. The diagnostic collects light from the center of the LPP plume ($d_o$ = 110.0 cm), and couples light to the monochromator through a convex lens. The light is wavelength filtered and collected by a PMT. The setup is placed at a distance of 32.5 cm along the blow-off axis ($-\hat{z}$ direction, anti-parallel to $B_0$) which is one of the viewing port locations where data can be collected.

range (225 – 245 nm). The $C^{4+}$ ion species was chosen for study based on experimental reasons, and of the observable self-emission lines, the 227.091 nm line was determined to be the brightest over a wide range of temperatures and densities. All measurements for these experiments were made through quartz windows, which were transparent down to ~ 150 nm.

## A.3 Design and assembly

The primary objective of this diagnostic is to measure the velocity of multiple concurrent charge states of fast ions. In our experiments, the ions are super-Alfvénic with speed $v/v_A > 1$, where $v_A = B/(4\pi m_i n_i)^{1/2}$ is the Alfvén speed, $B$ is the ambient magnetic field, $m_i$ is the ion mass, and $n_i$ is the number density of the ions. This requires the diagnostic to have a temporal resolution of much less than one inverse ion cyclotron frequency ($\omega_{c,i}^{-1} = m_i c/q_i B$), where $c$ is the speed of light, and $q_i$ is the ion charge, and spatial resolution less than one ion inertial length ($\delta_i = v_A \omega_{c,i}^{-1}$).

There are three critical components of the diagnostic: the collection optics, the monochromator as a light filter, and a light detector system. The collection lens combined with the monochromator sets the spatial resolution, whereas the light detector system determines the temporal response and

the light detection characteristics.

### A.3.1 Collection optics

Coupling of light emitted from the source to the detector is most easily understood by tracing rays from the detector aperture back through the monochromator and into the plasma. Light emitted by the ions is collected by a spherical plano-convex lens and imaged onto the monochromator entrance slit. All calculations are performed under the assumption of an ideal lens (i.e. minimum spherical aberrations) and an optically thin plasma (i.e. negligible photon-ion collisions).

In order to transmit the image plane unaffected (i.e. without loss of light or resolution) through the monochromator, the collection optics should be positioned to match the f-number ($N_f$) of the monochromator($N_{f,m}$). In other terms, $d_i = 2rN_{f,m}$ where $d_i$ is the distance between the lens and entrance slit of the monochromator, and $r$ is the radius of the lens as can be seen in Fig. 1. Using the thin lens equation, the resulting distance from the lens to the object plane is $d_o = (2frN_{f,m})/(2rN_{f,m} - f)$, where $f$ is the focal length of the collection optic(s).

The object distance is often set by experimental constraints. For instance, the closest a lens can physically be positioned to the axis of the LAPD chamber, while still being located outside of the chamber, is 0.5 m.

In the common case where the source of emission is spatially extended, characterizing the spatial resolution of the measurement system is necessary. This is especially crucial where there is spatial structure of interest. Conventionally a ray tracing algorithm would be used to calculate the collection volume of such a setup[34]. However, these can be cumbersome and computationally intensive. An alternative method has been utilized that is within 4% agreement of ray tracing algorithms[21].

The desired quantity is the collection efficiency ($\epsilon$) for an arbitrary point within the source for the optical system under consideration (Fig. 2):

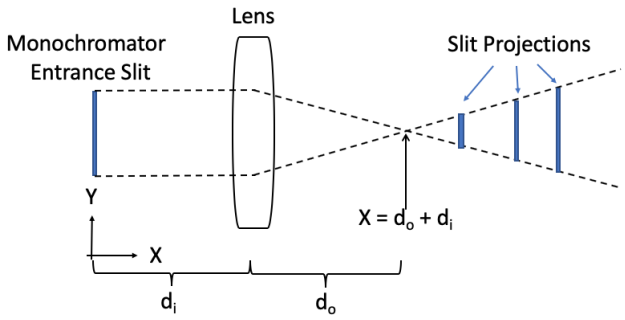


Figure A.2: Sample pattern of accepted rays from a source displaced transverse to the collection axis. The effective area used to calculate the coupling efficiency uses the image of the monochromator slit.

$$\epsilon(x) = \frac{A_l(x, y, z)}{4\pi(x - d_i)^2} \tag{A.1}$$

where $A_l(x, y, z)$ is the area defined by the accepted light rays from an arbitrary point in space for all values $x > d_i$ (the location of the lens) and $\epsilon(d_o + d_i) \equiv \epsilon_o = 1$ at best focus. The collection efficiency for points outside of best focus is determined by projecting an image of the monochromator entrance slit onto a plane transverse to the collection axis (Fig. 2). Utilizing this technique, the collection volume boundary is defined to be where $\epsilon = 1/e \approx 0.37$

For the setup used in experiments conducted on the LAPD, the light was collected through a 200 mm focal length lens to a 1/4 m Acton spectrometer (1200 grooves/mm grating blazed at 500 nm). The entrance slit was set to be 10 $\mu$m with a height of 4 mm. The resulting collection volume was determined to be 0.23 cm$^3$ along the line of sight, with a maximum cross section of 2.8 cm $\times$ 2.2 $\mu$m (corresponding to the height and width of the slit, respectively).

### A.3.2 Detector comparison

There are many important factors to weigh when deciding upon a light detector, including: temporal response, quantum efficiency, signal to noise, spectral range, and radiant flux being observed. The two metrics that most compactly encompass these quantities are the signal to noise ratio (S/N) and the equivalent noise input (ENI). The ENI (also known as noise equivalent power) is the minimum

input light flux at which you receive a S/N of unity for a detector. In comparing two commonly used light detectors - the avalanche photodiode (APD) and the photomultiplier tube (PMT) - it was determined that the PMT outperformed the APD under our experimental conditions.

The signal output by an APD is $I_s$ =M$R(\lambda)P_i$, where M is the gain, $R(\lambda)$ is the responsivity at a given wavelength ($\lambda$) and $P_i$ is the input power. Depending on the value of $P_i$, the detector noise will be dominated by either detector dark noise ($I_d$) at low levels, or photon shot noise at higher levels.

$$\frac{S}{N}_{APD} = \frac{MR(\lambda)P_i}{\sqrt{(2q\Delta B(I_d + R(\lambda)M^2P_iF))}} \tag{A.2}$$

The S/N is given by Eq. 2 where $q$ is the elementary charge, $\Delta B$ is the bandwidth, and $F$ is the excess noise factor, which describes the statistical noise due to multiplication process and is given by $F = Mk + (2 - 1/M)(1 - k)$, where k is the ionization rate ratio[52]. The minimum detectable optical power, $P_{min}$ can be calculated from setting Eqn. 2 equal to 1. This results in

$$P_{i,APD,min} = \frac{q\Delta BF}{R(\lambda)} + \frac{\sqrt{q^2\Delta B^2F^2 + 2q\Delta BI_dM^{-2}}}{R(\lambda)} \tag{A.3}$$

Since the dark current will dominate for low level light signals, this can be estimated as:

$$P_{i,APD,min} = \frac{\sqrt{2q\Delta BI_d}}{MR(\lambda)} \tag{A.4}$$

The S/N for the PMT case is given by Eqn. 5 where $S_p$ is the anode radiant sensitivity, $I_{da}$ is the anode dark current, and $\mu$ is the gain[38].

$$\frac{S}{N}_{PMT} = \frac{S_p P_i}{\sqrt{(2q\Delta B\mu F(S_p P_i + 2I_{da}))}} \tag{A.5}$$

Unlike the APD case where one term in the noise dominates over the other for low input power, both noise sources have to be taken into consideration when rearranging for $P_i, min$[38].

$$P_{i,PMT,min} = \frac{q\mu F\Delta B}{S_p} + \frac{\sqrt{(q\mu F\Delta B)^2 + 4qI_{da}\mu F\Delta B}}{S_p} \tag{A.6}$$

Where F and $S_p$ are highly wavelength dependent. Once a specific wavelength of interest has been chosen, the values for the majority of terms in equations 2 and 5 are determined. However, the PMT is designed to be able to have certain characteristics, namely bandwidth, changed by an external circuit. The bandwidth of this type of ciruit is given[52] by $\Delta B = 0.35/\tau_{RC} = 0.35/R_{tot}C_{tot}$, where $\tau_{RC}$ is the characteristic time of an RC circuit, $R_{tot}$ is the total resistance and $C_{tot}$ is the total capacitance.

Both the APD and PMT have a low output capacitance ($\sim$ 0.1 – 100 pF and $\sim$ 1 – 20 pF, respectively). Therefore, the total capacitance is dominated by the connecting BNC cable ($C_{BNC}$), which typically has a capacitance/length value in the 100 – 300 pF/m range.

A PMT has a series of smaller resisters that add up to have high terminal impedance ($\sim$ 300 kΩ). By impedance matching this to an external circuit (oscilloscope, data-acquisition-system, etc.) the $\tau_{RC}$ can be manipulated by adding a parallel shunt resistor. For instance: assuming the use of an oscilloscope that has 1 MΩ impedance capabilities, different shunt resistors can be placed in parallel so as to set the total resistance of the system. This combined with the $C_{BNC}$ will set the bandwidth, and therefore the S/N of the setup. Shunt resistors ranging from 500 Ω – 10 kΩ therefore result in an effective bandwidth of 23.33 MHz −1.2 MHz respectively.

In contrast, the terminal circuitry in an APD is an active low-pass filter with amplification. The

| | Hamamatsu S12053-10 (APD) | Hamamatsu R7518 (PMT) |
|---|---|---|
| $R(\lambda)$ *or* $S_p$ $(A/W)$ | 0.14 | $5.1x10^5$ |
| Gain (M or $\mu$) | 50 | $1.2x10^7$ |
| $I_D$ (nA) | 1.0 | 0.2 |
| F | 3 | 1 |
| $A_d$ $(mm^2)$ | 0.79 | 192 |
| S/N at 1 $\mu W$ | 3.8 | 237 |

Table A.1: Comparison of S/N of the Hamamatsu $S12035-10$ APD and $R7518$ PMT. The terminal resistor used to calculate is $1k\Omega$, giving a $\tau_{RC} = 36\ ns$. All values taken at 227.1 *nm* wavelength value.

output impedance is low ($\sim 50\ \Omega$) which does not offer the same adaptability to external circuitry as with high impedance. The output impedance dominates $\tau_{RC}$ and therefore the bandwidth is fixed.

This straight-forward adjustment to the bandwidth, and therefore the S/N, by changing out the shunt resistor is a desired quality of this diagnostic, which is satisfied by the PMT. This offers flexibility to configure the setup for varying levels of light detection. For laser experiments run on the LAPD, this flexibility allows for measuring a hot, dense plasma as well as a cold, tenuous plasma with minimal adjustments.

The final aspect to be weighed is the detector active area $A_d$. This is important to match to the image size at the detector in order to maximize the light that is being collected. Generally, $A_{d,PMT} > 100\ A_{d,APD}$. Due to a small active area, many APDs waste collected light and therefore have a much smaller effective $P_i$. This will need to be taken into account when comparing the $S/N_{eff}$.

Under expected values of light flux ( 1 $\mu$W) and detector properties for PMTs and APDs (Table 1) that fit in this setup, it was determined that $S/N_{PMT} >> S/N_{APD}$. In cases of high radiant flux leading to an anode output current of $I_{a,out} > 1\ \mu$A or for time resolution of $< 1$ ns, an APD would be the desirable detector.

## A.4 Calculating velocity from detector signals

This diagnostic was tested during experiments (Fig. A.1) where a laser ($10^{12}$ W/cm$^2$, 1053 nm) ablates a $C_2H_4$ (plastic) target. The resulting LPP streams transverse to the focal axis of the monochromator. The dominant charge state[78], both in terms of kinetic energy density and population fraction, is $C^{4+}$. As LPP particles pass through the collection volume, light of characteristic wavelengths is emitted through self-emission. The light is collected by the lens, filtered through the monochromator and coupled to the PMT.

Based on the geometry of the LAPD, diagnostic ports are only available at specific intervals along the z-axis, which determines the spatial frequency of measurements. Once a given distance has been selected, a time trace of the self-emission of a specified LPP ion species (Fig. A.4a) is recorded. Temporal profiles of ion self-emission are recorded with a time resolution ranging from $10-200$ ns. The self-emission profiles can be transformed into velocity data by using the time-of-flight based on the distance. However, calculating the velocity bins in this way weighs slower particles more than faster particles, as they spend more time in the collection volume. This effect can be corrected by using a velocity-dependent time-integration method, wherein we multiply the amplitude by the velocity. The correction shifts the velocity distributions to larger values, which is shown in the bottom plot of Fig. A.3.

Other diagnostics, such as Langmuir probes, are capable of producing ion velocity traces[45]. The differentiating factor for the diagnostic being presented is the ability to distinguish between ion species based on the emitted spectral line, the control over the S/N and bandwidth of each measurement, and the linearity in response (Langmuir probes have a non-linear response at higher currents due to charge accumulation). In Fig. A.4, three different time profiles and corresponding velocity profiles of $C^{4+}$ at different distances from the target are displayed. These were taken at the same wavelength ($\lambda = 227.1$ nm), but with 3 different shunt resistors (500 Ω for blue, 5 kΩ for orange, and 10 kΩ for green). Although the $S/N$ and bandwidth of these measurements vary significantly, the velocity distributions are mostly unaffected. The furthest measurement of $C^{4+}$

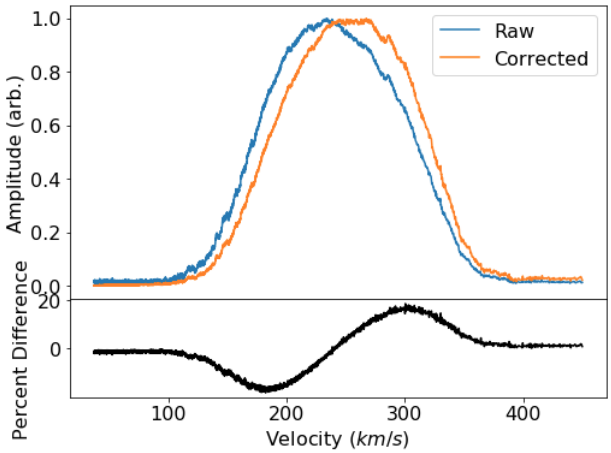


Figure A.3: Top: Comparison of raw (blue) and corrected (orange) $C^{4+}$ ($\lambda$ = 227.1 nm) velocity distributions from self-emission signals. The correction shifts the velocities by up to 20%. Bottom: Relative difference between the two profiles above.

was at 715 cm from the target, limited by the viewing ports of the LAPD.

## A.5 Discussion and conclusion

The system of a monochromator using a photomultiplier tube as a detector was designed to measure time-of-flight (TOF) velocity of laser-produced plasma (LPP) ions streaming transversely to the collection plane, in a magnetized ambient plasma. The diagnostic well resolved the dynamics of the laser plasma ions spatially ($\sim 0.1$ mm$^3$) and temporally ($\sim 10-200$ ns depending on the chosen detector bandwidth) and provided a S/N ratio greater than an avalanche photodiode detector (see Sec. III).

There is no direct way of measuring a localized temperature and density with this diagnostic. However, by comparing the measured spectrum to collisional-radiative modeling software, the temperature and density can be inferred[80]. Temporally and spatially resolved spectra can be collected by varying the monochromator wavelengths across many laser shots. In order to properly compare the measured spectra to a model, the responsivity (or the electrical output per optical input) must be determined. This is important in order to compare the correct absolute amplitudes of the

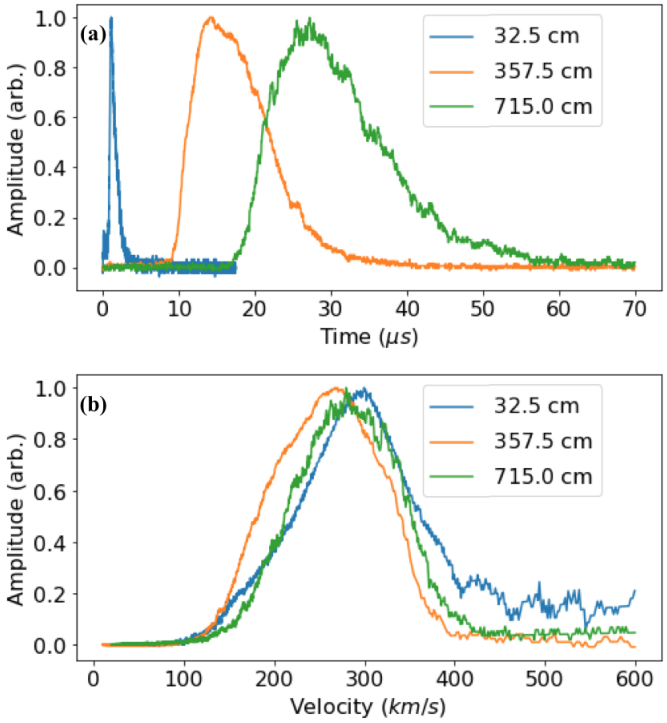


Figure A.4: a) Time traces of $C^{+4}$ ($\lambda$ = 227.1 nm) ion self-emission measured at three distances from the target. b) Corresponding (corrected) velocity traces for each of the time traces.

spectral lines. This calibration can be accomplished using two well-characterized light sources: one being a continuous source to get the wavelength dependence, and the other being a narrow band light source to determine how the instrument function affects the power density[74]. Developing this technique will be a subject for future work.

Bibliography

[1] R Altkorn and R N Zare. Effects of saturation on laser-induced fluorescence measurements of population and polarization. *Annual Review of Physical Chemistry*, 35(1):265–289, 1984.

[2] K. L. Baker, C. A. Thomas, T. R. Dittrich, O. Landen, G. Kyrala, D. T. Casey, C. R. Weber, J. Milovich, D. T. Woods, M. Schneider, S. F. Khan, B. K. Spears, A. Zylstra, C. Kong, J. Crippen, N. Alfonso, C. B. Yeamans, J. D. Moody, A. S. Moore, N. B. Meezan, A. Pak, D. N. Fittinghoff, P. L. Volegov, O. Hurricane, D. Callahan, P. Patel, and P. Amendt. Fill tube dynamics in inertial confinement fusion implosions with high density carbon ablators . *Physics of Plasmas*, 27:112706, 2020.

[3] V.P. Bashurin, A.I. Golubev, and V.A. Terekhin. The collisionless deceleration of an ionized cloud dispersing in a uniform plasma in a magnetic field. *Journal of Applied Mechanics and Technical Physics*, 24(5):614–620, 1983.

[4] Paul M. Bellan. *Fundamentals of Plasma Physics*. Cambridge University Press, 2006.

[5] Yu. A. Berezin, G. I. Dudnikova, M. P. Fedoruk, and V. A. Vshivkov. Explosion phenomena in collisionless plasmas at super-alfvenic speed. *International Journal of Computational Fluid Dynamics*, 10(2):117–126, 1998.

[6] P. A. Bernhardt, R. A. Roussel-Dupre, and M. B. Pongratz. *Journal of Geophysical Research*, 92:57777, 1987.

[7] B C Boland, F E Irons, and R W P McWhirter. A spectroscopic study of the plasma generated by a laser from polyethylene. *Journal of Physics B: Atomic and Molecular Physics*, 1(6):1180–1228–2, November 1968.

[8] P.A. Bonczyk and J.A. Shirley. Measurement of ch and cn concentration in flames by laser-induced saturated fluorescence. *Combustion and Flame*, 34:253–264, 1979.

[9] A. S. Bondarenko, D. B. Schaeffer, E. T. Everson, S. E. Clark, B. R. Lee, C. G. Constantin, S. Vincena, B. Van Compernolle, S. K. P. Tripathi, D. Winske, and C. Niemann. Collisionless momentum transfer in space and astrophysical explosions. *Nature Physics*, 13(6):573–577, 2017.

[10] A. S. Bondarenko, D. B. Schaeffer, E. T. Everson, C. G. Constantin, S. E. Clark, and C. Niemann. Feasibility of characterizing laser-ablated carbon plasmas via planar laser induced fluorescence. *Review of Scientific Instruments*, 83:10E515, 2012.

[11] A. S. Bondarenko, D. B. Schaeffer, E. T. Everson, C. G. Constantin, S. E. Clark, and C. Niemann. Feasibility of characterizing laser-ablated carbon plasmas via planar laser induced fluorescence. *The Review of Scientific Instruments*, 83(10):10E515, October 2012.

[12] Jeffrey Bonde, Stephen Vincena, and Walter Gekelman. Electrostatic structure of a magnetized laser-produced plasma. *Phys. Rev. E*, 92:051102, Nov 2015.

[13] Jeffrey Bonde, Stephen Vincena, and Walter Gekelman. Collisionless coupling of a high- $\beta$ expansion to an ambient, magnetized plasma. ii. experimental fields and measured momentum coupling. *Physics of Plasmas*, 25:042110, 2018.

[14] M. G. H. Boogaarts, S. Mazouffre, G. J. Brinkman, H. W. P. van der Heijden, P. Vankan, J. A. M. van der Mullen, and D. C. Schram. Quantitative two-photon laser-induced fluorescence measurements of atomic hydrogen densities, temperatures, and velocities in an expanding thermal plasma. *Review of Scientific Instruments*, 73:1, 2002.

[15] K. J. Bowers, B. J. Albright, L. Yin, B. Bergen, and T. J. T. Kwan. Ultrahigh performance three-dimensional electromagnetic relativistic kinetic plasma simulationa). *Physics of Plasmas*, 15(5):055703, 03 2008.

[16] Nils Brenning, Tomas Hurtig, and Michael A. Raadu. Conditions for plasmoid penetration across abrupt magnetic barriers. *Physics of Plasmas*, 12(1):012309, 12 2004.

[17] D. Burgess and M. Scholer. *Collisionless Shock in Space Plasmas*. Cambridge University Press, 2018.

[18] Francis F Chen. Langmuir probe diagnostics. In *IEEE-ICOPS Meeting, Jeju, Korea*, 2003.

[19] N. Claire, M. Dindelegan, G. Bachet, and F. Skiff. Nonlinear optical tagging diagnostic for the measurement of fokker–planck diffusion and electric fields. *Review of Scientific Instruments*, 72:4372, 2001.

[20] S. E. Clark, E. T. Everson, D. B. Schaeffer, A. S. Bondarenko, C. G. Constantin, C. Niemann, and D. Winske. Enhanced collisionless shock formation in a magnetized plasma containing a density gradient. *Phys. Rev. E*, 90:041101, Oct 2014.

[21] M. J. Colgan. Fast calculation of collection efficiency for optical emission spectroscopy of extended sources. *Rev. Sci. Instrum.*, 63:5311, 1992.

[22] A. Collette and W. Gekelman. Structure of an exploding laser-produced plasma. *Phys. Rev. Lett.*, 105:195003, Nov 2010.

[23] A Collette and W Gekelman. Structure of an exploding laser-produced plasmaa). *Physics of Plasmas (1994-present)*, 18(5):055705, 2011.

[24] C. M. Cooper, W. Gekelman, P. Pribyl, and Z. Lucky. A new large area lanthanum hexaboride plasma source. *Review of Scientific Instruments*, 81:083503, 2010.

[25] William D. Davis and Alan W. DeSilva. Role of turbulence in the coupling of a magnetic pulse to a collisionless plasma. *The Physics of Fluids*, 16(10):1740–1748, 1973.

[26] G. Dimonte and L. G. Wiley. Dynamics of exploding plasmas in a magnetic field. *Physical Review Letters*, 67:1755, 1991.

[27] D. A. D'Ippolito, J. R. Myra, and S. J. Zweben. Convective transport by intermittent blob-filaments: Comparison of theory and experiment. *Physics of Plasmas*, 18:060501, 2011.

[28] R. Dorst, D. B. Schaeffer, A. Le, J. J. Pilgram C. G. Constantin, S. Vincena, S. K. P. Triapthi, D. Winske, D. Larson, M Coweee, and C. Niemann. High repetition rate mapping of the interaction between a laser plasma and magnetized background plasma via laser induced fluorescence. *Physics of Plasmas*, 29:082113, 2022.

[29] R. S. Dorst, D. B. Schaeffer, J. J. Pilgram, C. G. Constantin, and C. Niemann. *Review of Scientific Instruments*, 2022.

[30] R. P. Drake. *High-Energy-Density Physics*. Springer Berlin, 2006.

[31] RP Drake. The design of laboratory experiments to produce collisionless shocks of cosmic relevance. *Physics of Plasmas (1994-present)*, 7(11):4690–4698, 2000.

[32] P. Dyal. Particle and eld measurements of the starsh diamagnetic cavity. *Journal of Geophysical Research*, 111:23, 2006.

[33] E. T. Everson, P. Pribyl, C. G. Constantin, A. Zylstra, D. Schaeffer, N. L. Kugland, and C. Niemann. Design, construction, and calibration of a three-axis, high-frequency magnetic probe (b-dot probe) as a diagnostic for exploding plasmas. *Review of Scientific Instruments*, 80(11):113505, 2009.

[34] P. B. Farnsworth, B. W. Smith, and N. Omenetto. Computer modeling of collection efficiency of laser excited fluorescence from a graphite furnace. *Spectrochimica Acta.*, 45B(10):1151, 1990.

[35] D. W. Forslund and J. P. Freidberg. Theory of laminar collisionless shocks. *Phys. Rev. Lett.*, 27:1189–1192, Nov 1971.

[36] W. Gekelman, P. Pribyl, Z. Lucky, M. Drandell, D. Leneman, J. Maggs, S. Vincena, B. Van

Compernolle, S. K. P. Tripathi, G. Morales, T. A. Carter, Y. Wang, and T. DeHaas. The upgraded large plasma device, a machine for studying frontier basic plasma physics. *Review of Scientific Instruments*, 87:025105, 2016.

[37] W. Gekelman, M. VanZeelend, S. Vincena, and P. Pribyl. Experiments and observations on intense alfvén waves in the laboratory and in space. *Journal of Geophysical Research*, 108:A71281, 2003.

[38] A. Ghassemi, K. Sato, and K. Kobayashi. Photomultiplier technical handbook third edition (3a). *Hamamatsu Photonics K.K.*, 2016.

[39] S. J. Gitmoer, R. D. Jones, F. Begay, A. W. Ehler, J. F. Kephart, and R. Kristal. Fast ions and hot electrons in the laser–plasma interaction. *The Physics of Fluids*, 29:2679, 1986.

[40] M. J. Goeckner, J. Goree, and T. E. Sheridan. Saturation broadening of laser-induced fluorescence from plasma ions. *Review of Scientific Instruments*, 64(4):996–1000, 04 1993.

[41] A.I. Golubev, A.A. Solov'ev, and V.A. Terekhin. Collisionless dispersion of an ionized cloud into a homogeneous magnetized plasma. *Journal of Applied Mechanics and Technical Physics*, 19(5):602–609, 1978.

[42] J. Grun, R. Decoste, B. H. Ripin, and J.. Gardner. *Applied Physics Letters*, 39:545, 1981.

[43] P. V. Heuer, M. S. Weidl, R. S. Dorst, D. B. Schaeffer, S.K.P Tripathi, S. Vincena, C. Constantin, C. Niemann, L.B. Wilson III, and D. Winske. Laboratory observations of ultra-low-frequency analog waves driven by the right-hand resonant ion beam instability. *The Astrophysical Journal Letters*, 891:1, 2020.

[44] P.V. Heuer, D.B. Schaeffer, E.N. Knall, C.G. Constantin, L.R. Hofer, S. Vincena, S. Tripathi, and C. Niemann. Fast gated imaging of the collisionless interaction of a laser-produced and magnetized ambient plasma. *High Energy Density Physics*, 22:17, 2017.

[45] P.V. Heuer, M.S. Weidl, R.S. Dorst, D.B. Schaeffer, A.S. Bondarenko, S.K.P. Tripathi, B. Van Compernolle, S. Vincena, C.G. Constantin, C. Niemann, and D. Winske. Observations of a field-aligned ion/ion-beam instability in a magnetized laboratory plasma. *Physics of Plasmas*, 25:032104, 2018.

[46] D. W. Hewett, S. H. Brecht, and D. J. Larson. The physics of ion decoupling in magnetized plasma expansions. *Journal of Geophysical Research*, 116:12, 2011.

[47] M. Hoppe and C. Russell. On the nature of ulf waves upstream of planetary bow shocks. *Advacnce in Space Research*, 1:327–332, 1981.

[48] I. H. Hutchinson. *Principles of Plasma Diagnostics*, volume 83. Cambridge University Press, 1987.

[49] T. Ikegami, S. Ishibashi, Y. Yamagata, K. Ebihara, R. K. Thareja, and J. Narayan. Spatial distribution of carbon species in laser ablation of graphite target. *Journal of Vacuum Science & Technology A: Vacuum, Surfaces, and Films*, 19(4):1304, 2001.

[50] M. H. Key and W. T. Toner. *The Physics of Fluids*, 26:2011, 1983.

[51] Yoonyoung Kim, D. Jewitt, J. Luu, J. Li, and M. Mutchler. Comet108p/ciffreo: The blob. *The Astronomical Journal*, 165:150, 2023.

[52] Hamamatsu Photonics K.K. Mppc). *Hamamatsu Photonics K.K.*, 1994.

[53] S. M. Krimigis, G Haerendel, R. W. McEntire, G. Paschmann, and D. A. Bryant. The active magnetospheric particle tracer explorers (AMPTE) program. *Eos, Transactions American Geophysical Union*, 63(45):843–850, November 1982.

[54] Ari Le, Dan Winske, Adam Stanier, William Daughton, Misa Cowee, Blake Wetherton, and Fan Guo. Astrophysical explosions revisited: Collisionless coupling of debris to magnetized plasma. *Journal of Geophysical Research: Space Physics*, 126(9):e2021JA029125, 2021.

[55] M. M. Leroy, D. Winske, C. C. Goodrich, C. S. Wu, and K. Papadopoulos. The structure of perpendicular bow shocks. *Journal of Geophysical Research: Space Physics*, 87(A7):5081–5094, 1982.

[56] J.J. MacFarlane, I.E. Golovkin, and P.R. Woodruff. HELIOS-CR – a 1-D radiation-magnetohydrodynamics code with inline atomic kinetics modeling. *Journal of Quantitative Spectroscopy and Radiative Transfer*, 99(1–3):381–397, May 2006.

[57] R. M. Magee, M. E. Galante, D. McCarren, E. E. Scime, R. L. Boivin, N. H. Brooks, R. J. Groebner, D. N. Hill, , and G. D. Porter. A two photon absorption laser induced fluorescence diagnostic for fusion plasmas. *Review of Scientific Instruments*, 83:10D701, 2012.

[58] John B. McBride, Edward Ott, Jay P. Boris, and Joseph H. Orens. Theory and simulation of turbulent heating by the modified Two-Stream instability. *Physics of Fluids*, 15(12):2367–2383, December 1972.

[59] RWP McWhirter. Plasma diagnostic techniques, ed. *RH Huddlestone and SL Leonard,(Academic, New York, 1965)*, 1965.

[60] B. Meyer and G. Thiell. Experimental scaling laws for ablation parameters in plane target-laser interaction with 1.06 m and 0.35 m laser wavelengths. *The Physics of Fluids*, 27:302, 1984.

[61] A. N. Mostovych, B. H. Ripin, and J. A. Stamper. Laser-produced plasma jets: Collimation and instability in strong transverse magnetic fields. *Physical Review Letters*, 62:2837, 1989.

[62] H. M. Mott-Smith and I. Langmuir. The theory of collectors in gaseous discharges. *Physical Review*, 28:727–763, 1926.

[63] C. Niemann, C. G. Constantin, D. B. Schaeffer, and et. al. High-energy nd:glass laser faciltiy for collisionless laboratory astrophysics. *Journal of Instrumentation*, 7:P03010, 2012.

[64] C. Niemann, W. Gekelman, C. G. Constantin, E. T. Everson, D. B. Schaeffer, A. S. Bondarenko, S. E. Clark, D. Winske, S. Vincena, B. Van Compernolle, and P. Pribyl. Observation of collisionless shocks in a large current-free laboratory plasma. *Geophysical Research Letters*, 41:7413–7418, 2014.

[65] C. Niemann, W. Gekelman, C. G. Constantin, E. T. Everson, D. B. Schaeffer, S. E. Clark, D. Winske, A. B. Zylstra, P. Pribyl, S. K. P. Tripathi, D. Larson, S. H. Glenzer, and A. S. Bondarenko. Dynamics of exploding plasmas in a large magnetized plasma. *Physics of Plasmas (1994-present)*, 20(1):012108, January 2013.

[66] C. Niemann, W. Gekelman, C. G. Constantin, E. T. Everson, D. B. Schaeffer, S. E. Clark, D. Winske, A. B. Zylstra, P. Pribyl, S. K. P. Tripathi, D. Larson, S. H. Glenzer, and A. S. Bondarenko. Dynamics of exploding plasmas in a large magnetized plasma. *Physics of Plasmas*, 20:012108, 2013.

[67] G. O'Sullivan, A. Cummings, C. Z. Dong, P. Dunne, P. Hayden, O. Morris, E. Sokell, F. O'Reilly, M. G. Su, and J. White. Emission and absorption in laser produced plasmas: processes and applications. *JournalofPhysics:ConferenceSeries*, 163:012003, 2009.

[68] K. Papadopoulos. Heating of counterstreaming ion beams in an external magnetic field. *Physics of Fluids*, 14(4):849, 1971.

[69] R. A. Phaneuf, R. K. Janev, and M. S. Pindzola. Atomic data for fusion volume v. *Oak Ridge National Laboratory*, 5:6086, 1987.

[70] C. Plechaty, R. Presura, and A. A. Esaulov. Focusing of an explosive plasma expansion in a transverse magnetic field. *Physical Review Letters*, 111:185002, 2013.

[71] B. H. Ripin, J. D. Huba, E. A. McLean, C. K. Manka, T. Peyser, H. R. Burris, and J. Grun. *Physics of Fluids B*, 5:3491, 1993.

[72] B. H. Ripin, E. A. McLean, C. K. Manka, C. Pawley, J. A. Stamper, T. A. Peyser, A. N. Mostovych, J. Grun, A. B. Hassam, and J. Huba. Large-larmor-radius interchange instability. *Physical Review Letters*, 59:2299, 1987.

[73] B. H. Ripin, R. R. Whitlock, F. C. Young, S. P. Obenschain, E. A. McLean, and R. Decoste. Long-pulse laser-plasma interactions at $10^{12}$-$10^{15}$ w/cm$^2$. *Phys. Rev. Lett.*, 43:350–353, Jul 1979.

[74] M. Sassi and J. W. Daily. Doppler shift methods for plasma diagnostics. *J. Quant. Spectrosc. Radiat. Transfer*, 40(3):426, 1998.

[75] D. B. Schaeffer, W. Fox, R. K. Follett, G. Fiksel, C. K. Li, J. Matteucci, A. Bhattacharjee, and K. Germaschewski. Direct observations of particle dynamics in magnetized collisionless shock precursors in laser-produced plasmas. *Physical Review Letters*, 122:245001, 2019.

[76] D. B. Schaeffer, W. Fox, J. Matteucci, K. V. Lezhnin, A. Bhattacharjee, and K. Germaschewski. Kinetic simulations of piston-driven collisionless shock formation in magnetized laboratory plasmas. *Physics of Plasmas*, 27:042901, 2020.

[77] D. B. Schaeffer, D. Winske, D. J. Larson, M. M. Cowee, C. G. Constantin, A. S. Bondarenko, S. E. Clark, and C. Niemann. On the generation of magnetized collisionless shocks in the large plasma device. *Physics of Plasmas*, 24:041405, 2017.

[78] D.B. Schaeffer, A.S. Bondarenko, E.T. Everson, S.E. Clark, C.G. Constantin, and C. Niemann. Characterization of laser-produced carbon plasmas relevant to laboratory astrophysics. *Journal of Applied Physics*, 120(4), 2016.

[79] G. Schmidt. *Physics of High Temperature Plasmas*, volume 79. Academic Press Inc., 1979.

[80] E. M. Sciamma, R. D. Bengston, W. L. Rowan, A. Keesee, and C. A. Lee et al. Method to estimate the electron temperature and neutral density in a plasma from spectroscopic

measurements using argon atom and ion collisional-radiative models. *Rev. Sci. Instrum*, 79:10E324, 2008.

[81] Rajiv K Singh, OW Holland, and J Narayan. Theoretical model for deposition of superconducting thin films using pulsed laser evaporation technique. *Journal of applied physics*, 68(1):233–247, 1990.

[82] J. J. Song, F. J. Wessel, G. Yur, H. U. Rahman, N. Rostoker, and R. S. White. Fast magnetization of a high-to-low-beta plasma beam. *Physics of Fluids B: Plasma Physics*, 2(10):2482–2486, 10 1990.

[83] D.S. Spicer, R.W. Clark, and S.P. Maran. A model of the pre-sedoc expansion phase of supernova remnant-ambient plasma coupling and x-ray emission from sn 1987a. *The Astrophysical Journal*, 356:549–571, 1990.

[84] D. A. Tidman and N. A. Krall. *Shock waves in collisionless plasma*. Wiley Interscience, 1971.

[85] R. A. Treumann. Fundamentals of collisionless shocks for astrophysical application, 1. nonrelativistic shocks. *The Astronomy and Atrophyical Review*, 17:409–535, 2009.

[86] B. A. Trubnikov. Particle interactions in a fully ionized plasma. *Reviews of Plasma Physics*, 1:105, 1965.

[87] M. VanZeeland and W. Gekelman. Laser-plasma diamagnetism in the presence of an ambient magnetized plasma. *Physics of Plasmas*, 11(1):320–323, January 2004.

[88] M. VanZeeland, W. Gekelman, S. Vincena, and J. Maggs. Currents and shear alfvén wave radiation generated by an exploding laser-produced plasma: Perpendicular incidence. *Physics of Plasmas*, 10:1243–1252, 2003.

[89] M. S. Weidl, D. Winske, and F. Jenko. Hybrid simulations of a parallel collisionless shock in the large plasma device. *Physics of Plasmas*, 23:122102, 2016.

[90] D. Winske and S. P. Gary. Hybrid simulations of debris-ambient ion interactions in astrophysical explosions. *Journal of Geophysical Research*, 112:A10303, 2007.

[91] D. Winske, J. D. Huba, C. Niemann, and A. Le. Recalling and updating research on diamagnetic cavities: Experiments, theory, simulations. *Frontiers in Astronomy and Space Sciences*, 5:51, 2019.

[92] Thomas P. Wright. Early-time model of laser plasma expansion. *Physics of Fluids (1958-1988)*, 14(9):1905–1910, September 1971.

[93] Yu.P. Zakharov. Laboratory simulation of artificial plasma releases in space. *Advances in Space Research*, 29(9):1335–1344, 2002.

[94] John Zinn, Herman Hoerlin, and Albert G. Petschek. The motion of bomb debris following the starfish test. In Billy M. McCormac, editor, *Radiation Trapped in the Earth's Magnetic Field*, pages 671–692, Dordrecht, 1966. Springer Netherlands.